Large Scale Clustering in the Universe

Thesis presented by

Yi-peng Jing

for the degree of Magister Philosophiae

Supervisor: Professor Dennis Sciama

S.I.S.S.A. - I.S.A.S.

Astrophysics Sector

Academic year 1990-91

Acknowledgements

First of all, I deeply thank my collaborators: Drs. S. Borgani, G. Bórner, Y. Gao, H.J. Mo, M. Plionis, R. Valdarnini, Y.Y. Zhou for their fruitful collaboration and insightful discussions based on which the thesis is presented. In particular, I am grateful to M. Plionis for his helpful suggestions which improve the presentation and the readability of the thesis.

My sincere thanks are due to Prof. D. Sciama, my present supervisor, and to Prof. J.L. Zhang, my former supervisor in Hefei, for their invaluable advice and their continuous encouragement in my research work.

My special thanks go to Prof. L.Z. Fang who introduced me to this fascinating field when he was in Hefei.

I would also like to thank Drs. H.G. Bi, S. Bonometto, Y.Q. Chu, H.W. Lee, R. Ruffini for their helpful conversations from which I benefited a lot.

Most of the work presented here was done during my graduate studies at International School for Advanced Studies(SISSA), Trieste and at Center for Astrophysics, University of Science and Technology of China, Hefei. Various supports from both institutes are greatly acknowledged. Part of the work was done during my visit at International Center for Theoretical Physics (ICTP), Trieste; International Center for Relativistic Astrophysics (ICRA), Rome; and Max-Planck Institute of Astrophysics, Garching. I thank these institutions to kindly offer fellowships to me.

Contents

An Overview

One major task of modern cosmology is to understand the Large Scale Structures (LSS) of the Universe. To complete this task, we have to proceed in three steps. The first step is to accumulate the observational data, such as catalogues of galaxies. The second step is analysis the data, usually introducing certain statistical quantities, in order to give a fair description of the structures existing in the Universe. And the final step is to propose and test theoretical models of LSS formation. These three steps are interactive: the observations and the statistical analyses often are motivated and guided by proposed theories; and theories are often proposed or/and improved to explain and understand the observations.

A contribution to understanding the LSS of the Universe is given in this thesis. The first part of the thesis will summarize the recent developments in the theories, the observations, and the statistics, which will be given in the first three chapters. The following chapters contain our original contributions to the subject, which are mostly concentrated on the second step — the statistical measures. More precisely, the thesis is arranged as follows:

In Chapter 1, I will give an outline of the theories of galaxy formation. I will only describe the gravitational instability theory and the conventional Gaussian models dominated by various particles. Our description is rather qualitative, only to supply a frame to understand the statistical results given in the sections containing our original contributions.

In Chapter 2, I will list the main catalogues and samples of extragalactic objects which are often used in the LSS studies. The information relevant to the LSS studies will be outlined. I will emphasize on the size of each sample (such as the number of objects, volume covered), so that we can judge the quality and universality of statistical results based on these samples.

Chapter 3 will describe the commonly used statistical measures of clustering. These are: the correlation function analysis, the void probability function, the minimal-spanning trees, the topological analysis and the percolation method. The results, obtained both by us and by other people, will be summarized, together with constraints that they impose on the theoretical models (if known). So an evaluation of our research work can be made from this chapter.

Afterwards, I will present the details of our research work. In Chapter 4, I present the angular two- and three-point correlation functions of galaxies in the ESO- Uppsala catalog, using angular- diameter (d1)- limited samples. Based on the analysis, the questions regarding the scaling-depth relation, the volume effect on the correlation length, the morphology segregation, etc. are addressed.

Chapter 5 will present our recent work on the superposition effect on the cluster-cluster correlation ξ_{cc}. By a *consistency* check of the redshift correlation function between three redshift samples of Abell clusters and by running numerical simulations, we found there is no evidence that the contamination effect has seriously enhanced the ξ_{cc}, thus the result of ξ_{cc} initially obtained by Bahcall & Soneira (1983) still challenges most of the current models of LSS formation.

In Chapter 6, I present our first statistical analysis on the three-point correlation function ζ_{ccc} of rich clusters. We found that ζ_{ccc} can be approximated by the hierarchical form, just like galaxies. The results put strong constraints on the linear 'biasing' theories.

It seems the 'biasing' theory can't explain the observed ζ_{ccc} [but see Gott *et al.* (1991, preprint) including nonlinear clustering effect]. In Chapter 7, we explore the problem in an interesting alternative — the bubble model. We found that the hierarchical form emerges in this scenario, with weak dependence on the model details.

It appears impossible to extract the higher-order($N \geq 4$) correlation functions of rich clusters by the correlation analysis. In the last chapter, we study the problem using the void probability function $P_0(V)$, which is known to be connected with all N-point correlation functions(White 1979). The results show that Abell clusters are distributed with scale invariance and the scaling is independent of cluster richness. Furthermore, by comparing with the CFA sample, we tentatively conclude that there exists a universal scaling in the distributions of galaxies and clusters.

1

An outline of the theories of galaxy formation

In this chapter, I shall give an outline of current galaxy formation theories. To prove or disprove these theories is one of the major tasks of the LSS studies. The statistics of galaxy clustering are often guided and motivated by these theories. An accurate description of the models usually needs to solve a set of differential equations in the linear regime and to run N-body simulations in the nonlinear regime, to follow the evolution of density perturbations. It is out of the scope of this thesis to give much detail. Instead here I give a qualitative description of the main features of the models which are mostly relevant to the statistics used in the thesis. I hope the material presented here is helpful to understand the following chapters. Rigorous treatment of the models can be found in several excellent text books.

In §1.1, I will summarize the parameters upon which current models of galaxy formation depend, and classify the models according to these parameters. Then a qualitative description of the gravitational instability theory follows in §1.2. The biasing mechanisms are illustrated, in §1.4, by choosing 'peaks' in the Gaussian fields. The transfer functions and the main features of the conventional models will be given in §1.3 and 1.5 respectively. Here we shall not discuss the cosmic string scenario and explosion theory, though they are also plausible.

1.1 The model parameters

The current theories of galaxy formation generally are based on the hot big-bang cosmology. Therefore the parameters of the big-bang model are also the parameters of the galaxy formation theories. These are:

a). The density parameter Ω_o: $0.1 \leq \Omega_o \leq 1$;

b). The Hubble constant H_o: $H_o = 100h\text{km sec}^{-1}\ \text{Mpc}^{-1}$ and $0.4 \leq h \leq 1$;

c). The temperature of the cosmic background radiation T_o: $T_o \approx 2.7\text{K}$;

d). The cosmological constant Λ, which is usually set to be zero.

Besides them, there are further parameters which belong to the galaxy formation theories mostly(if not entirely). They are:

e). The contents of the Universe: Is there dark matter? If it does exist, is it baryonic matter, Cold Dark Matter (CDM), Hot Dark Matter(HDM), unstable dark matter? And how much of it is there? (Ω_i?)

f). The primordial fluctuations: How did these fluctuations originate? Are they Gaussian or non-Gaussian? What spectrum $P(k)$ do they have? If $P(k)$ is a power law, how large is the amplitude and what is the slope?

g). Biasing: does light trace mass in the spatial distribution? If not, how is it biased? Which physical process leads to the biasing?

h). The effect of non-gravitational process: Is the effect, like explosion, important in forming the LSS?

According to the distinctive features of the resulting structures, I group the models into the following categories:

i). Gaussian fluctuation models dominated by
- ♣ Baryonic matter
- ♣ Cold dark matter (CDM)
- ♣ Hot dark matter (HDM)

ii). Non-Gaussian fluctuation model
- ♣ Cosmic strings

iii). Explosions

In each set of the models, the 'biasing' mechanism can be further introduced. In this chapter, I will concentrate on the first set of models.

1.2 The basics of the gravitational instability theory

It's generally thought that the structures we see today, such as galaxies, clusters and superclusters, originate from the small density inhomogeneities in the early Universe. The amplification mechanism of the perturbations is thought to be the gravitational instability. In this section, I shall give the fundamentals of this mechanism.

1.2.1 Three different eras

According to the different behaviours of perturbation growth, we divide the entire history of the Universe into three eras. This division will help us to describe the evolution of density inhomogeneities(see §1.3).

a. The first era is the radiation dominated phase at $1+z \geq 1+z_{eq} = 2.5 \times 10^4 (\Omega_o h^2)$. During this phase, radiation density exceeds that of the non-relativistic matter. The comoving horizon size at $1+z_{eq}$ is: $\lambda_{eq} = 13(\Omega_o h^2)^{-1}$Mpc;

b. The second era is between $1+z_{eq}$ and $1+z_{dec} \sim 1100$. During this stage, non-relativistic matter begins to dominate the radiation. The radiation is strongly coupled with the baryons at the initial stage of the era, and begins to decouple from the baryons at the final stage, therefore the baryon-radiation can be approximated as an idea fluid in this era;

c. The last era is after $1+z_{dec}$, when ions and free electrons recombine. Eventually the free electron density becomes so low that radiation and matter become decoupled. Because of the decoupling, the pressure in matter drops immensely. If there is no reionization, photons behave like collisionless particles of $m = 0$ afterwards.

1.2.2 Three important length scales

There are three length scales which are relevant to the size of the resulting structures. These are:

a. The Jeans length of a fluid: As we know, the time scale of gravitational growth is: $t_g \sim (G\rho)^{-1/2}$; and the time scale of diffusion on scale l due to pressure is: $t_d = l/v_s$

(where v_s is the sound speed). If $t_g < t_d$, the fluctuation on scale l can gravitationally grow; otherwise the fluctuation behaves like a sound wave. For the critical case, $t_g \sim t_d$, we have a length $\lambda_J = v_s(G\rho)^{-1/2}$ which we call the Jeans length. Clearly, only fluctuations larger than λ_J can grow under gravitational instability.

b. Perturbations in collisionless components suffer the Landau damping. Until the perturbation becomes Jeans unstable and begins to grow at t_{eq}, the collisionless particles can stream out from the overdense regions into the underdense regions, thus erasing the inhomogeneities. The length scale of the damping is obtained by solving the collisionless Boltzmann Equation. Its approximate value can be estimated by calculating the path traveled by a particle from the beginning to t_{eq}. The comoving length traveled by a particle is

$$\lambda_{FS} \equiv r(t_{eq}) - r(t_i) = \int_{t_i}^{t_{eq}} \frac{v(t)}{R(t)} dt$$

Assuming the particle becomes non-relativistic at t_{NR}, then

$$\lambda_{FS} = \int_0^{t_{NR}} \frac{1}{R(t)} dt + \int_{t_{NR}}^{t_{eq}} \frac{R_{NR}}{R^2(t)} dt$$

In the radiation dominated era, $R(t) \propto t^{1/2}$, so

$$\lambda_{FS} = (\frac{t_{NR}}{R_{NR}})[2 + \ln(\frac{t_{eq}}{t_{NR}})]$$

For the light neutrinos, $\lambda_{FS} = 20(30\text{ev}/m_\nu)\text{Mpc}$.

c. The perturbations in the baryon-photon fluid are subjected to the Silk damping around the recombination era, because the perfect fluid approximation breaks down. A rigorous treatment of the problem needs to solve the collisional Boltzmann Equation. The length scale of the damping is approximately the diffusion length of a photon. It can be estimated as follows. The photon mean free path : $\lambda_\gamma = (\chi_e n_e \sigma_T)^{-1}$ (where χ_e is the ionization rate; n_e is the density of electrons; and σ_T is the Thomson cross-section). In a time interval Δt, a photon suffers $\Delta t/\lambda_\gamma$ collisions and makes a random walk whose size squared is

$$\Delta r^2 = \frac{\Delta t}{\lambda_\gamma(t)} \frac{\lambda_\gamma^2(t)}{R^2(t)} = \frac{\Delta t \lambda_\gamma(t)}{R^2(t)}$$

So the Silk damping scale is

$$\lambda_S = \sqrt{\int_0^{t_{dec}} dt \frac{\lambda_\gamma(t)}{R^2(t)}}$$

If we take suitable values for each parameter, we get λ_S:

$$\lambda_S \approx 3.5(\Omega_0/\Omega_b)^{1/2}(\Omega_0 h^2)^{-3/4} \text{ Mpc}$$

Note that the isocurvature perturbations do not suffer from this effect, since the spatial distribution of photons is homogeneous.

1.2.3 Linear perturbation theories

If the fluctuations are well within the horizon and the characteristic velocity $\ll$ the light speed c, the Newtonian approximation suffices. If δ is the density contrast on the scales much larger than the Jeans length for the fluid, the linear perturbation equation is:

$$\frac{d^2\delta}{dt^2} + 2\frac{\dot{R}}{R}\frac{d\delta}{dt} = 4\pi\rho_b G\delta$$

For a flat model with matter dominated, we have

$$\delta_1 = D_1(t)\delta_i \qquad D_1(t) \propto R(t) \propto t^{2/3} \qquad \text{growing mode;}$$

and

$$\delta_2 = D_2(t)\delta_i \qquad D_2(t) \propto R(t)^{-3/2} \propto t^{-1} \qquad \text{decaying mode.}$$

Since the second mode decays very rapidly, we are mostly interested in the growing mode. The explicit expressions of $D(t)$ can be obtained separately for the closed and open Universes, but here we only give some qualitative, approximate properties of such solutions.

In an open model of $\Omega_o < 1$, $\delta_1 = D_1(t)\delta_i$. When $z > \Omega^{-1}$, $D_1(t) \propto t^{2/3}$; however for $z < \Omega^{-1}$, the growth is suppressed.

In a closed model of $\Omega_o > 1$, $\delta_1 = D_1(t)\delta_i$. Its growth is more rapid than in the flat model.

Since the physical length $l_{ph} \propto R(t)l_{co}$, and the horizon length is $\sim t$(which is proportional to R^2 in the radiation-dominated era and to $R^{3/2}$ in the matter dominated era), the fluctuations which give rise to galaxies or other structures, must be larger than the size of the horizon (*i.e.*, $l_{ph} > t$) at sufficiently early times. In order to treat such super-horizon-sized fluctuations, one needs a full general-relativistic analysis. In this case, the universe can always be regarded as a flat one. In the synchronous metric, there are two physical modes: a decaying mode and a growing mode; and two pure gauge modes. The growing mode evolves as $\delta \propto R^2$ in the radiation dominated era and $\delta \propto R$ in the matter dominated era.

1.3 The transfer functions and the processed power spectrum in the baryon, CDM and HDM models

Let the density fluctuation spectrum be $P_i(k)$ at the initial time. As the perturbation evolves, we would observe at the present, the processed density spectrum $P(k) = T^2(k,t_0)D_1^2(t_0)P_i(k)$. The function $T(k,t_0)$ is called the transfer function. Its importance to the LSS studies is obvious and it can be strictly solved in the linear regime. Here I qualitatively discuss $T(k,t_0)$ in the baryon, CDM and HDM models.

At the first stage $t < t_{eq}$, the fluctuations of size greater than the horizon grow as D_1(*i.e.*, $T(k) = 1$). The sub-horizon fluctuations in WIMP (Weak Interacting Massive

Particles) components can not grow (or at best they logarithmically grow with R) due to the radiation domination (also called the Meszaros effect). This effect leads $T(k) \propto R_h^2(k)$, *i.e.*, $T(k) \propto k^{-2}[R_h(k)$ is the scale factor when fluctuations of k enter the horizon]. Furthermore, the perturbations of size less than λ_{FS} are erased in this stage due to the Landau damping. This effect can be modeled as $T(k) = 0$. Baryon-Radiation (B-R) fluctuations within the horizon behave like sound waves due to the large Jeans length. This effect can be written as $T(k) = f(\text{oscillating})$.

During the next stage ($t_{eq} < t < t_{dec}$), fluctuations in WIMP grow $\propto D_1(t)$. B-R perturbations inside horizon behaves like a sound wave, but the super-horizon perturbations grow also $\propto D_1(t)$. How to model these effects is obvious (see above).

At and after the recombination ($t \geq t_{dec}$), fluctuations in WIMP grow $\propto D_1(t)$[until $z = \Omega_0^{-1} - 1$ if the universe is open]. At recombination, baryon and radiation are decoupled, and the Jeans mass in baryon is reduced to the (sub-)galactic scale. At the meantime, Silk damping erases all perturbation in baryon of $\lambda < \lambda_S$. Afterwards in the baryon dominated universe, the fluctuations grow $\propto D_1(t)$; in the WIMP dominated universes, baryons will soon catch up the fluctuation of WIMP after the recombination(taking several expansion factors). The Silk damping is modelled as $T(k) = 0$ for $k < k_S$, and other processes are apparent.

Finally we can write the $T(k, t_0)$ approximately as:

$$T_{baryon}(k, t_0) = \begin{cases} 0, & \text{if } k > k_S; \\ \propto k^{-2}\ f(\text{oscillating}), & \text{if } k_S > k > k_{dec}; \\ 1, & \text{if } k < k_{dec}, \end{cases}$$

for the baryon universe;

$$T_{CDM}(k, t_0) = \begin{cases} \propto k^{-2} & \text{if } k > k_{eq}; \\ 1, & \text{if } k < k_{eq}, \end{cases}$$

for the CDM universe; and

$$T_{HDM}(k, t_0) = \begin{cases} 0, & \text{if } k > k_{FS} \sim k_{eq}; \\ 1, & \text{if } k < k_{FS} \sim k_{eq}, \end{cases}$$

for the neutrinos dominated universe. With these transfer functions, we can easily get the processed spectrum. Figure 1.1 shows the processed spectrums $P(k) = \mid \delta^2(k) \mid$ in baryon(open), CDM and HDM universes with the initial Zel'dovich spectrum $P_i(k) \propto k$, taken from the rigorous calculation of Holtzman(1989). The various effects emphasized above are obvious in the figure. We can also see the qualitative features of $T(k)$ given above.

1.4 A simple 'biasing' scheme — An example

1.4.1 Why we need 'biasing'

Up to now, we have only discussed the matter distribution. It is unclear to us whether galaxies (or clusters) trace mass distribution in space. It is not a trivial problem. The

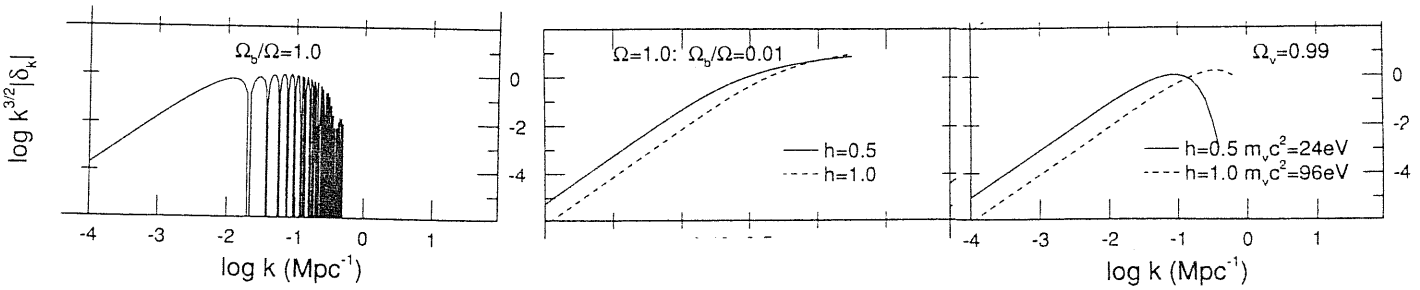

Fig.1.1 — The processed spectrums for baryon($\Omega_b = 0.2$), CDM(flat) and neutrinos(flat) dominated universe with scale-invariant adiabatic initial conditions(from left to right). Note $k^{3/2} \mid \delta_k \mid$ in the vertical coordinate corresponds to $k^{3/2}P^{1/2}(k)$ in the text.

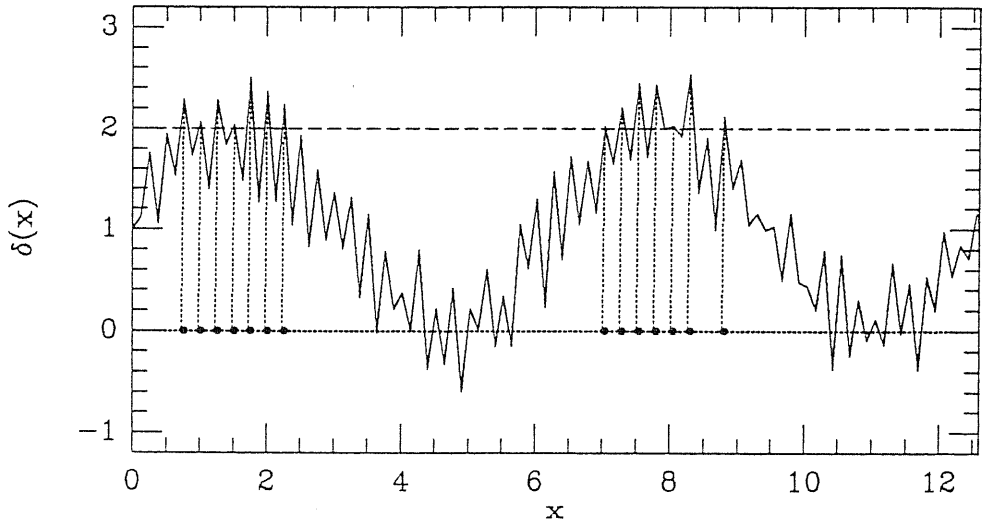

Fig.1.2 — A sketch map of the biasing scheme. Taken from Borgani (1990).

strong clustering exhibited by rich clusters at least shows that clusters and galaxies are not equivalent tracers in spatial distribution. This is one motivation for the proposal of the biased galaxy formation (Kaiser 1984).

The dynamical studies of galaxy distributions, such as the 'infall' argument, the Virial theorem, etc., always give an Ω about 0.2, while the inflation theories request $\Omega = 1$. In these studies, $\Omega \propto \delta_m^2$, and assume $\delta_m = \delta_g$ (*i.e.* galaxies trace mass). However, if galaxies are a biased tracer, e.g., $\delta_g = 2 \sim 3\delta_m$, we can have $\Omega = 1$ in such studies, *i.e.*, a flat universe.

The huge voids, such as Böotes, are rather difficult to be produced in the Gaussian models, if light traces mass. However, if galaxies do not trace mass, the void regions could be less empty in mass distribution than in galaxy distribution, and the problem could be solved.

N-body simulations of both hot and cold dark matter models need anti-biasing and biasing respectively, otherwise they can't produce the right amplitude and right slope of the galaxy-galaxy correlation function ξ_{gg}.

There are other theoretical arguments, though not as strong or clear as those listed above, that galaxies could be a biased tracer of the mass (see Dekel & Rees 1987)

1.4.2 One simple biasing scheme as an example

If fluctuations are Gaussian, the rare high peaks are more clustered than the background. This can be understood from Figure 1.2. In the figure, the small-wavelength perturbation is modulated on the long-wavelength one. If we choose only rare peaks with $\delta > \nu\sigma = 2$, such peaks must be more clustered than the background, as clearly shown in the Figure. As Kaiser(1984, later many others) show, the two-point correlation function of $\delta \geq \nu\sigma$ peaks is

$$\xi_{peaks} = \exp(\nu^2 \xi_{\rm background}) - 1.$$

For $\xi_{\rm background} \ll 1$, we have

$$\xi_{peaks} = \nu^2 \xi_{\rm background}$$

If $\nu \geq 1$, the peaks are more clustered than the background.

1.5 Main features of the conventional models

1.5.1 The baryon dominated Universe

The most attractive feature of this model is "what we see is what we get": we do not need any exotic particles. The model is always open, since the big-bang nucleosysthesis theory puts the upper limit on the baryonic density $\Omega_b < 0.2$. The galaxies and mass are the equal tracers in the spatial structures.

If the initial fluctuation is adiabatic, the fluctuations in baryonic matter are erased during the decoupling on scales smaller than the Silk damping(see §1.2 & 1.3). The first forming objects are of mass $10^{13} \sim 10^{14} M_\odot$, *i.e.*, the mass scale of rich clusters and superclusters. So the model is of the nature of the 'top-down' scenario.

In the adiabatic model, the gravitational growth becomes effective only from the decoupling $z = 1100$ to $z \approx \Omega_b^{-1} \sim 5$, giving growing factor $A \sim 200$(see §1.2). In order to produce structures observed, we have to require a large fluctuation amplitude at decoupling which would lead to $\Delta T/T \sim 10^{-3}$ at arcminutes scale, in severe conflict with the available experiments(Uson & Wilkinson 1984; Readhead *et al.* 1989). Because of this difficulty, the model has lost its initial popularity.

If the initial fluctuation is isothermal, there is no Silk damping effect, so the structures form as in the 'top-down' picture. The attractive feature is that it can produce coherent clustering on large scale, such as large scale bulk motion of Dressler *et al.* (1987). The anisotropy $\Delta T/T$ is much smaller than in the adiabatic case, however the observations of Readhead *et al.*(1989) have already ruled out this model if there are no reionizations after the decoupling (Efstathiou 1988). But if the universe is reionized, the model can be consistent with all the observations of $\Delta T/T$, although the constraint is quite stringent(Efstathiou 1988).

The studies of the isocurvature model, up to date, have been limited within the linear perturbation theories. The model is consistent with the observations of $\Delta T/T$, the large scale peculiar velocity fields and flux dipoles. So the model can not be ruled out. However, there are no simulation studies in the non-linear regime. Therefore many properties regarding the clustering statistics, given below, are not clear yet.

1.5.2 The HDM model

The HDM model is attractive because the neutrinos, as the missing mass, are the only particle known to us. Especially, since it is declared that the mass of neutrinos has been detected to be about several tens Ev, which is just as large as to close the Universe.

The distinctive feature of the HDM model is the large streaming length $\sim$ tens Mpc, so the first forming objects are of the size of superclusters. Galaxies and clusters of galaxies are the results of fragmentation of the first forming objects ('top-down' scenario). So this model can easily produce filamentary structures.

The most severe problem of the scenario is that galaxies have formed very recently $z \sim 1$, in contrast with the observations of quasars at $z > 4$. The problem is inevitable, since galaxies form when superclusters collapse and the observations show that superclusters are reaching or reached very recently the nonlinearity.

The model has been studied in much detail, both by linear perturbation theories and by N-body simulations. As a result, the model has been convincingly ruled out by the recent observation of $\Delta T/T$ at a one degree scale(Bond *et al.* 1991). If there is no biasing, the detailed N-simulations show that the model is unable to produce the right amplitude A_{gg} of ξ_{gg}, the hierarchical form of the three-point correlation function of galaxies, the cluster-cluster correlation function, the scaling behaviour of voids, etc.(*e.g.*, Batuski, *et al.* 1987; Fry, *et al.* 1989). Introducing biasing or anti-biasing may resolve part of the problems, but at the expense of making other problems more severe. The theory seems out of repair.

1.5.3 The standard CDM model

The standard CDM model has dominated galaxy formation theories for many years. This is the most successful model, though it is facing challenges from recent observations. The most attractive feature of the model is that it is just the one the inflation theories predicted. There are only three parameters: h, the amplitude of $P(k)$ and the biasing prescription, to be adjusted. But there are several sets of observations against which the model can be tested.

One distinctive feature of the model is that smaller objects form earlier than larger ones, *i.e.*, the 'bottom-up' scenario (see §1.3).

Another feature is 'biasing'. In the 'standard' CDM model, the galaxies must be a biased tracer of the mass distribution, as discussed in §1.4. White *et al.*(1987) proposed that galaxies preferentially form at halos with large circular velocities v_c, as a 'natural' biasing scheme. Their simulations show that the objects of large v_c are clustered more than those of smaller v_c. Because of the Faber-Jackson and the Tully-Fisher relations, the model predicts that faint galaxies are distributed more randomly than bright ones. The prescription, however, may be still too simple. But as hinted by their studies, galaxies of different types(*e.g.* luminosity, morphology, rotation velocity) are likely to have different clustering properties.

The model has been studied in great detail. It successfully passed the $\Delta T/T$ test on various angular scales. The model can reproduce all the features observed on scales from tens Kpc to 10 Mpc: *e.g.*, the correlation functions of galaxies, the Faber-Jackson and the Tully-Fisher relations, the scaling behaviours of voids, the relative pair-velocities, ... etc.. However, because of the lack of clustering power on large scales, the model is unable to

explain the features observed recently on several tens Mpc: the cluster-cluster correlation function, the angular two-point correlation function from the APM survey, the variance of the IRAS survey, the large peculiar velocity fields, etc. It is evident that the standard model has to be revised. The revisions might be able to improve the comparisons of the model with the observations, but some attractive properties of the 'standard' model would be lost.

2

Major observational samples

Our understanding of the matter distribution in the Universe mainly comes from the distributions of galaxies, of galaxy groups and of galaxy clusters, since telescopes can only directly detect these objects. Although presently we are still uncertain which (if any) of these objects fairly trace the matter distribution in the universe(see §1.4), it is of no doubt that these distributions are closely related. Moreover, the ultimate goal of the galaxy formation theories is to understand the distribution of these objects. Thus it is very important to study their spatial distributions.

As in any branch of astronomy, meaningful statistics regarding their distribution need samples (or catalogues) whose selection procedures are well defined and as free as possible of systematic biases and effects. Here I list the major observational samples and catalogues in the LSS studies, together with their defining criteria. There certainly exist, in some (perhaps all) of these samples, systematic biases which must be corrected in the LSS studies, otherwise spurious clustering could result. However the procedures for correcting such effects are usually very complicated, and their description is beyond the scope of this thesis but could be found in the literature.

♣ The Lick catalogue

This catalogue contains $\sim$ one million galaxies with $m_b \leq 18.9$ in the sky $\delta > -22.5°$ (Shane & Wirtanen 1967; Seldner *et al.* 1977). Galaxies are counted in each 10×10 arcmin^2 cells. The characteristic sample depth is about 210 h^{-1}Mpc. The reduction and correction procedures of the catalogue can be found in Seldner *et al.* (1977) and Plionis (1988).

♣ The Zwicky Catalogue

The Zwicky catalog contains 28,000 galaxies in the northern sky $\delta > -3°$. Galaxies are listed down to $m_{pg} = 15.7$, and the catalog is reasonably complete to $m_{pg} = 15.5$. This catalog is the important database for the LSS study in the northern sky (Zwicky *et al.* 1961-68).

♣ The Uppsala Catalogue

This catalogue lists angular positions of $\sim$ 13,000 galaxies in the sky area $\delta > -2.5°$. The sample is complete to major (apparent) axis $D_1 \simeq 1'$. Morphological types, diameters, and magnitudes(if observed) are also given. The characteristic sample depth is about 70 h^{-1}Mpc (Nilson 1973).

♣ The ESO/Uppsala catalogue

This catalogue lists angular positions of $\sim$ 15,000 galaxies in the southern sky with $\delta < -17.5°$. It's also claimed to be complete to major (apparent) axis $D_1 \simeq 1'$. Morphological types and diameters are presented for all galaxies. The sample depth is slightly deeper than that of the Uppsala catalogue (Lauberts 1982).

♣ The APM galaxy survey

This is a uniform sample of $\sim$ 2 million galaxies to a magnitude limit of $b_J = 20.5$, covering the 4300 square degrees area of $b \leq -40°$ and $\delta < -20°$. The survey is based on 185 UKSTU J survey plates which are scanned and digitized by the APM facility in Cambridge (Maddox *et al.* 1990b).

♣ The IRAS galaxy samples

A new type of galaxy samples, IRAS galaxy samples, come from IRAS database (*IRAS Point Source Catalog*, Version 2 1988; e.g., Saunders *et al.* 1990; Strauss *et al.* 1990). These samples are usually flux limited (mostly at 60μm), and are selected on the flux quality at 60μm and far-infrared colours, in order to discriminate against cirrus, stars and planetary nebulae. The advantages of the large coverage ($\sim$ 80%) of sky, lack of the Galactic extinction in the far-infrared, well-calibrated flux densities, and $\sim 120h^{-1}$Mpc characteristic sample depth, make such samples very useful in the LSS studies. If the limiting flux is 0.5 Jy at 60μm, there are roughly 17,000 galaxies.

♣ CfA Redshift Survey

The sample presents the radial velocities for the *all* 2401 galaxies in the merged Zwicky-Nilson catalogue brighter than 14.5 m_Z with $b^{II} \geq 40°$ and $\delta \geq 0°$, or $b^{II} \leq -30°$ and $\delta \geq 0°$. Its typical sample depth is $\sim$40 h^{-1}Mpc(Huchra *et al.* 1983).

♣ Southern Sky Redshift Survey

This is a diameter-limited redshift survey in the southern sky with comparable depth and sky area to the CfA survey. The galaxies are selected from the ESO/Uppsala catalogue. The survey contains all 1957 galaxies with face-on diameter greater than 1.23′, on the sky with $\delta < -17.5°$ and $b^{II} < -30°$. A total of 1735 galaxies have available redshifts. Redshift incompleteness is a strong function of morphology types; dwarfs are especially incomplete (da Costa *et al.* 1991).

♣ CfA2 Redshift Survey of Galaxies

This survey, intended to extend the original CfA redshift survey (1983) to the magnitude limit $m_{pg} = 15.5$ over a similar sky area, is still emerging. Four strips of 6° in declination are reported to be complete in redshift. Only the data of the first slice of $8^h \leq \alpha \leq 17°$ and $26.5° \leq \delta \leq 32.5°$, which consists of 1057 galaxies, have been published (Huchra et al. 1990b).

♣ Northern Redshift Survey of Dwarf and LSB galaxies

As shown by Thuan and Seitzer (1979), the UGC was fairly complete for all dwarf and low surface brightness (LSB) galaxies larger than 1′(the UGC diameter lower limit), so the UGC could become a good database for selecting a sample of Dwarf and LSB galaxies. The sample of Thuan *et al.* (1991) contains *all* galaxies classified in the UGC with a Hubble type of Dwarf, Dwarf Irregular, Dwarf Spiral, Ir, Sc-Irr, or S-Irr; a de Vaucouleurs type of Sd-dm, Sdm, Sm, or Im; or in the absence of these classifications, a van den Bergh luminosity class of IV-V or V. These selection criteria result in a sample of 1845 galaxies. This sample were observed by Arecibo and Green Bank telescopes at 21 cm. The detection rate of 84%, gives a total sample of 1557 galaxies with 21 cm redshifts.

♣ A Redshift Survey of IRAS Galaxies with $f_{60} > 1.936$ Jy

This is a redshift complete sample of IRAS galaxies with the flux limit $f_{60\mu m} > 1.936$ Jy. It contains 2649 galaxies, covers 87.6% of the sky, and has sample depth $\sim 50h^{-1}$Mpc (Strauss *et al.* 1990).

♣ The QDOT Redshift Survey of IRAS Galaxies

This is a sparse-sampled redshift survey of IRAS galaxies, at sampling rate of one in six, complete to the flux limit $f_{60} = 0.6$Jy at $\mid b \mid \geq 10°$. It consists of 2163 galaxies, of which 2093 have available redshifts. It is about 2 times deeper than the sample of Strauss *et al.* (1990), at the expense of sparse-sampling.

♣ ACO Catalogue of Clusters of Galaxies

This is an all-sky catalogue of rich clusters of galaxies, complete nominally to $z = 0.2$ for clusters with populations (N_A) of 30 or more galaxies within Abell radius $r_A = 1.5h^{-1}$Mpc and in the magnitude range m_3 to $m_3 + 2.0$, where m_3 is the magnitude of the third brightest cluster member. There are a total of 4073 clusters. Their positions in the sky are listed, together with the distance class D, the richness class R, m_{10} (the magnitude of the tenth brightest cluster member), Bautz-Morgan types, redshifts if available, *etc.* (Abell *et al.* 1989).

♣ Shectman Catalogue of Clusters of Galaxies

The Shectman catalogue, consisting of 646 clusters, has been constructed from the Shane-Wirtanen counts in $10'$ bins by identifying local density maxima above a threshold value(about 3.6 times of the mean density) relative to eight surrounding cells, after slightly smoothing the data to reduce the effect of the sampling grid. It covers the sky region of $\delta \geq -22.5°$ and $\mid b \mid \geq 40°$. About 70% of $D \leq 4$ and 10% of $D \leq 5$ Abell clusters have been identified in the catalogue. It also includes much poorer clusters, which consist of 60% the sample. The characteristic sample depth is similar to the $D \leq 4$ sample of Abell clusters (Shectman 1985).

♣ Plionis *et al.* Catalogue of Clusters of Galaxies

This catalogue, also based on the Shane-Wirtanen counts in $10'$ bins, has been compiled by identifying overdensity regions above certain threshold values: $\sigma / < \sigma >$=3.6, 3.0, 2.5, 1.8. It contains $\sim$ 6000 clusters, covering the sky of $\delta \geq -22.5°$ and $\mid b \mid \geq 40°$. At the highest overdensity threshold all clusters found are either Abell or Zwicky clusters (Plionis *et al.* 1991).

♣ Redshift samples of Abell clusters

Two subsamples, extracted from the original Abell catalogue (1958), now have complete redshift information. One is the sample of 103 clusters of richness $R \geq 1$ and distance $D \leq 4$ at the high galactic latitude $\mid b \mid \geq 30°$ (Hoessel *et al.* 1981). The other, completed recently, covers a 561 square degree in the region of $10^h \leq \alpha \leq 15°$ and $58° \leq \delta \leq 78°$, and includes 145 clusters with $R \geq 0$ and $D \leq 6$(Huchra *et al.* 1990a).

The nearby sample of $D \leq 4$ and $R \geq 0$ at $\mid b \mid \geq 30°$, is also near to redshift completion ($\sim$ 95%). An update compilation by Struble and Rood (1991a) lists $\sim$ 650 redshifts for Abell clusters and will soon appear in *ApJS*.

♣ CfA Catalogue of Groups of Galaxies

Catalogues of groups of galaxies are usually produced by friends-friends finding algorithm(Huchra & Geller 1982). The CfA catalogue, based on the 14.5 m_B CfA redshift survey, identifys groups as density enhancements in redshift space of a factor greater than 20. It consists of 176 groups with more than two members. It covers the same sky area and has a similar sample depth as the 14.5 m_B CfA redshift survey (Geller & Huchra 1983).

♣ SSRS Catalogue of Groups of Galaxies

This catalogue, based on the SSRS redshift survey, is produced by the same techniques used in the CfA catalogue. It contains 87 groups with more than two members (Maia *et al.* 1989).

♣ CfA2 Catalogue of Groups of Galaxies

The groups of the catalogue are identified, in the two CfA redshift slices of $8^h \leq \alpha \leq 17^h$ and $26.5° \leq \delta \leq 38.5°$, as density enhancements in redshift space of a factor greater than 80. It contains 128 groups with three or more members (Ramella *et al.* 1989).

3

Statistical measures of clustering

Even from two-dimensional maps (or catalogs) of galaxies and clusters, we can easily find that their spatial distribution is quite clumpy. An example, in Figure 3.1, shows the positions of all the galaxies from the Zwicky *et al.* catalog which satisfy $m_B \leq 15.5$, $8^h \leq \alpha \leq 17^h$ and $8.5° \leq \delta \leq 50.5°$. The grid is Cartesian in R.A. and decl., and the deficiency of galaxies west of 9^h and east of 16^h is caused by Galactic obscuration. The Coma cluster and the Virgo cluster are the dense regions at ($\alpha = 13^h$, $\delta \simeq +29°$) and at ($\alpha = 12.5^h$, $\delta \simeq +12°$). Several other well known clusters, e.g., Abell 1367 (11.7^h, $+21°$), Abell 2197/2199 complex(16.3^h, $+38°$), are also obvious. These dense regions appear to be connected by "galaxy chains/surfaces". Between these structures, prominent "voids" (*i.e.*, the regions which are devoid of galaxies) can be seen, which stand up, for examples, at ($\alpha \simeq 15.5^h$, $\delta \simeq +35°$), ($\alpha \simeq 12.8^h$, $\delta \simeq +21°$), ($\alpha \simeq 10^h$, $\delta \simeq +26°$), etc.

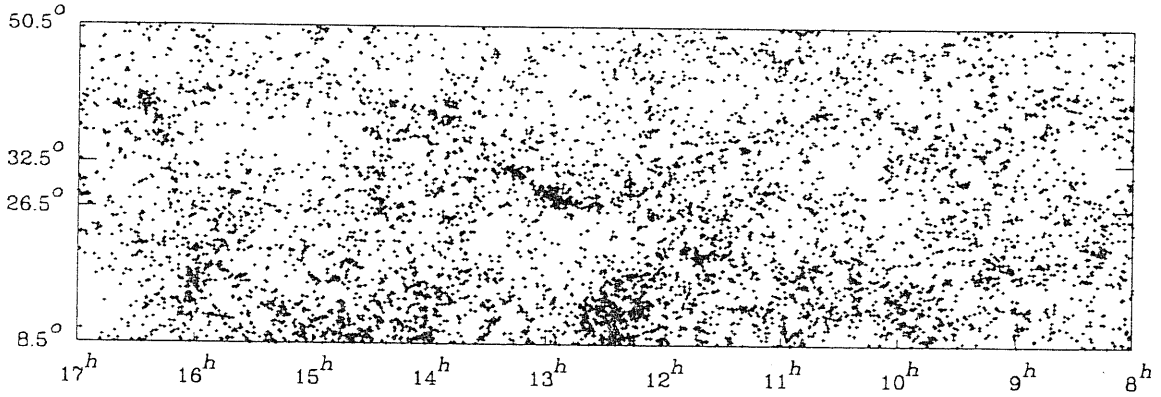

Fig.3.1 — The map of the 7031 objects with $m_B \leq 15.5$, listed by Zwicky *et al.* in the region bounded by $8^h \leq \alpha \leq 17^h$ and $8.5° \leq \delta \leq 50.5°$. Taken from de Lapparant *et al.* (1986).

Though the 2-D maps have already clearly shown prominent structures, the projection on 2-D must have smeared a lot of 3-D structures. An example is that a cell-like structure, which is of course very inhomogeneous, would have a quite smooth 2-D projection. 3-D maps with complete redshift information, therefore, should contain much richer information on the structures. In the Figure 3.2, we show the famous plot of the observed velocity versus right ascension for the 1061 galaxies which are brighter than $m_B = 15.5$ and with velocities less than 15,000 km s^{-1} in the full 6° thick slice(from de Lapparant *et al.* 1986). The most striking features of the figure are several large regions almost devoided of galaxies and the sharpness of the boundaries of the high density regions which surround the voids. Combining the other two neighboring slices and comparing these surveys with the 2-D plot (Fig.3.1), Geller & Huchra (1988) strongly argue for a bubble-like structure, *i.e.*, the galaxies are distributed on the surfaces of shells tightly packed next to each other(see also, Joeveer & Einasto 1978). However, other studies show that galaxies are distributed as a hierarchy of clusters(*e.g.* Soneira & Peebles 1977; Bhavsar 1978 & 1980), a network

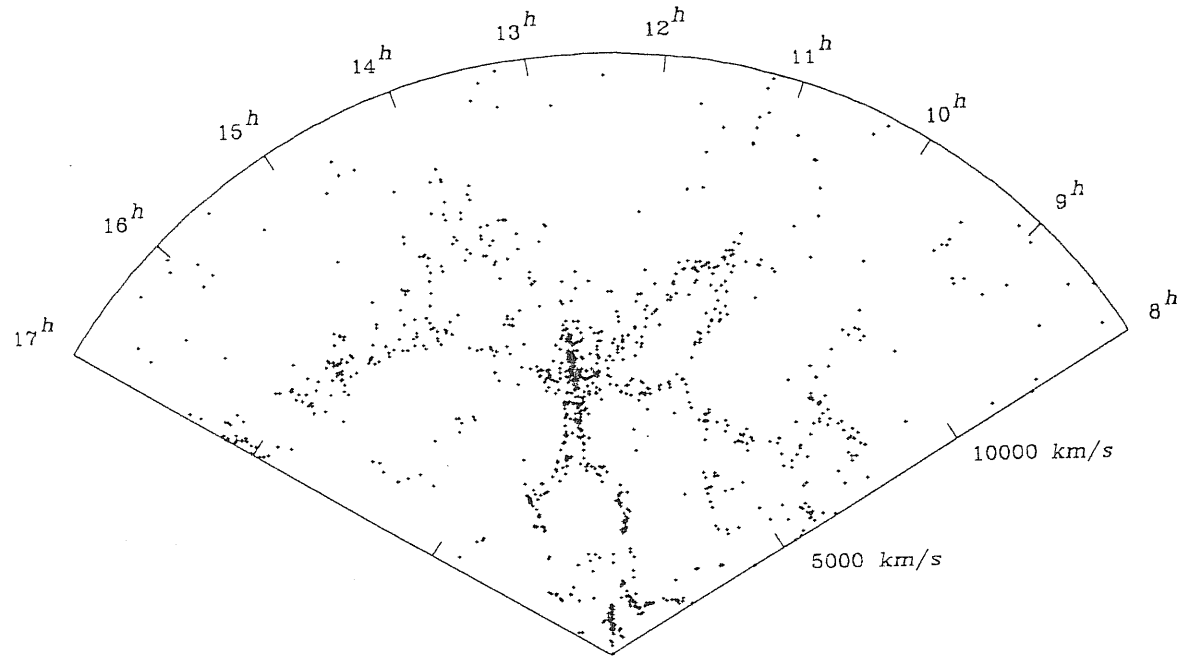

Fig.3.2 — Map of the observed velocity plotted vs. right ascension in the declination wedge $26.5° \leq \delta \leq 32.5°$. The 1061 objects plotted have $m_B \leq 15.5$ and $V \leq 15,000$ km s^{-1}. Taken from de Lapparant *et al.* (1986).

of filaments(Einasto *et al.* 1984; Haynes & Giovanelli 1986; Bhavsar & Ling 1988), or a sponge like topology(*e.g.*, Gott *et al.* 1986).

To quantify these clustering features and to test theoretical models, we need objective and free-of-bias statistical measures. An *ideal* statistic of clustering should have following features:

1.) On the observational side, the statistic should be able to quantify the clustering strength and coherence length, as well as the geometry and topology;

2.) On the theoretical side, it should be a good discriminant between different theories of galaxy formation;

3.) From the practical point of view, the statistic should be well defined and should be easily applied.

Several statistical measures have been frequently used in the studies of the large scale structure of the Universe. They are:

1.) N-body correlation functions;

2.) Void probability functions;

3.) Minimal-spanning trees;

4.) Topological analysis;

5.) Percolation analysis.

Each method has its pros and cons, and they are often used complementarily. In the following sections, I shall present the basic features of these methods, their main

results(observational and theoretical), their main success and failures, etc.

3.1 Correlation function analysis

Correlation function analysis is still the most important statistical tool in the LSS studies. A full account of N-body correlation functions can be found in the excellent book by Peebles (1980). Here we shall only summarize up the basic points, which will be referred in the following chapters. Main results regarding galaxy clustering will be presented in the next section.

3.1.1 Two-point spatial correlation function

The two-point correlation function is defined by writing the joint probability, d^2P, of finding each object in two volume elements dV_1 at $\vec{r}_1$ and dV_2 at $\vec{r}_2$ as:

$$d^2P = n(\vec{r}_1)n(\vec{r}_2)[1 + \xi(\vec{r}_1, \vec{r}_2)]dV_1 dV_2, \tag{3.1.1}$$

where $\xi(\vec{r}_1, \vec{r}_2)$ is the two-point correlation function, and $n(\vec{r})$ is the *expected* number density at position $\vec{r}$. In the LSS studies, the cosmological principle tells us that $\xi(\vec{r}_1, \vec{r}_2)$ is only a function of the pair separation $r_{12} = \mid \vec{r}_1 - \vec{r}_2 \mid$, *i.e.*, $\xi(\vec{r}_1, \vec{r}_2) = \xi(r_{12})$ (however, cf. Pietronero 1987).

Now let $DD(r)$ be the pairs of objects within the separation range $r \sim r + \Delta r$ in the observed sample, and $RR(r)$ the corresponding pairs in a random sample which has the same boundaries and selection effects as the real sample. By integrating eq.(3.1.1), we can easily find

$$\xi(r) = \frac{DD(r)}{RR(r)} - 1. \tag{3.1.2}$$

The meaning of $\xi(r)$, clearly shown by eq.(3.1.2), is the excess of pairs of objects, relative to the random distribution, therefore its value reflects the degree of clustering at scale r.

Equation (3.1.2) also provides us with the base of estimating $\xi(r)$. We construct a large set of random samples, or equivalently one random sample of much higher density. Each random sample should have the same boundaries and same observational selection effects(*e.g.*, magnitude- or diameter-limited; galactic extinction; variations in plate sensitivity, *etc.*)as the observed sample. Then we count pairs in a given separation range in both the observed sample and the random one and finally we can obtain $\xi(r)$ through eq.(3.1.2).

3.1.2 Three-point spatial correlation function

In the same way as for $\xi(r)$, we can define the three-point correlation function. The joint probability, d^3P, of finding three objects concentrated in each of the three volume elements dV_1, dV_2 and dV_3, separated by r_{12}, r_{23} and r_{31} can be written as:

$$d^3P = n(\vec{r}_1)n(\vec{r}_2)n(\vec{r}_3)[1 + \xi(r_{12}) + \xi(r_{23}) + \xi(r_{31}) + \zeta(r_{12}, r_{23}, r_{31})]dV_1 dV_2 dV_3, \tag{3.1.3}$$

where $\zeta(r_{12}, r_{23}, r_{31})$ is the three-point correlation function, and $n(\vec{r}_i)$ the *expected* number density at position $\vec{r}_i$ of dV_i

Integrating the equation (3.1.3), we can easily find,

$$\zeta(r_{12},r_{23},r_{31}) = \frac{DDD(r_{12},r_{23},r_{31})}{RRR(r_{12},r_{23},r_{31})} - 1 - \xi(r_{12}) - \xi(r_{23}) - \xi(r_{31}), \qquad (3.1.4a)$$

or equivalently,

$$\zeta(r_{12},r_{23},r_{31}) = \frac{DDD(r_{12},r_{23},r_{31}) - DDR(r_{12},r_{23},r_{31})}{RRR(r_{12},r_{23},r_{31})} + 2, \qquad (3.1.4b)$$

where $DDD(r_{12},r_{23},r_{31})$ is the count of triplets with shapes (r_{12},r_{23},r_{31}) in the observed sample, $RRR(r_{12},r_{23},r_{31})$ the *expected* count in a random sample, and $DDR(r_{12},r_{23},r_{31})$ the *expected* count of triplets formed by two real objects and one random point.

The direct estimations of ζ usually are based on the equations (3.1.4), through counting triplets DDD, DDR and RRR. If the two-point function can be determined quite accurately, it is wise to use eq.(3.1.4a), since we can save a lot of computational time needed to obtain DDR. Otherwise eq.(3.1.4b) should be used.

In analogy with the procedure of defining ζ, we can also define other higher-order (*e.g.*, 4-body, 5-body, ...) correlation functions. Since the direct determination for extragalactic objects of the four-point or higher-point functions is rather uncertain at the present(see, *e.g.*, Groth & Peebles 1977; Sharp *et al.* 1984), we will not go further. Instead we will discuss the transformation equation between angular and spatial correlation functions.

3.1.3 Limber's equation

Since most of the extragalactic-object catalogues give only positions on the sky, and the completion of large redshift surveys (a few thousand for galaxies; a few hundred for clusters) usually takes several years to be completed even today, most of our knowledge about correlation functions is still based on two-dimensional samples. In this case, angular correlation functions are defined in exactly the same way as the spatial ones, and we shall not repeat them. One of the most remarkable features of the correlation analysis is that the spatial and angular correlation functions are related by the so-called 'Limber's equation'. From the Limber's equation, we are able to extract information on the spatial functions, which reflect the real clustering properties, from the angular ones.

Usually the two-point and three-point angular functions are denoted by $\omega(\theta)$ and $z(\theta_{12},\theta_{23},\theta_{31})$. Assuming that the radial selection function is $\phi(r)$ and using the small angle approximation, the relation between $\omega(\theta)$ and $\xi(r)$ reads(see, Peebles 1980)

$$\omega(\theta) = \frac{\int_0^\infty \phi^2(r) r^4 dr \int_{-\infty}^\infty \xi(\sqrt{u^2+r^2\theta^2}) du}{[\int_0^\infty \phi^2(r) r^2 dr]^2}. \qquad (3.1.5)$$

For a special case where $\xi(r)$ is a power law, $\xi(r) = Br^{-\gamma}$, then eq.(3.1.5) shows that $\omega(\theta)$ must be also a power law $\omega(\theta) = A\theta^{-\beta}$. Furthermore their slopes and amplitudes are connected by

$$\gamma = \beta + 1, \qquad (3.1.6a)$$

and

$$A = B\frac{\int_0^\infty \phi^2(r)r^{5-\gamma}dr}{[\int_0^\infty \phi^2(r)r^2\,dr]^2}\frac{\Gamma(1/2)\Gamma(\beta/2)}{\Gamma(1+\beta/2)}. \qquad (3.1.6b)$$

The observational studies have shown that the two-point correlation functions of galaxies, groups and clusters closely obey the power law with $\gamma \approx 1.8$ (*e.g.*, Davis & Peebles 1983, Groth & Peebles 1977 for galaxies; Jing & Zhang 1988 for groups; Bahcall & Soneira 1983 for rich clusters; more details in the next section), therefore the simple relations (3.1.6) are very relevant to the LSS studies.

A general relation between $z(\theta_{12},\theta_{23},\theta_{31})$ and $\zeta(r_{12},r_{23},r_{31})$ can also be easily derived. Instead of presenting this general relation, we now consider a special case where $\zeta(r_{12},r_{23},r_{31})$ is of the hierarchical form, *i.e.*,

$$\zeta(r_{12},r_{23},r_{31}) = Q[\xi(r_{12})\xi(r_{23}) + \xi(r_{23})\xi(r_{31}) + \xi(r_{31})\xi(r_{12}]. \qquad (3.1.7)$$

In the power law model of ξ, the transformation predicts that $z(\theta_{12},\theta_{23},\theta_{31})$ must also be a hierarchical form

$$z(\theta_{12},\theta_{23},\theta_{31}) = q[\omega(\theta_{12})\omega(\theta_{23}) + \omega(\theta_{23})\omega(\theta_{31}) + \omega(\theta_{31})\omega(\theta_{12}]. \qquad (3.1.8)$$

Furthermore, Q and q are simply related by

$$\frac{q}{Q} = \frac{(\int_0^\infty r^{8-2\gamma}\phi(r)^3dr)(\int_0^\infty r^2\phi(r)dr)}{(\int_0^\infty r^{5-\gamma}\phi(r)^2dr)^2}. \qquad (3.1.9)$$

Interestingly enough, this model agrees very well with the observations of galaxies and clusters in great detail(e.g., Groth & Peebles 1977, Efstathiou & Jedrzejewski 1984 for galaxies; Jing & Zhang 1989, Tóth *et al.* 1989 for clusters; more details in the next section)

Several important points must be stated here. 1). The Limber like equations are the projection of the spatial functions to angular ones. To acquire the spatial functions, some specific models (as eqs. 3.1.6—3.1.7) have to be assumed in advance and then later be tested by two- and three-dimensional data. Certainly the inversions of Limber equations can overcome this limitation. However, as shown by Fall and Tremaine (1977) and Parry(1977) for the two-point correlation function, such an inversion is complicated and is unstable against statistical fluctuations. For higher order correlations, the inversions would become even more complicated and unstable, unless some specific forms, such as power laws, are assumed (Tóth *et al.* 1989). 2). All the above discussions assume an Euclidean space, which is valid for samples of redshift much less than 0.1. For deep samples, the effects of space curvature must be considered in the Limber equations. A full treatment of the relativistic effects has been given in Peebles(1980). 3). The value B is quite sensitive to the sample depth, to the shape of the selection function, and to the relativistic corrections, while the ratio q/Q are independent of the sample depth and insensitive to the selection function and the relativistic corrections. 4). The selection function is usually obtained from the luminosity or diameter functions of galaxies, or from the space density of objects.

3.1.4 The scaling relation

Another striking property of the correlation functions is the so-called 'scaling relation'. If the characteristic sample depth is D, on the small angle approximation, we have the following scaling(Peebles 1980):

$$\omega(\theta) = D^{-1}W(\theta D), \tag{3.1.10a}$$

The relation (3.1.10a) can be understood as follows. The correlation function $\omega(\theta)$ measures the ratio of the number of neighbors in excess of random to the number expected for a uniform distribution. If one counts neighbors in solid angle $\delta\Omega \propto D^{-2}$ at angular distance θD from a galaxy at distance D from the observer, one is looking at a fixed projected area at the galaxy and a fixed projected distance from the galaxy, so the number of correlated neighbors seen is independent of D while the number of accidental neighbors from the foreground and background is proportional to D. Thus $\omega \propto D^{-1}$ at fixed θD.

The function $W(\theta D)$ depends both on the spatial correlation function and on the shape of the selection function. For each kind of catalogue(e.g., magnitude-limited catalogue, diameter-limited catalogue), the shape of the selection function is fixed. So for two samples of depths D_1 and D_2, their angular correlation functions $\omega_1(\theta)$ and $\omega_2(\theta)$ are related by

$$\omega_1(\theta) = \frac{D_2}{D_1}\omega_2(\theta\frac{D_1}{D_2}). \tag{3.1.10b}$$

If the two-point function $\omega(\theta)$ is a power law $\omega(\theta) = A\theta^{-\beta}$, as observed for galaxies and clusters, we can easily find:

$$A \propto D^{-(1+\beta)}. \tag{3.1.10c}$$

Equations(3.1.10) are frequently used to test the reality of detected ω signals (see, Peebles 1980; Bahcall 1988b) and to test the volume dependence or the fractal property (Einasto *et al.* 1986) of galaxy clustering (e.g., Peebles 1980; Jing *et al.* 1991a).

3.1.5 A brief outline of estimation techniques and error analysis

The techniques, employed for estimating correlation functions, can be divided roughly into two types: the *direct counting method* and the *moment method.*

The direct counting methods for estimating two- and three-point correlation functions have already been given in §3.1.1 and §3.1.2. There the description for estimating two-point function is almost complete. However, since ζ (or z) is a function of three variables r_{12}, r_{23}, r_{31} (or $\theta_{12}, \theta_{23}, \theta_{31}$), its functional form is much more hidden than for ξ (or ω). The general method to study the sides dependence of $\zeta(r_{12}, r_{23}, r_{31})$ is described in Peebles & Groth (1975). However, if we want to test models of ζ or/and to find out some parameters, the least-square fitting of triplets count is more suitable(Tóth *et al.* 1989; Jing *et al.* 1991a; Borgani *et al.* 1991; Plionis *et al.* 1991). More details of these two methods will be presented along with our original work in Chapter 4 and Chapter 6.

Since the $(n-1)$-moments of the neighbor counts are related with the integrals of correlation functions up to n-points(§36, Peebles 1980), we are certainly able to get correlation functions from the moments(see,e.g., Peebles 1975; Peebles 1980; Sharp *et al.* 1984).

The main advantage of this method is that it can save a lot of computational time in estimating high-order correlation functions. The disadvantages are 1.)the functional forms for correlation functions have to be first assumed and then checked; 2.)unless only a single large shell is taken(but in this case, the assumed model can not be checked), it losses a lot of information on configurations, based on which correlation functions are extracted. The first point is rather obvious. To illustrate the second point, we take an example of the three-point function and of the second moments estimated in thin shells. The information of the three-point function is, of course, contained in *all possible triplets*, however the second moment only explores the *triplets with roughly two equal sides* (the shell radius).

Therefore, in my opinion, the direct counting method is favored to study samples of moderate size (without any requirement on *a priori* knowledge of correlations), while the moment method is suitable to study the samples of very large size(e.g., numerical simulations) with (or to test) *a priori* knowledge of correlations.

The errors, in the correlation analysis, can be divided roughly into two types: systematic errors(e.g., systematic variations in plates sensitivity; a sample biased due to the dominance of a supercluster or a void) and statistical fluctuations. The former type of errors is rather difficult to estimate if we only have one sample. The error estimates mentioned in literature are usually meant to estimate the later type of error. This is now generally thought to be well estimated by the bootstrap resampling technique(hereafter, BRT)(Barrow *et al.* 1984; Ling *et al.* 1986). In the BRT approach, the error is given by the standard variation of a large set of pseudo-samples, each of which is produced by randomly choosing N points, with replacement, from the original sample of N points. H.J. Mo in Munich has proved analytically that the BRT error is $\sqrt{3}$ times of Poissonian error for two-point correlation function and $\sqrt{7}$ times for the three-point function (private communication, 1991), so we do not need to spend a lot of computational time to estimate BRT errors. His conclusion was confirmed by his own check of the CfA sample(Huchra et al. 1983) as well as by my check of numerical simulations made by R. Valdarnini. Furthermore my analysis of the simulations shows that the BRT does give a good estimate of sampling errors in correlation analysis — this is the first direct evidence supporting BRT as a fair estimate of sampling error in clustering studies. The results of Mo and mine will be combined in a future paper (Mo and Jing, 1991).

3.1.6 A summary of main features of correlation functions

Correlation functions are still the most major measure of large-scale clustering in the Universe. In respect to other clustering measures, correlation analysis has its own advantages and disadvantages.

As has been seen above, the correlation functions cab easily be defined, with no any ambiguity. Their meaning, as clustering measures, is obvious, and the clustering strength and coherence length can be easily quantified. it is rather convenient to apply this measure to both 3-D samples as well as 2-D samples. The angular correlation functions can be related with the spatial ones through the Limber equations. And the scaling relations of angular functions of different depths are a convenient test of clustering reality and universality. At least two- and three-point functions of galaxies and clusters obey the simple power-law and hierarchical forms. These functions, regarding different 2-D and 3-D samples, have good reproducibility.

The correlation functions are simple to analyze in theoretical studies, and are sensitive (at least in principle) to the model details. The two-point correlation function is the inverse Fourier transformation of the *density power spectrum*. Different models of galaxy formation have different power spectra, which are even more distinguishable in the linear regime(*i.e.*, $\xi(r) \ll 1$). Furthermore, the models with Gaussian fluctuations predict a vanishing three-point function in the linear regime. The particular form of three-point function is predicted at the high biasing level for the models of Gaussian and non-Gaussian fluctuations.

Though correlation functions only measure the spatial patterns of galaxy distributions, they can be easily related with the dynamics on the large scale through the BBGKY hierarchy. Very useful equations have been derived, such as the Cosmic Energy Equation and the Cosmic Virial Theorem, which are important in understanding the origins and evolution of LSS. These equations are also the important sources from which the density parameter Ω of the Universe can be estimated.

In comparison with the above advantages, the disadvantages are minimal but not negligible. In principle, a full statistical description of a spatial point distribution needs the knowledge of *all* n-point correlation functions. In contrast, our present determination of even the 4-point function for galaxies and clusters is still rather uncertain. Furthermore, the low-order(2- and 3-point) correlation functions are not sensitive to the presence or absence of filamentary, bubble-like, sponge-like structures *etc.*. Therefore, correlation analysis, in practice, is unable to tell us anything about the topology and geometry of the distributions. In respect with high-order clustering, other measures (see §3.3 – 3.4) are more robust than the correlation functions.

3.2 The results of correlation analysis and confrontations with theories

In this section I shall summarize the results obtained from the correlation analysis, and outline how to use these results to constraint the current theories.

3.2.1 Two- and three-point correlation functions of galaxies

The two-point angular correlation function of galaxies at the small angular scale is well represented by a power law,

$$\omega(\theta) = A\theta^{-\beta}, \qquad \beta \simeq 0.77. \tag{3.2.1}$$

The first reliable determinations of this relation were from the statistical studies of Peebles and his coworkers on the Lick and Zwicky catalogues(Groth & Peebles 1977; references therein). These two samples are magnitude limited and are in the northern hemisphere. Our recent study of the ESO/Uppsala catalogue confirms that eq.(3.2.1) is also valid for the southern diameter-limited galaxy sample(Jing *et al.* 1991a). The conversion of eq.(3.2.1) to the spatial correlation function, through the Limber equation, yields,

$$\xi(r) = (r_0/r)^\gamma, \qquad \gamma = 1 + \beta \simeq 1.77 \tag{3.2.2}$$

with $r_0 \simeq 5h^{-1}$Mpc for $r \leq 10h^{-1}$Mpc(Groth & Peebles 1977; Jing *et al.* 1991a). This estimate is roughly consistent with the results based on redshift surveys(Davis & Peebles 1983; Bean *et al.* 1983; Davis *et al.* 1988; but see de Lapparent *et al.* 1988).

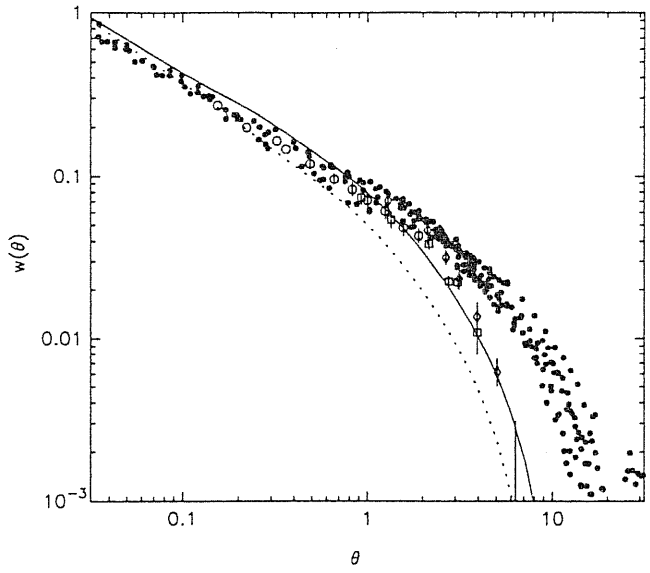

Fig.3.3 — The filled circles show the estimates of $\omega(\theta)$ of Maddox *et al.* (1990a) scaled to the Lick depth. The open symbols show $\omega(\theta)$ for the Lick catalogue from Groth & Peebles (1977). The dotted and solid lines show computations of $\omega(\theta)$ based on the CDM model with $h = 0.5$ and $h = 0.4$. Taken from Maddox *et al.* (1990a).

Now a new generation of large, uniform and machine-scanned catalogues of galaxies is emerging(Maddox *et al.* 1990a; Collins *et al.* 1989; Picard 1991). These catalogues are better defined and subjected to less artificial biases than the previous 'eye' selected catalogues. Maddox *et al.* (1990a) measured $\omega(\theta)$ for the APM catalogue, their results confirm the power-law (3.2.1) at the small scales as well as the break from the power-law at roughly the same physical separation as found previously. However, their $\omega(\theta)$ decline more gently from the power law on larger scales and they argue Groth & Peebles(1977) may have removed some intrinsic clustering when correcting for large-scale gradients in the Lick counts (see also Plionis 1988; Brown & Groth 1989). Their results are plotted in Fig.3.3.

To study $\xi(r)$ in theories at the range of $r \leq 10h^{-1}$Mpc, N-body simulations are needed in order to follow the nonlinear evolution of density perturbations. Though the power law form of $\xi(r)$ with the observed slope and amplitude is not a trivial prediction in the theories of galaxy formation, most current attractive scenarios reproduce this form without difficulty at certain epoch of evolution. So the power law is not a good discriminant between theories. Instead it is usually used to identify the present time in the simulations, so that the models could be further tested by other statistical measures.

As stated in §3.1.6, the function $\xi(r)$ at large scales (*i.e.* where $\xi(r) \ll 1$) is related by linear perturbation theory to the primordial fluctuation power spectrum. The new features of $\omega(\theta)$ revealed by Maddox *et al.* (1990a) on large angular scales, are important for testing theories of the formation of large-scale structures. In particular, comparing with the $\omega(\theta)$ predicted by the N-body simulations of the 'standard' biased CDM models(White *et al.*

1987), Maddox *et al.* (1990a) conclude that the CDM models have insufficient large scale power (Fig.3.3).

Efstathiou *et al.*(1990) performed estimates, for the QDOT redshift survey of *IRAS* galaxies, of the variance σ^2 which is related to the $\xi(r)$ according to

$$\sigma^2(l) = 1/V^2 \int_{V=l^3} \xi(r_{12}) dV_1 dV_2.$$

Their results are plotted in Fig.3.4. The strong non-zero σ^2 at $l = 30, 40h^{-1}$Mpc provide us with another new evidence for large scale structure. They also estimated σ^2 in the CDM models of White *et al.* (1987), which are given in Fig.3.4 too. Clearly, there is more large-scale power in the galaxy distribution than in the models.

Maddox *et al.*(1990a) and Efstathiou *et al.*(1990) tested the CDM models by comparing the observations with the N-body simulations. I found, as expected, such tests can be done analytically, since the linear perturbation theory is valid in these regime. Using the same power spectrum as in White *et al.* (1987), I calculated $\omega(\theta)$ and σ^2 in the CDM model, which are given in Fig.3.5 and Fig.3.4. The analytical results repeat the simulation results with high precision, indicating these observations are good probes to the primordial power spectrum. I shall use these two measures together with recent determinations of flux dipoles and bulk motions, to test various possible models of Gaussian primordial fluctuations(Jing *et al.*, 1991c), thus narrowing the range of model parameters. Note it is unrealistic to use observations on the nonlinear scales to test a lot of models, since in this case we have to impose the N-body techniques which are time consuming.

Now we turn to the three-point function of galaxies. Based on the Lick and Zwicky catalogues, Groth and Peebles(1977) found that the galaxy angular three-point correlation function is well approximated by eq.(3.1.8) with $q \simeq 1.7$ at the physical scale $r \leq 10h^{-1}$Mpc. Thus the spatial three-point function must be represented by the eq.(3.1.7), and $Q \simeq 1.3$ from the Limber equation (3.1.9). The later studies based on redshift samples(Peebles 1981; Efstathiou & Jedrzejewski 1984) and on the ESO-Uppsala catalogue(Jing *et al.* 1991a; see Chapter 4 for details) result in a smaller $Q \simeq 0.8$, possible due to lack of prominent rich clusters in these samples.

The three-point correlation function is an independent probe of the origin of LSS. N-body simulations show a strongly scale-dependent Q in hot dark matter models(Fry & Melott 1985), a much weaker dependence in unbiased CDM models(Davis *et al.* 1985; Fry & Melott 1985), while biased CDM models have a Q that is essentially constant (Davis *et al.* 1985; Melott & Fry 1986) at the value $Q \simeq 1$. The recent study of Valdarnini & Borgani (1991), using several typical power spectra, also shows that the Q-test is sensitive to both the power spectra and the biasing prescription. However, the apparent difference of Q between 3-D and 2-D observational samples reminds us to be cautious in testing the current models.

3.2.2 The scaling test and the volume dependence of the correlation length

The scaling (3.1.10) of $\omega(\theta)$ with the sample depth is important as a test for possible systematic errors in the data (which would lead to spurious clustering) and for the limited sample sizes. Groth & Peebles(1977) discussed the scaling relation for Zwicky, Lick and

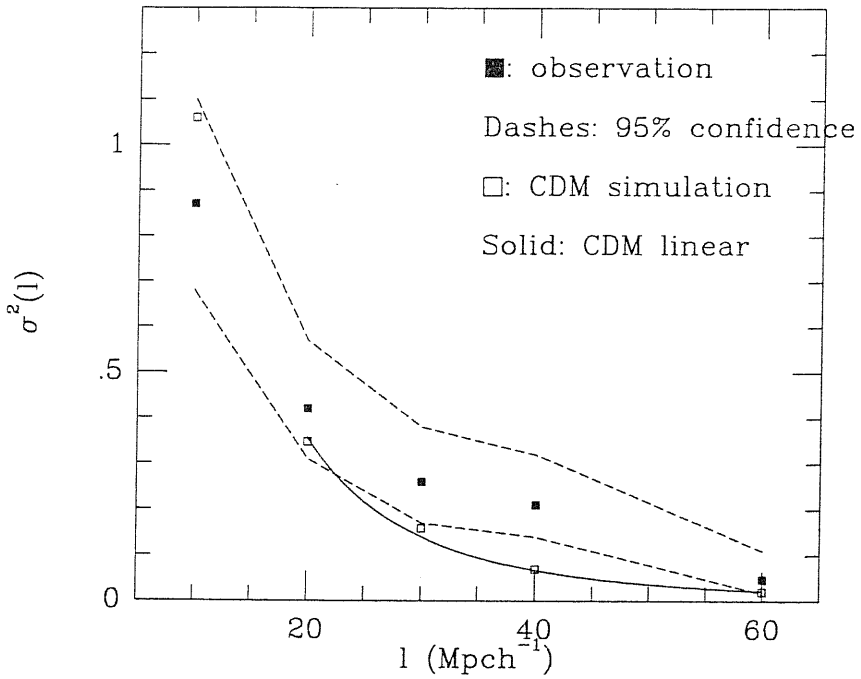

Fig.3.4 — The variances $\sigma^2(l)$ in the cubic volumes of size l. The filled squares are the results for the *IRAS* distribution, and the dashed lines represent the 95% confidence level. The empty squares are for the CDM simulations. All these data are taken from Efstathiou *et al.* (1990). The solid line represents the prediction by the author based on the linear perturbation theory(Jing *et al.*, 1991c).

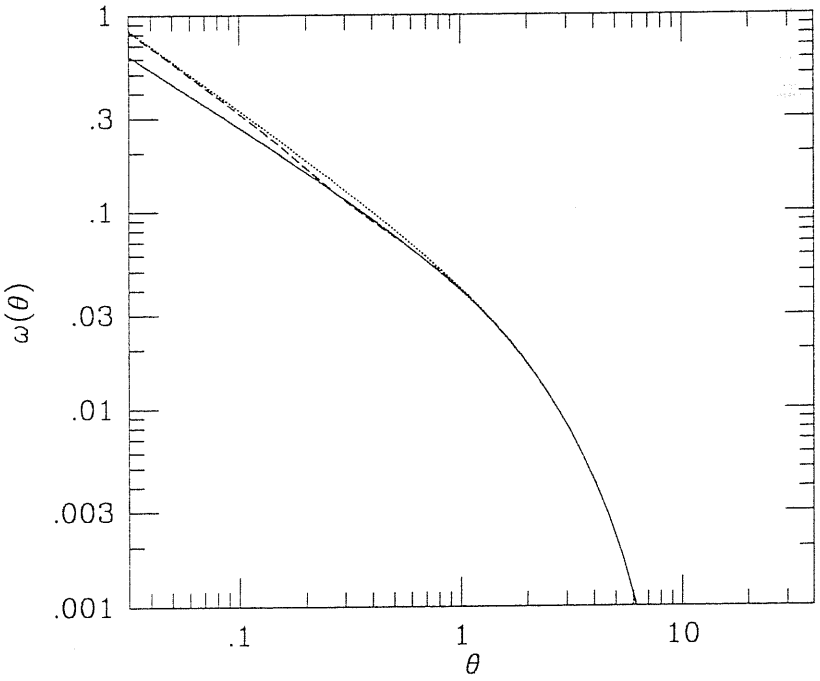

Fig.3.5 — The predicted $\omega(\theta)$ for the Lick catalogue in the CDM model with $h = 0.5$ based on the linear perturbation theory. The different lines correspond to different extrapolations of $\xi(r)$ at the small scales. The results are consistent with Maddox *et al.* (1990a) which used N-body simulations.(Jing *et al.*, 1991c).

Jagellonian catalogs, and found that the scaling is valid within a precision of 20% in amplitude. This uncertainty is expected because of the errors due to the luminosity function and sampling fluctuations. Recent estimates based on deep surveys, such as APM and Cosmos surveys(e.g., Maddox *et al.* 1990a&b), support the validity of the scaling. All this indicates the conventional value $r_0 \simeq 5h^{-1}$Mpc of the correlation length derived by Peebles and coworkers in 1970s is reliable and samples with size as that of the Zwicky and Jagellonian catalogs are fair for the two-point correlation analysis. Furthermore, systematic errors in the Zwicky, Lick and Jagellonian catalogs are not important for two-point correlation analysis at least on small scales(where $\xi(r) \geq 1$).

Einasto *et al.*(1986) claimed that the correlation length in the CfA redshift survey increases proportionally with the sample size, and that the effect is not a function of the intrinsic luminosity of galaxies(cf. §3.2.3). They argue rather that the available samples are far from being a fair sample of the universe. They estimate $r_0 = 10h^{-1}$Mpc for the true correlation length and a fair sample is reached if the CfA sample enlarges two times in the depth. Their results are an indication that galaxies are distributed in a fractal distribution possibly extending to $\sim 100h^{-1}$Mpc(Calzetti *et al.* 1988; Einasto *et al.* 1986; Pietronero 1987). However, the scaling tests of Groth & Peebles (1977) clearly oppose this idea.

The later detailed analyses of the nearby redshift samples(Davis *et al.* 1988; Börner & Mo 1990) point out that the effect found by Einasto *et al.*(1986) in fact is a combination of the sample-size dependence and the luminosity segregation(cf. §3.2.3). They estimate that in the skies surveyed by the CfA and SSRS, the increase of r_0 with the sample depth is significant only within the local region of depth less than $30h^{-1}$Mpc. Moreover, Davis *et al.* (1988) found no such effect in the all-sky survey of *IRAS* galaxies. Thus, these results argue against the existence of $\sim 100h^{-1}$Mpc fractal distributions in the Universe.

The effect on r_0 by the sample-size can also be studied by the scaling test of $\omega(\theta)$ in 2-D shallow catalogues. Since the samples of different depths are apparent diameter- or magnitude-limited, each sample has the same fraction of intrinsic bright and faint galaxies. Therefore, the luminosity segregation effect would not enter in such a study and the sample-size effect is isolated, in contrast with the analyses of 3-D samples. But the broad distribution of galaxies in the radial direction makes us able only to give a typical size where the sample-size effect could be effective.

Such a test has been done in our recent paper(Jing *et al.* 1991a). We selected samples with different limiting diameters from the southern ESO/Uppsala catalog. Our scaling test gives $r_0 = 5h^{-1}$Mpc as the correlation length of galaxies, consistent with most previous analyses of the northern samples. Furthermore, we did find a smaller r_0 for samples with depth less than $30h^{-1}$Mpc, giving support to the results of Davis *et al.* (1988) and Börner & Mo (1990).

3.2.3 Luminosity and morphology segregations, and biasing

Some theories of biased galaxy formation (*e.g.* Dekel and Silk 1986; White *et al.* 1987) predicted that the more luminous the galaxies, the more clustered they are, and that dwarf galaxies are even more uniformly distributed than normal ones and that they fill the regions devoided of bright galaxies. Many authors have studied the problem observationally but still with contradictory conclusions. Bothum *et al.* (1986), Thuan *et al.* (1987), Eder *et al.* (1989), Binggeli *et al.* (1990), and Thuan *et al.* (1991) found that there is no difference

between the dwarf-LSB(Low Surface Brightness) and the bright galaxy distributions, while Davis & Djogovski (1985), Giovanelli *et al.* (1986), Xia *et al.* (1986), Salzer *et al.* (1990) and Santiago & da Costa (1990) found that dwarf-LSB galaxies are less clustered than large HSB(High Surface Brightness) galaxies. Another set of studies based on CfA and SSRS samples conclude that there is a trend of increasing correlation length with luminosity in the subsamples of high brightness($\geq$ the characteristic brightness L_*) (Davis *et al.* 1988; Hollósi & Efstathiou 1988; Börner & Mo 1990), but this trend is not significant in the subsamples of lower brightness. The results were not conclusive because most of these studies suffered from various deficiencies. Note the sample used by Thuan *et al.* (1991) is the most complete, well-defined and largest one in these studies. If we make a judgement based on the completeness, size and quality of the samples used, our conclusion would be that galaxies of different luminosities (including dwarfs) have the same degree of clustering except that the brightest galaxies (brighter than L_*) are more clustered.

It has been known for a long time that early-type galaxies preferentially locate in rich dense regions and late-type ones in fields(*i.e.* the morphology segregation). The first statistical study of this effect was made by Davis and Geller(1976) based on the 2-D magnitude-limited($14.5m_b$) sample from UGC. They found that early type galaxies are more clustered than late types. The two-point correlation function is well approximated by a power law for each type, but the slopes are steepened from late to early types. These results are confirmed by Giovanelli *et al.*(1986) in their study of 2-D galaxy distribution in the Perseus-Pisces region. We made an independent test of this effect in the southern sky, using diameter-limited samples(Jing *et al.* 1991a). Our results support that late type galaxies are distributed more randomly, but show a weak dependence of the slope of $\xi(r)$ on morphology types. The studies of Börner & Mo 1990 and Santiago & da Costa (1990), using the CfA and SSRS redshift samples, reached the same conclusion as ours.

We are the first to study the morphology dependence of three-point function(Jing *et al.* 1991a). We found the hierarchical form (3.1.8) is a good approximation for each morphology type. The constant Q is roughly the same for the early types (E/SO) and late types(Sbc and later) as for galaxies in general, but it is much smaller for the early spirals(Sa, Sab, Sb). Redshift samples and larger 2-D samples are needed to clarify this effect.

All these observational results would be important inputs to the biasing mechanisms of galaxy formation. The results of Thuan *et al.* (1991) that the dwarfs/LSBs are good tracer of galaxy distribution, rule out a certain class of biased galaxy formation theories which predict a uniform spatial distribution of the dwarfs/LSBs. The observed morphology segregation and luminosity segregation at high luminosity, both at the large scales $r \approx 5$ to $10h^{-1}$Mpc, provide valuable evidence for biased galaxy formation. Since only 'crude' theories of biasing mechanisms are available, it is premature to link these results to some specific theories.

3.2.4 Correlation functions of rich clusters and groups

Among the many others(see references in Bahcall 1988b), Bahcall & Soneira(1983) analysed both the angular and the spatial two-point correlation functions for the clusters of Abell (1958) catalog. The $\xi(r)$ for $R \geq 1$ clusters turned out to be $\xi_{R\geq 1} = (25/r)^{1.8}$ for $r \leq 100h^{-1}$Mpc. Moreover, the two-point function for clusters of different richness

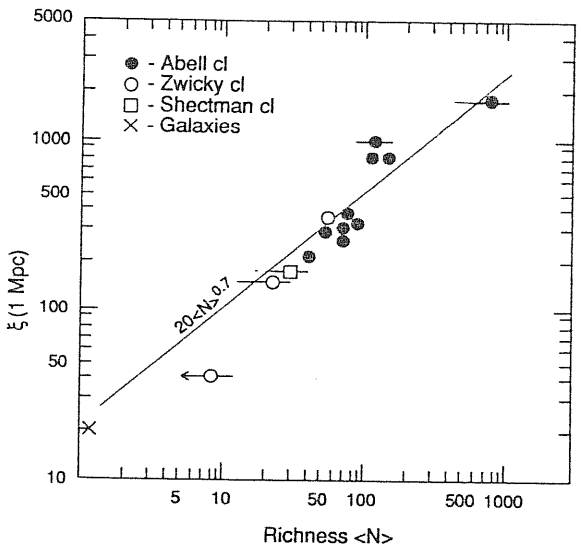

Fig.3.6 — The richness dependence of the amplitude. Taken from Bahcall (1988).

can be expressed by the power law form $\xi(r) = (r_0/r)^\gamma$ with the slope $\gamma = 1.8$ and the amplitude r_0 increased with the richness(see, Fig.3.6). The results have been confirmed by numerous other studies based on independent samples(*e.g.*, Huchra *et al.* 1990a; Batuski & Burns 1985; Kopylov *et al.* 1987; Postman *et al.* 1986; Shectman 1985; Gao & Jing, 1989; Batuski *et al.* 1989; Couchman *et al.* 1989; Plionis & Borgani 1991).

These statistical results have given important implications and constraints on theoretical models. The high amplitude of ξ_{cc} (relative to that of galaxies) and the richness dependence of r_0 indicate that the luminous systems in the Universe are not equivalent tracers of the structures. This feature, together with other observational facts (*e.g.*, huge voids like Bootes; the density parameter Ω always ~ 0.2 from the dynamical studies of galaxy distributions), led to the idea of biased galaxy formation (*e.g.*, Kaiser 1984; Bardeen *et al* 1986). The scale explored by ξ_{cc} is so large that ξ_{cc} is expected to reflect the primordial fluctuation spectrum. Its large amplitude as well as large coherence length are strong constraints on the flat models with the primordial Gaussian fluctuation. In particular, the 'standard' CDM model fails to reproduce the observed ξ_{cc}(*e.g.* White *et al.* 1987).

The crucial importance of the ξ_{cc} motivated people to check its reality carefully. Since the cluster catalogs up to date are all compiled by 'eye' from the two-dimensional plates, some fraction of clusters could be the results of superposition of foreground and/or background galaxies. If the effect happens due to the chance superposition of 'field' galaxies(*i.e.* those not related with other rich clusters included), the resultant artificial clusters form a random component in the spatial distribution, which produces an unchanged or even a reduced ξ_{cc}. In contrast, if the effect is correlated with the positions of other rich clusters(*i.e*, the 'halo' galaxies of foreground or/and background clusters), an enhanced spurious clustering is produced with its manifestation in the line-of-sight direction. Since the observed ξ_{cc} is high, most of the present concern is on the later effect. It has been in hot debate for several years whether the effect seriously enhances the ξ_{cc}(see §5.1 for a review). In

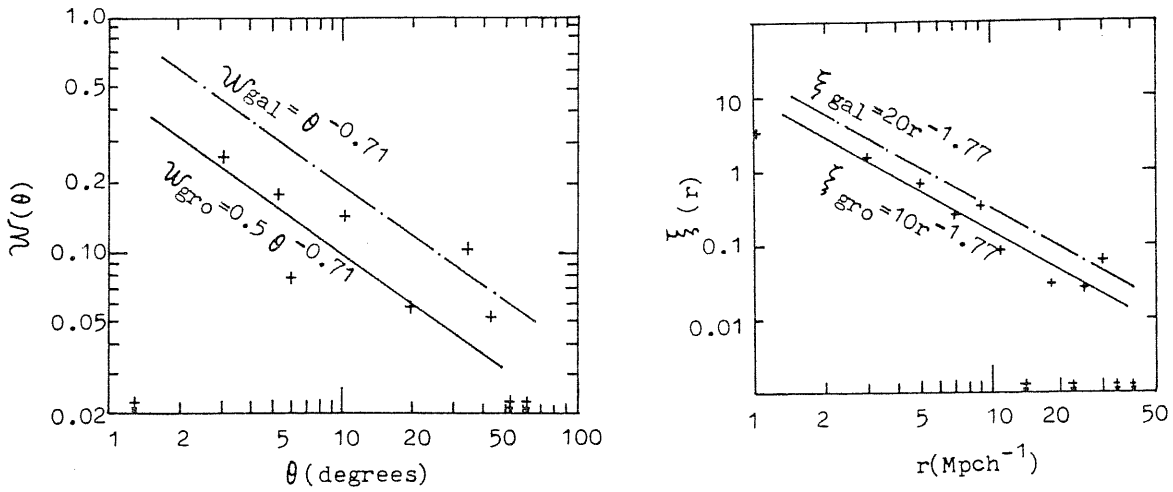

Fig.3.7 — The angular (a) and spatial (b) two-point correlation functions of CfA groups. The crosses are the statistical results, and the solid lines are the approximate fits to the data. The dot-dashed lines are the galaxy correlation functions: (a) $\omega(\theta)$ of $14.5m_b$ UGC catalogue; and (b) $\xi(r)$ of the CfA(From Jing & Zhang 1988).

our recent work by M. Plionis, R. Valdarnini and myself (Jing et al. 1991b), we showed *no evidence* for significant enhancement of ξ_{cc} by the contamination effect, thus supporting that the ξ_{cc} detected by Bahcall and Soneira(1983) is due to the real clustering (see Chapter 5).

Several authors have studied the group-group correlation function ξ_{groups} for those available catalogs of groups. J.L. Zhang and I (Jing & Zhang 1988) first analysed both the angular and spatial two-point correlation functions for the CfA groups(Geller & Huchra 1982). We found that ξ_{groups} can be approximated by $\xi_{groups} = Ar^{-1.8}$, with $A \simeq 10(h^{-1}\mathrm{Mpc})^{1.8}$ about half of the amplitude of galaxies, thus groups are more uniformly distributed in space than galaxies. These results have been confirmed by Maia & da Costa(1990) based on an independent group catalog selected from the SSRS survey(Maia *et al.* 1989). The analysis by Ramella *et al.* (1990) of their independent group sample selected from the CfA slice survey (Ramella *et al.* 1989), however found a larger amplitude which is as large as that of galaxies within the errors. The discrepancy between the last and the former two studies has not been well understood. One possible cause is suspected to be the different density thresholds $\delta\rho/\rho$ used in forming these catalogues: in the first two catalogues, $\delta\rho/\rho = 20$; in the last catalog, $\delta\rho/\rho = 80$.

The ξ_{groups} could be a powerful test of the theories. In the hierarchical gravitational theory, Kashlinsky (1987) predicts that poor groups (with turnaround mass less than $10^{14}M_{\odot}$) are less clustered than galaxies. The above results appear to support his model. However, I noted the criteria of defining groups are different between the observations and the theory, so we must be cautious in such a detailed comparison. More important perhaps is that we have reached the capability of simulating a galaxy sample as large as CfA and SSRS using N-body techniques and that exactly the same group-finding algorithms can

be applied to both simulations and observations. Thus a proper evaluation of models can be made based on group properties. The recent simulation study of Gaussian and non-Gaussian CDM models by Matarrese *et al.* (1991), shows that the ξ_{groups} is a sensitive discriminant of the models. However their selection criteria of groups, although similar to, not the same are as the previous studies of the observations. We are planning to explore the problem by employing exactly the same group-finding procedure both in N-body simulations and in observations(Jing & Valdarnini, 1991b).

The angular three-point correlation function of Abell clusters was first analysed by J.L. Zhang and the author (Jing & Zhang 1989) and independently by Töth *et al* (1989). Both studies yield a consistent result that rich clusters of galaxies, just like galaxies, obey the hierarchical form (3.1.7) with $Q \simeq 0.8$. Furthermore, after analysing clusters of richness $R \geq 2$, Jing and Zhang (1989) pointed out the hierarchical form is independent of cluster richness. These results have been further confirmed by the later analyses based on redshift complete, albeit small, samples of Abell clusters (Jing & Valdarnini 1991a; Gott *et al.* 1991). A detailed presentation of our analyses will be given in Chapter 6.

A definite form has been predicted for ζ_{ccc}(*e.g.*, Politzer & Wise 1984; Szalay 1988; Matarrese *et al.* 1986), if rich clusters form at high density peaks as guided by ξ_{cc}(Kaiser 1984). In the high peak approximation, Matarrese *et al.* (1986) showed

$$\begin{aligned}\zeta_{ccc}(1,2,3) = F(1,2,3) \times \{[\xi_{cc}(1,2)\xi_{cc}(2,3) + ...(3\text{terms})] + \xi(1,2)\xi(2,3)\xi(3,1)\} \\ + [1 - F(1,2,3)] \times \{1 + [\xi(1,2) + ...(3\text{terms})]\},\end{aligned} \tag{3.2.3}$$

where $F(1,2,3)$ depends on the fluctuation type. If the fluctuation is Gaussian, $F(1,2,3)$ is 1. The same factor $F(1,2,3)$ before the quadratic and cubic terms of ξ seems contradictory with the observations (Töth *et al.* 1989). However, the recent N-body simulation of the 'standard' CDM model(Gott *et al.* 1991) showed a surprising result: the clusters (high peaks) in the simulations do obey the hierarchical form. The discrepancy has not been well understood, though Gott *et al.*(1991) tried to interpret the hierarchical form as due to dynamical merges. I noted that their simulated sample of clusters is small and only one particular simulation (in fact they have done three) is used. In my opinion, further work both on analytical modeling and on simulations are needed to clarify this discrepancy.

In my recent papers (Jing 1990a & 1991), I explored the ξ_{ccc} in another distinct model of non-Gaussian fluctuation — the explosion scenario (*e.g.*, Weinberg *et al.* 1989). In this model, clusters form at the intersections of the bubbles. I found that the hierarchical form holds for the simulated clusters with a similar Q to that of the observations, and the results are not sensitive to the model details(see Chapter 7).

3.3 Void probability function

3.3.1 The general relation with N-point correlation functions

It was first shown by White (1979) that the probability that a given size and shaped volume V placed randomly in space be empty of objects is given by a sum over the correlation functions to all orders,

$$P_0 = \exp[\sum_{N=1}^{\infty} \frac{(-1)^N}{N} \overline{n}^N \int_V d^3\vec{x}_1 ... d^3\vec{x}_N \kappa_N(\vec{x}_1, ..., \vec{x}_N)], \tag{3.3.1}$$

where $\overline{n}$ is the average number density; $\kappa_N(\vec{x}_1,...,\vec{x}_N)$ are the irreducible N-point correlations of the objects. The equation can also be applied to two dimensional samples, if we replace $\overline{n}$, $\kappa_N(\vec{x}_1,...,\vec{x}_N)$ and V respectively by the surface number density, the N-point angular correlations and the surface area. Obviously, the measure is related with all N-point correlation functions.

3.3.2 A scaling property in the hierarchical distribution

In the hierarchical model, the irreducible N-point function $\kappa_N(\vec{x}_1,...,\vec{x}_N)$ is given by a symmetrized sum of connected products of $N-1$ two-point functions ξ, conveniently associated with tree graphs of N points(*e.g.*,Schaeffer 1984, Fry *et al.* 1989),

$$\kappa_N(\vec{x}_1,...,\vec{x}_N) = \sum_{(i=\text{all trees})} Q_N(i)\xi(r_1)...\xi(r_{N-1}), \tag{3.3.2}$$

where the product runs over the $N-1$ limbs connecting the N-points of the tree and the sum over all N^{N-2} distinct labeled trees. The current available statistical studies of low order correlation functions of both galaxies and clusters(see the last section), support that the model works in the Universe. It was also expected that the model might be valid in some theories under certain approximations(for details, see, *e.g.,* Fry *et al.* 1989).

As shown first by White(1979) and later by many others (*e.g.*, Sharp 1981; Fry 1984; Schaeffer 1984), in the hierarchical distribution, the void probability obeys a scaling,

$$\Sigma \equiv \frac{\ln P_0}{\overline{n}V} = \Sigma(q), \tag{3.3.3}$$

where $q \equiv \overline{n}V\overline{\xi}$ and $\overline{\xi} \equiv 1/V^2 \int_V \xi(r_{12})dV_1dV_2$. This says that the function Σ depends on the $\overline{n}$, ξ and V only through the combination q (usually called the scaling variable). As in §3.1.3, it can be easily shown that the 2-D projection of a 3-D hierarchical distribution is still hierarchical, thus the scaling relation holds also for 2-D samples, though the functional form of $\Sigma(q)$ is different for 2-D and 3-D cases(depending on the radial selection function).

3.3.3 The scaling properties in galaxy distributions— a summary of observations

In the LSS studies, there are many ways to test the scaling relation, as indicated by eq.(3.3.3) itself. For a 2-D sample, *e.g.*, a magnitude-limited galaxy sample, we can study whether the scaling is established by using different shaped area (*e.g.*, squares; circles), subsamples of different dilutions, and subsamples of different limiting magnitudes. The same method can also be applied to 3-D redshift samples. If the scaling does hold, Σ should only depend on the scaling variable q; otherwise Σ depends on the shape and the size of the volume (area) as well as on the number density.

The scaling property has now been examined for galaxies in great detail by a number of authors. Sharp (1981) first studied the scaling relation for the Zwicky catalogue of galaxies and found that the scaling is obeyed, so the data are consistent with a hierarchical distribution. The later analyses of the CfA redshift survey(Maurogordato & Lachiéze-Rey 1987; Mo & Börner 1990) and of the Giovanelli-Haynes redshift sample in the Pisces-Perseus region(Fry *et al.* 1989), using subsamples of different dilutions, confirmed the scaling found in 2-D studies. Furthermore, Maurogordato & Lachiéze-Rey(1987) and Fry

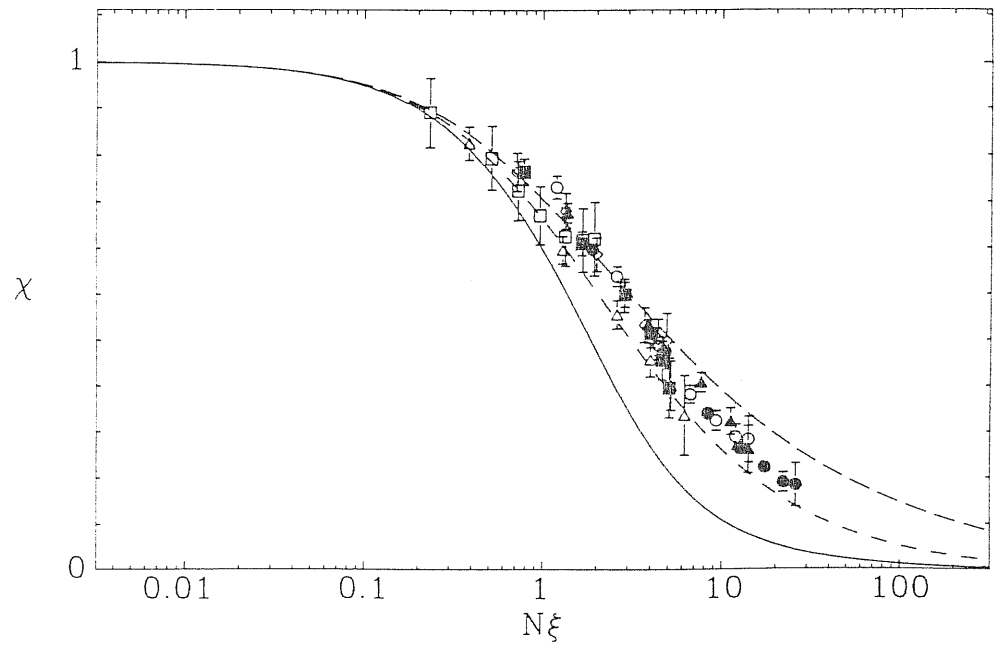

Fig.3.8 — The scaled void probability χ plotted against $\overline{N\xi}$ for the Perseus-Pisces catalog, showing the success of the scaling. The different symbols represent the subsamples of different luminosities and different dilutions. Taken from Fry *et al.* (1989).

et al. (1989) compared $\Sigma(q)$ for several samples of different luminosities, and found that $\Sigma(q)$ is independent of luminosity and is consistent with that of galaxies without luminosity division(see Fig.3.8). It was further found that the scaling relation is independent of galaxy morphology types(Mo & Börner 1990).

I noted two implications of this universal scaling. First, for galaxies as a whole, their high-order correlation functions are consistent with the hierarchical model (3.3.2), though the values of $Q_N(i)$ (for $N \geq 4$) have not been fixed yet. Second, galaxies of different morphology types and luminosities obey the same hierarchical model(3.3.2). This further implys that $Q_N(i)$ (for $N \geq 3$) is independent of morphology types and of luminosities. Our direct analysis of UGC and ESO/Uppsala catalogues (Jing *et al.* 1991a) did show a weak dependence of $Q_N(i)$ ($N = 3$) on morphology types.

3.3.4 The scaling properties in cluster distributions— a summary of observations

The scaling properties for rich clusters were first studied by the author (Jing 1990b), a detailed account of the work will be presented in Chapter 8. As a summary, I examined $\Sigma(q)$ for several cluster (2-D) samples of different depths and of different richness which are selected from the ACO catalog of rich clusters of galaxies. I found that the rich clusters also obey the scaling, and the scaling relation is independent of richness. So the distributions of rich clusters can be described by a hierarchical model, consistent with the statistics of three-point correlation function(see, §3.2.4). All the scaling features have been further confirmed by a recent analysis on small 3-D samples(Cappi *et al.* 1991), though the accuracy of their results is limited because of the small size of the 3-D samples.

As shown by Schaeffer (1987), the function $\Sigma(q)$ depends on the redshift selection

function weakly, thus making possible a comparison of $\Sigma(q)$ with that of galaxies even in 2-D samples. The studies of Jing (1990b) and Cappi *et al.* (1991) gave indication that galaxies and clusters obey the same scaling, though more detailed studies with larger redshift samples are still needed.

3.3.5 Theoretical implications

As we saw above, the hierarchical scaling is established both in the galaxy and in the cluster distributions, and it depends weakly on the intrinsic properties of these objects(such as, luminosity, morphology, richness). However, there is no *a priori* reason to expect the scaling necessarily to be followed, thus the observed scaling could become a strong constraint on the theories of galaxy formation.

Fry *et al.* (1989) have applied the statistics to numerical simulations of HDM and CDM inflationary models, initially Poisson models, and cosmic strings seeded models, in order to probe $\Sigma(q)$ of 'galaxies' in these models. They found that the simulation results obey the implied hierarchical scaling in many cases, but not in all. In particular, HDM models without biasing show the effect of a strong feature in the initial power spectrum. The cosmic string models exhibit scaling but do not agree well with the galaxy data. The rest of the models work well, implying that the initial fluctuation spectrum has a behavior closest to that in CDM models, or perhaps Poisson.

As discussed in §3.2.4, a hierarchical distribution, like eq.(3.3.2), is not expected for rich clusters in the simple analytical models in which 'clusters' are formed at high density peaks. But these analytical prescriptions may be too simple, so large N-body simulations are needed to clarify this point.

3.4 The Other Measures of High-order Clustering

As stated in the beginning of this chapter, three other measures depending on high-order clustering are frequently used in the LSS study. Because of the limited space of the thesis, I can only briefly discuss these measures. Despite of the brevity, I tried to keep the spirit of the previous sections: to summarize the basic features of each method and the main results obtained.

3.4.1 A topology measure — the genus-threshold density relation

Gott, Melott and their collaborators (Gott *et al.* 1989; and references therein) suggested that the genus of isodensity contours could be used as a quantitative measure of the topology of the large scale structure. The genus of the contour surface is defined by

$$G_s = (Number\ of\ holes) - (Number\ of\ isolated\ regions)$$

where "hole" means a hole like that in a doughnut and an isolated region may be above or below the threshold density.

Gott *et al.*(1986) showed that G_s is related to the integral of Gaussian curvature K over the contour surface

$$G_s = -\frac{1}{4\pi}\int K dA.$$

The relation makes it possible to measure the genus of a contour surface in catalogs of extragalactic objects and in simulations. The computer program has already been published in Melott (1990) and Weinberg (1988).

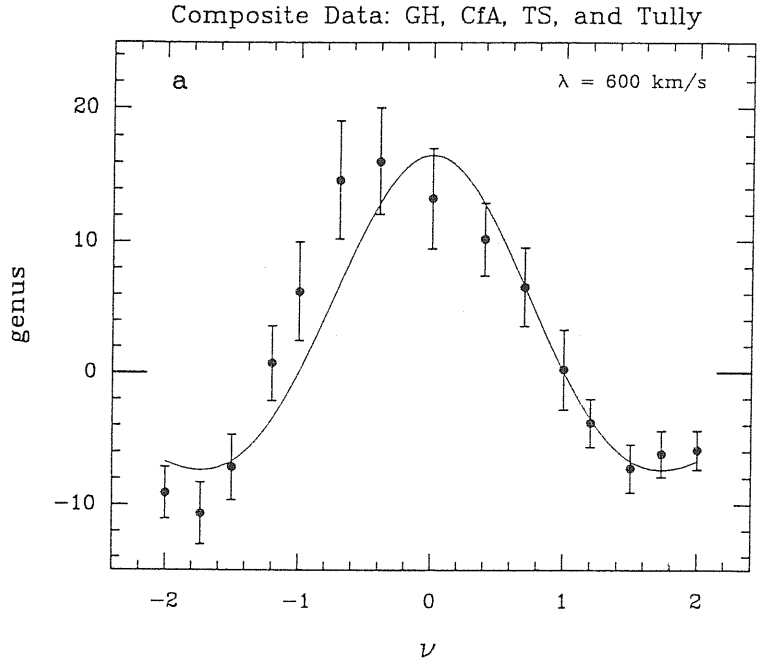

Fig.3.9 — The composite genus curve created by adding the (bootstrap average) curves from the Giovanelli and Haynes, CfA, dwarf and Tully samples, all smoothed at $\lambda \sim 600$ km s^{-1}. The best-fit random phase curve is shown for comparison. The curve shows a small shift to the left in the direction of a meatball topology. Taken from Gott *et al.* (1989).

In terms of density threshold ν (which is in unit of the standard deviation from the mean), Hamilton *et al.*(1986) showed that for Gaussian random fields, the mean genus per unit volume is given by

$$g_s = N(1-\nu^2)\exp(-\nu^2/2),$$

where

$$N = \frac{1}{(2\pi)^2}(\int k^2 P(k) d^3k/3 \int P(k) d^3k)^{3/2}.$$

So while the amplitude N of the genus curve depends on the *shape* of the power spectrum, the shape of the genus curve depends only on the density threshold ν, $g_s \propto (1-\nu^2)\exp(-\nu^2/2)$. Any deviation from this genus shape indicates a deviation from the Gaussianity. For example, the meatball structures will shift the peak of g_s to negative ν but the bubbly structures will shift it in the opposite direction.

In gravitational instability theories, the primordial Gaussian or non-Gaussian features remain in the linear regime. So the analysis of galaxy samples or/and cluster samples in the linear regime (*i.e.*, $r \geq r_0$), can in principle determine whether primordial fluctuations are of a Gaussian or a non-Gaussian nature. The shape of the primordial power spectrum, if Gaussian, can be further constrained by the observed amplitude N.

Gott *et al.* (1989) analysed most available redshift samples of galaxies and clusters and found that the distribution of these objects on linear scales is approximately Gaussian with

slight meatball shifts(see Fig.3.7). Such similar shifts also show up in CDM simulations due to a combination of biasing and sampling effects. Notice that these shifts are in the opposite direction to what expected in a bubble model, thus there is no evidence for the existence of bubbles from this quantitative study. The main results of their model tests are that, while the HDM model is consistent with the observation data, the standard CDM model seems the most successful one in explaining the observed genus-density relation.

A 2-D equivalent, the Euler-Poincáre characteristic (Adler 1981; Coles 1988) has been also applied to the study of the LSS (Coles & Plionis 1991), using the largest available galaxy catalogue, the Shane & Wirtanen catalogue. The results support that in the mildly non-linear regime the topology approaches that of a meatball, but in the linear regime the topology is indistinguishable from that of a Gaussian field, consistent with the 3-D study of Gott *et al.* (1989).

3.4.2 Minimal spanning trees

Any distribution of points in space is associated with a unique structure, the so-called 'Minimal Spanning Tree' (or MST)(Barrow *et al.* 1985). The MST picks out the dominant pattern of connectedness in a manner that emphasizes its intrinsic linear associations, so it is mostly useful in studying the properties related with 'filamentary' structure (Bhavsar & Ling 1988). Since the MST depends on the high order clustering, some quantitative properties of the MST can be defined and then calculated for comparative purposes, so as to discriminate between theories which have similar low-order clustering(Barrow *et al.* 1985). Now we describe the definition and construction of the MST, following Barrow *et al.* (1985).

Our data set is termed a *graph* which will be composed of *nodes* (galaxies), *edges* (straight lines joining galaxies) and *edge-lengths* (distances between galaxies). A sequence of edges joining nodes is a *path*; a closed path is called a *circuit* and a graph will be called *connected* if there is a path between any pair of nodes. The number of edges emanating from a node is call its *degree*. A connected graph containing no circuit is a *spanning tree*. The length of a tree is defined to be the linear sum of the lengths of its component edges. The *minimal spanning tree* (MST) is the spanning tree of the minimum length. The MST will be unique, if no two edges have a equal length. A *k-branch* is a path of k edges connecting a node of degree 1 to a node of degree exceeding 2 with all intervening nodes of degree 2.

The simplest algorithm to construct explicitly the MST of a graph, Γ, first picks an arbitrary node of Γ and then adds the connected edge of smallest length. This edge and the two nodes at its ends form the first *partial tree*, Π_1. The kth partial tree, Π_k, is formed by adding to Π_{k-1} the shortest edge connecting Π_{k-1} to any nodes of Γ not already in Π_{k-1}. If Γ contains n nodes then Π_{n-1} is the required MST.

In order to distill the dominant features of the MST, two further reducing operations, *pruning* and *separating*, on the MST can be performed.

1). Pruning: An MST is pruned to level p when all k-branches with $k \leq p$ have been removed.

2). Separating: Remove from the MST any edges whose length exceeds some cut-off l_0.

Bhavsar and Ling (1988) showed that the MST, combined with the data permuting technique, is a successful filament-finding algorithm which can identify the filaments and

determine their statistical significance (physical associations or chance alignments of small clustered objects). Applying the technique to the CfA sample, they found the filaments of tens Mpc are *real.* This is the first objective, statistical evidence for the physical existence of filaments.

In the original paper of Barrow *et al.* (1985), they proposed two statistical quantitaties to quantify the structure of an MST: $F(l)$ and $R(l)$ distributions. The $F(l)$ is the distribution of edge-lengths of the MST, and $R(l)$ is the ratio of $F(l)$ to the number of pairs with the separation l in the data set. These two estimates are sensitive to the existence of high order clustering, and therefore are expected to be a good discriminant of the theories. However, quantitative analyses of available data as well as of various theoretical models(N-body simulations) still need to be done at the present.

3.4.3 Percolation analysis

Consider a system of N points in a cubic space of size l^3, its characteristic length is the mean separation $\bar{d} = l/N^{1/3}$. The *clusters* are identified by the *friends-friends* algorithm: two points are friends if their separation is less than a certain distance, say, d, and a cluster is the collection of points which are mutual friends (i.e. including the friends of friends). The percolation analysis is, in fact, used to study the geometrical properties of the clusters.

One commonly used analysis is to estimate the normalized length $l_m(b) = L_{max}(b)/l$, where $L_{max}(b)$ is the maximum length of the clusters, and b is the dimensionless separation parameter $b = d/\bar{d}$. When $l_m(b) = l_m(b_*) = 1$, the system is called to be percolated and b_* is called the percolation parameter. In a uniform distribution, b_* is 1; and in a Poissonian distribution, $b_* = 0.86$. If a sample contains large coherent structures such as filaments and sheets, the b_* is expected to be smaller than 0.86. On the contrary, if a sample contains a lot of small isolated clusters, the b_* is greater than 0.86.

There have been several studies on b_*, based on CfA and SSRS redshift surveys. The results are between 0.6 to 0.8. As shown by Dekel & West (1985) and by Barrow $ Bhavsar (1983), b_* is very sensitive to the sampling parameters(the mean density and the volume), so an interpretion of the results is not an easy task. They also showed that the parameter is not a very good discriminant between the current models.

However, this analysis could still be useful (at least in principle) if suitable quantities and suitable methods are chosen, because of the dependence of the clusters' properties on the high order clustering. One way, for example, is to estimate $l_m(b)$ for the comparative purpose, that is, to estimate $l_m(b)$ in the observations as well as in the simulations and then to compare them so as to test the models. Another example is to compare $l_m(b)$ between a real sample and its random sample, so as to exhibit the clustering on large scales(e.g., Börner & Mo 1990). Other physical properties of clusters, such as the fraction of populations in different sized clusters, may also be useful in testing the models(e.g., Pellegrini *et al.* 1990).

4

Correlation functions of galaxies in the ESO-Uppsala catalogue

4.1 Introduction

Correlation functions have been widely used to measure the clustering in galaxy distribution (§3.1–3.2). During the last 15 years, several important results have been obtained. The two-point correlation function of galaxies is found to closely obey a power law

$$\xi(r) = (r_0/r)^{\alpha} \tag{4.1}$$

with $\alpha \approx 1.8$ and $r_0 \approx 5\,h^{-1}$Mpc (Groth and Peebles, 1977, hereafter GP; Davis and Peebles, 1983). A scaling relation is found between the spatial two- and three-point correlation functions (GP, see also §3.1–3.2)

$$\zeta(r_1, r_2, r_3) = Q[\xi(r_1)\xi(r_2) + \xi(r_2)\xi(r_3) + \xi(r_3)\xi(r_1)] \tag{4.2}$$

with $Q \approx 1$. It is also found that galaxies with different morphological types have different correlation functions. In particular, Davis and Geller (1976) and Giovanelli et al. (1986), using respectively the two-dimensional magnitude-limited UGC samples (complete to $m = 14.5$) and the two-dimensional samples constructed in the Perseus-Pisces region, found that elliptical and lenticular galaxies have a two-point correlation function with larger amplitude and steeper shape. These statistical results are frequently used as important observational inputs to the theories of galaxy formation (see e.g. Efstathiou and Silk, 1983).

However, there are also questions concerning the universality of these results. First, the results are mainly derived from galaxy catalogs in the northern hemisphere, it is important to test whether or not galaxies in the southern hemisphere give the same results. Second, the previous results are mainly based on magnitude-selected samples. Since the diameter-function of galaxies (DF) is now available (Lahav et al., 1988, here after LRL), it is interesting to see whether or not the diameter-selected samples give similar results. Third, the morphological dependence found by Davis and Geller (1976) and Giovanelli et al. (1986) might apply only for galaxies in dense clusters, because their samples are dominated respectively by local superclusters and by the Perseus-Pisces supercluster. It is important to test whether or not the same dependence holds for a statistically fairer sample.

To answer these questions, we estimate the two- and three- point correlation functions for galaxies in the ESO/Uppsala (hereafter ESO) catalog (Lauberts, 1982), and analyze their dependence on the morphological type. This catalog is one of the largest catalogs in the southern hemisphere with a complete list of morphological type. It is also completely selected by a angular-diameter criterion. Furthermore, the catalog has a very similarly selected partner, the UGC catalog (Nilson, 1973), in the northern hemisphere, which enables us to compare galaxy distributions in both hemispheres.

§4.2 summarizes data and samples. In §4.3 we present the results of the two- and three-point correlation functions for various samples, without dividing galaxies according to morphological type. The morphology dependence of the correlation functions is analysed in §4.4. §4.5 contains our conclusions.

4.2 Data and samples

We form samples from the ESO catalog (Lauberts, 1982). Since we will also use the UGC catalog (Nilson, 1973), it is also summarized below. The ESO catalog covers the sky south of $\delta = -17.5°$ and the UGC catalog covers the sky north of $\delta = -2.5°$. Both catalogs are claimed to be complete to a major-blue diameter (d_1) of 1 arcmin. We form samples in the region $b^{\rm II} \leq -25°$ (ESO) and $b^{\rm II} \geq 25°$ (UGC) with different angular-diameter limits $d_{1,\rm lim}$ [$\log d_{1,\rm lim}$ changes from 0.00 to 0.65 with increment 0.05; the samples are named as follows: E00 (U00) denotes the sample with $\log d_{1,\rm lim} = 0.00$, E05 (U05) denotes that with $\log d_{1,\rm lim} = 0.05$, and so on].

The selection effects due to galactic obscuration and declination- dependence are examined. The distribution of the galaxy density as a function of declination and galactic latitude is determined and compared with that expected from a random distribution over the same sample regions. The results are presented in Fig.4.1.

For the ESO catalog, the $b^{\rm II}$-dependence is negligible in the chosen region (Fig.4.1b) and there is a tendency for the galaxy density to decrease at high (negative) values of declination (Fig.4.1a). The dependence is represented by the smooth curve drawn in the figure. A similar dependence is found for the distribution of Abell clusters in the southern hemisphere (Batuski et al., 1989). For the UGC catalog, we found a negligible δ-dependence (Fig.4.1c) but a strong density excess around the Galactic pole ($b^{\rm II} > 60°$) (Fig.4.1d). The latter is obviously not due to galactic obscuration, but due to the presence of the Coma and Virgo superclusters. So we will make no correction for the UGC samples.

A diameter function of galaxies (DF) is needed to transform the angular correlation function to the spatial correlation function. We use the DF given by LRL:

$$\phi(D)dD = \phi_\star t^{-\mu}[1 + t/\nu]^{-\nu} \left[\mu/t + (1 + t/\nu)^{-1}\right] dt, \tag{4.3}$$

where D is the metric diameter; $t \equiv (D/D_\star)^2$. For the ESO catalog $\mu = 0.25$; $\nu = 3.05$; $D_\star = 7103 {\rm kms}^{-1}{\rm arcmin}$; $\phi_\star = 0.0101(\,h^{-1}{\rm Mpc})^{-3}$. For the UGC catalog $\mu = 0.16$; $\nu = 3.78$; $D_\star = 6073 {\rm kms}^{-1}{\rm arcmin}$; $\phi_\star = 0.0139(\,h^{-1}{\rm Mpc})^{-3}$.

4.3 The two- and three-point correlation functions

4.3.1 The two-point correlation function

The two-point angular correlation function $\omega(\theta)$ is estimated by the definition (see §3.1)

$$\omega(\theta) = \frac{n_R^2}{n^2}\frac{DD(\theta)}{RR(\theta)} - 1 \tag{4.4}$$

where $DD(\theta)$ is the number of data pairs with separation in the range $\theta \pm \Delta\theta/2$; $RR(\theta)$ is the corresponding count in a set of points randomly distributed within the sample

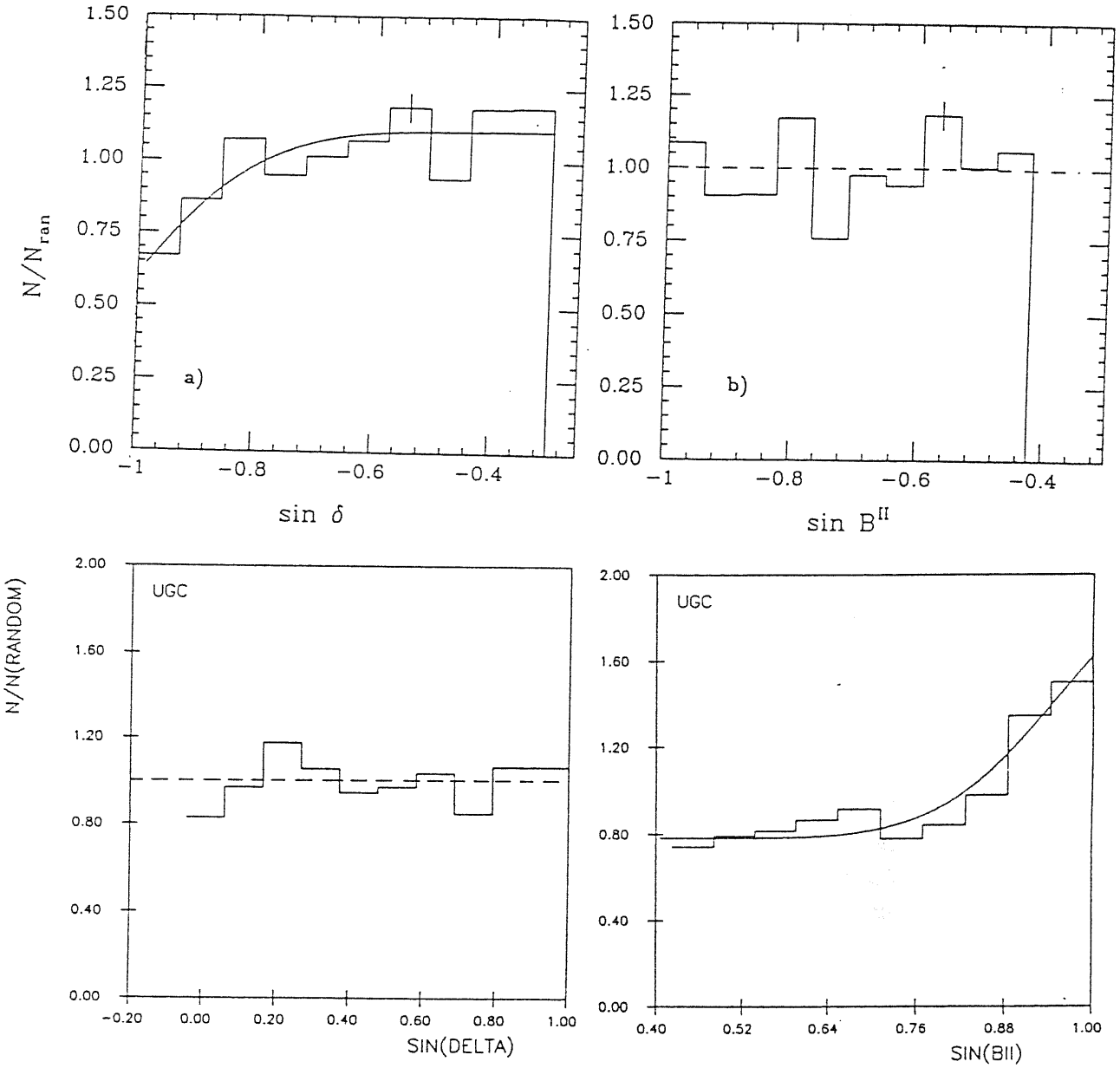

Fig.4.1 — (a) The distribution of ESO galaxies (with $d_1 \geq 1.'0$) as a function of declination (as compared with a distribution of random points within the same boundary). The smooth curve represents the selection function used in our analysis. (b) The same as (a), but as a function of galactic latitude. (c) and (d) plot the corresponding curves for the UGC galaxies

boundary; n and n_R are respectively the mean number densities of the data sample and of the random sample. For the ESO samples, the random sample is generated with the same declination dependence as is represented by the smooth curve in Fig.4.1a.

The pair counts DD and RR are estimated in 20 bins with the ith bin covering the range $0.1 \cdot (i-1) - 1 < \log\theta \leq 0.1 \cdot i - 1$ for $\log d_{1,lim} \leq 0.45$ and $0.1 \cdot (i-1) - 0.6 < \log\theta \leq 0.1 \cdot i - 0.6$ for other samples. The bootstrap resampling technique (hereafter BRT, Barrow et al., 1984) is used to estimate the error at each separation(see §3.1.5). In Fig.4.2

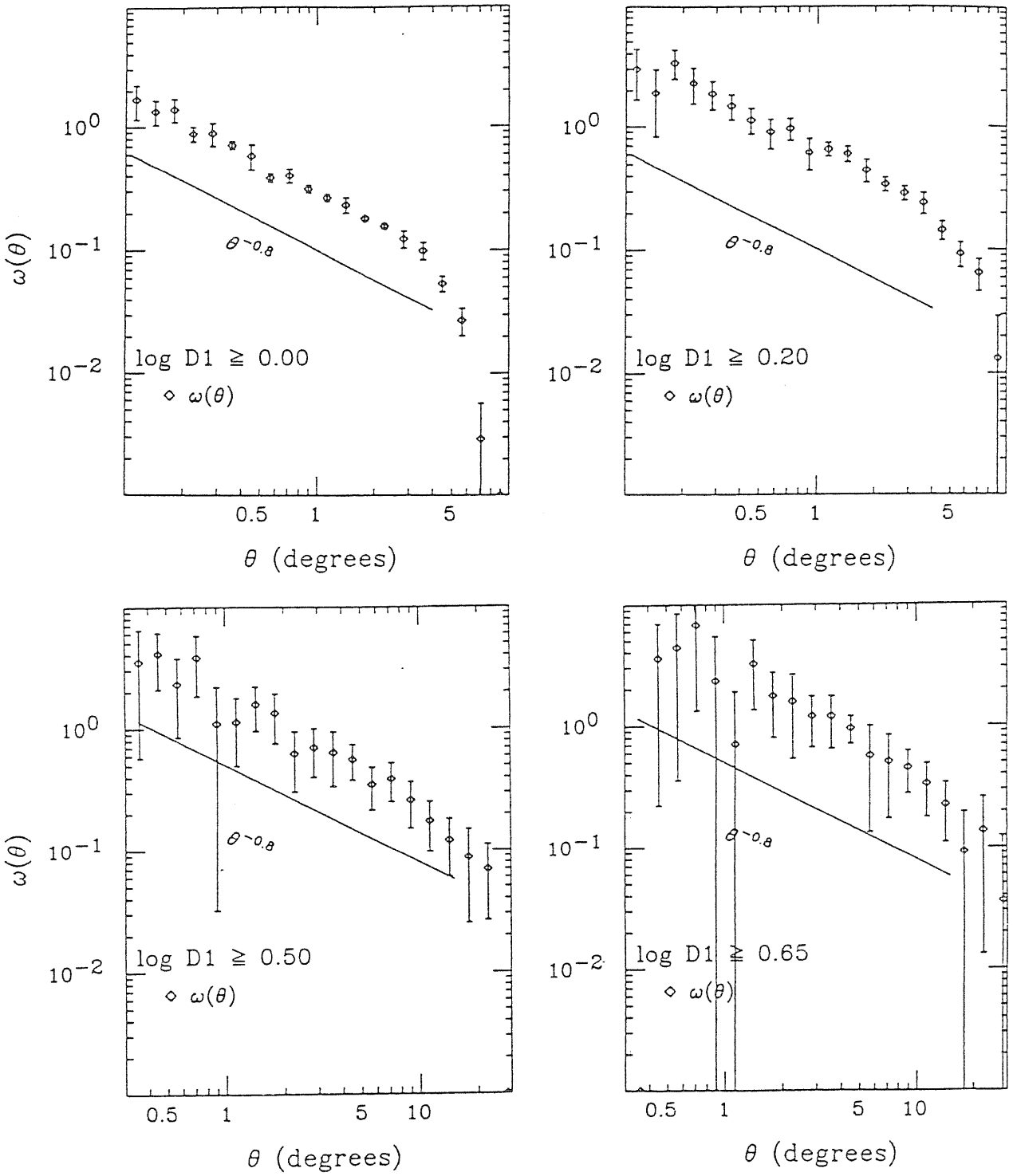

Fig.4.2 — Logarithmic plots of the two-point angular correlation functions for several typical samples (with their diameter limits indicated on the plots). The error bars represent 1σ variations among bootstrap resamplings.

we plot $\omega(\theta)$ for several typical samples formed from the ESO catalog. The plots illustrate

Table 4.1
Fit of the two-point correlation functions

sample	N_g	θ°_{min}	θ°_{max}	β	B	P	$B_{0.8}$	$P_{0.8}$	r_0
E00	5477	0.10	4.00	0.79 ± 0.03	0.29 ± 0.01	0.91	0.29 ± 0.01	0.91	4.87 ± 0.07
E05	4523	0.10	4.00	0.79 ± 0.03	0.35 ± 0.01	0.97	0.35 ± 0.01	0.96	4.84 ± 0.08
E10	3574	0.13	5.01	0.86 ± 0.05	0.41 ± 0.02	0.98	0.42 ± 0.02	0.73	4.74 ± 0.11
E15	2371	0.13	5.01	0.84 ± 0.05	0.60 ± 0.03	0.74	0.57 ± 0.03	0.53	5.01 ± 0.12
E20	1889	0.16	6.31	0.89 ± 0.05	0.68 ± 0.04	0.70	0.61 ± 0.03	0.10	4.66 ± 0.12
E25	1362	0.16	6.31	0.87 ± 0.06	0.79 ± 0.05	0.88	0.71 ± 0.04	0.59	4.52 ± 0.13
E30	1051	0.20	7.94	0.92 ± 0.08	1.00 ± 0.07	0.99	0.88 ± 0.06	0.75	4.53 ± 0.16
E35	699	0.20	7.94	0.98 ± 0.08	1.31 ± 0.11	1.00	1.05 ± 0.08	0.71	4.47 ± 0.18
E40	487	0.25	10.00	1.03 ± 0.10	1.75 ± 0.16	0.99	1.39 ± 0.12	0.62	4.65 ± 0.22
E45	386	0.25	10.00	0.91 ± 0.10	1.81 ± 0.23	0.99	1.53 ± 0.15	0.99	4.37 ± 0.23
E50	303	0.32	12.59	0.90 ± 0.13	1.92 ± 0.37	1.00	1.51 ± 0.18	1.00	3.87 ± 0.25
E55	236	0.32	12.59	0.79 ± 0.13	1.99 ± 0.43	1.00	1.73 ± 0.19	0.98	3.72 ± 0.22
E60	199	0.40	15.85	1.00 ± 0.15	2.67 ± 0.62	1.00	1.73 ± 0.22	0.99	3.31 ± 0.23
E65	143	0.40	15.85	0.99 ± 0.20	3.79 ± 1.31	1.00	2.42 ± 0.33	1.00	3.55 ± 0.26

that the data points are guided well by a power-law

$$\omega(\theta) = B\theta^{-\beta} \tag{4.5}$$

at $\omega(\theta) > 0.1$. In Table 4.1, the results of the power-law fitting (which is given by minimizing χ^2 of the fit; the corresponding minimum is denoted by χ^2_{min}) of the estimates of the two-point angular correlation functions are presented for all the samples. The tail probability, $P = P(\chi^2 > \chi^2_{min})$, that the variable χ^2 of the chi-square-distribution for the given degrees of freedom exceeds χ^2_{min} is listed to represent the goodness-of-fit. $P(\chi^2 > \chi^2_{min})$ is calculated by assuming that the data points used for the fits (which are indicated by the range of θ, i.e. θ_{min} and θ_{max}, in Table 4.1) are independent. As we can see clearly from the table, for each sample, the power-law assumption (eq.4.5) can be accepted at $\omega(\theta) > 0.1$, with the index β being about 0.8. We also try to fit the results by a single index $\beta = 0.8$ (which is approximately the weighted mean of the β values listed in Table 4.1). The results of the fit are also listed in Table 4.1 (with the amplitude B denoted by $B_{0.8}$ and the $\chi^2 > \chi^2_{min}$ probability P denoted by $P_{0.8}$). The χ^2-test shows that the universal power-law index ($\beta = 0.8$) can be accepted for all the samples. This result is remarkable, since the sample volume (given by the typical depth of the sample) varies from the shallowest ($\sim 25\,h^{-1}$Mpc) to the deepest ($\sim 120\,h^{-1}$Mpc) samples by a factor of ~ 100. The error estimated from the Poissonian variance of the pair counts is about half of that given by BRT. No universal power-law index can be accepted for all of the samples, if the Poissonian error estimate is used in the fitting.

The diameter function given by eq.(4.3) is used in Limber's equation (§3.1.3) to

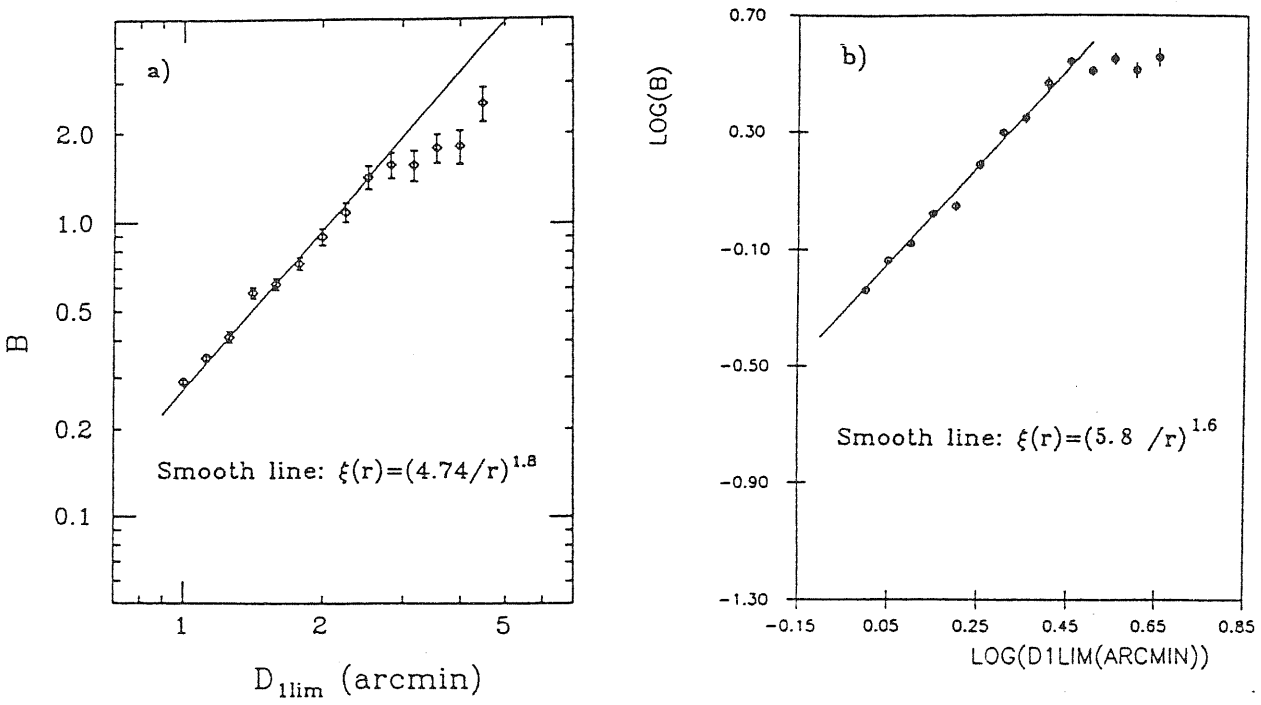

Fig.4.3 — (a) The scaling of the angular correlation strength B with sample depth (represented by the diameter limit) for ESO samples. The straight line represents the power-law form of the two-point spatial correlation function indicated in the plot. The error bars represent variations in the power-law fits of the two-point angular correlation functions for the corresponding samples. (b) The same as (a), but for UGC samples.

compute the two-point spatial correlation functions with a power-law form represented by eq.(4.1). We choose $\alpha \equiv 1 + \beta = 1.8$. The $\log B$-$\log d_{1,\rm lim}$ relation is drawn in Fig.4.3. For $\alpha = 1.8$ and a given r_0, the relation is a straight line with slope 1.8, for $B \propto (D_c^{-1} r_0)^\alpha \propto (d_{1,\rm lim} r_0)^\alpha$ where D_c is the characteristic depth of the sample. It is clear from Fig.4.3 that the data points can not be fitted (the fit in the following also refers to a weighted least chi-square) by a single value of r_0. We change r_0 to find a 'best fit' (i.e. to achieve a reasonable acceptance, e.g. $P > 5\%$, by removing the smallest number of data points), which gives $r_0 = 4.74\,h^{-1}$Mpc (the value of the variance among the used samples is about $0.20\,h^{-1}$Mpc which is compared to the largest internal error, $\approx 0.26\,h^{-1}$Mpc for the shallow samples) with $P \approx 15\%$. In this fit, we have to remove the data points for the four shallowest samples (E50, E55, E60, E65) and for the sample E15. Including E15 reduces $P(\chi^2 > \chi^2_{min})$ to $\sim 7\%$ which gives a marginally acceptable fit. The fit is not acceptable (with $P < 0.5\%$) if one or more data points of the four shallowest samples are used. We have also used other values of α. The results remain the same for all α values that can be used in a power law fit (eq.4.5) for each of the samples.

The deviations of the data points for the shallowest samples indicate a drop of the correlation function length of galaxies in the local region. For example, the correlation lengths for E60 and E65 are about $3.5\,h^{-1}$Mpc. A change of α in the acceptable range does not change the value significantly. A very similar behavior exists in the results of the similarly constructed UGC samples. Such a drop of correlation strength of galaxies in the

local region is found by many other authors (e.g. Davis et al., 1978; Einasto et al., 1986; Börner and Mo, 1990) and is interpreted as being due to a fractal structure in the galaxy distribution (e.g. Calzetti et al., 1988) or due to a density enhancement in the local region (Davis et al., 1988; Börner and Mo, 1990). Our results show that the depth dependence of the galaxy correlation length is significant only in a region with depth $< 40\,h^{-1}$Mpc, giving support to the latter interpretation.

4.3.2 The three-point correlation function

The angular three-point correlation function $z(\theta_1, \theta_2, \theta_3)$ is defined by the joint probability of finding triplets in three surface elements $d\Omega_1$, $d\Omega_2$ and $d\Omega_3$ separated by θ_1, θ_2 and θ_3 on the celestial sphere:

$$dP = N^3[1 + \omega(\theta_1) + \omega(\theta_2) + \omega(\theta_3) + z(\theta_1, \theta_2, \theta_3)]d\Omega_1 d\Omega_2 d\Omega_3 \tag{4.6}$$

where n is the mean surface number density. Without loosing generality we can set $\theta_1 \leq \theta_2 \leq \theta_3$ and define another set of variables: $\theta = \theta_1$; $u = \theta_2/\theta_1$; $v = (\theta_3 - \theta_2)/\theta_1$. Here we use the following bins of θ, u, v:

$$\begin{aligned}
\Theta_i < \theta \leq \Theta_{i+1} \qquad & [\log(\Theta_{i+1}/\Theta_i) = 0.1,\ i = 1, \cdots, i_{max},\ \Theta_1 = 0.1^\circ]; \\
U_i < u \leq U_{i+1} \qquad & [\log(U_{i+1}/U_i) = 0.1,\ i = 1, \cdots, 10,\ U_1 = 1]; \\
V_i < v \leq V_{i+1} \qquad & [V_{i+1} - V_i = 0.1,\ i = 1, \cdots, 10,\ V_1 = 0].
\end{aligned}$$

We estimate the three-point correlation function for the sample E05. Since the power-law form of $\omega(\theta)$ holds only at $\theta \leq \theta_{max} = 4.0^\circ$ for this sample, we limit our analysis to triangles with their longest sides smaller than θ_{max}. The value of i_{max} is determined by this condition. There are totally 922 bins.

Let DDD_{ijk} and RRR_{ijk} be respectively the counts of triplets in the bin $\Theta_i < \theta \leq \Theta_{i+1}$, $U_j < u \leq U_{j+1}$ and $V_k < v \leq V_{k+1}$ in the galaxy sample and in the random sample (the same random sample as in the estimate of the two-point correlation functions in §4.3.1). Integrating eq.(4.6), we have:

$$Z_{ijk} = \frac{DDD_{ijk}}{RRR_{ijk}}(\frac{n_R}{n})^3 - 1 - W_{ijk}, \tag{4.7}$$

where

$$W_{ijk} = \frac{\int_{\Theta_i}^{\Theta_{i+1}} \int_{U_j}^{U_{j+1}} \int_{V_k}^{V_{k+1}} [\omega(\theta) + \omega(u\theta) + \omega((u+v)\theta)] \frac{1}{\Delta} \theta^3 (u+v) u d\theta du dv}{\int_{\Theta_i}^{\Theta_{i+1}} \int_{U_j}^{U_{j+1}} \int_{V_k}^{V_{k+1}} \frac{1}{\Delta} \theta^3 (u+v) u d\theta du dv}; \tag{4.7a}$$

$$Z_{ijk} = \frac{\int_{\Theta_i}^{\Theta_{i+1}} \int_{U_j}^{U_{j+1}} \int_{V_k}^{V_{k+1}} z(\theta_1, \theta_2, \theta_3) \frac{1}{\Delta} \theta^3 (u+v) u d\theta du dv}{\int_{\Theta_i}^{\Theta_{i+1}} \int_{U_j}^{U_{j+1}} \int_{V_k}^{V_{k+1}} \frac{1}{\Delta} \theta^3 (u+v) u d\theta du dv}; \tag{4.7b}$$

$$\Delta = \sqrt{4u^2 - ((u+v)^2 - 1 - u^2)^2}.$$

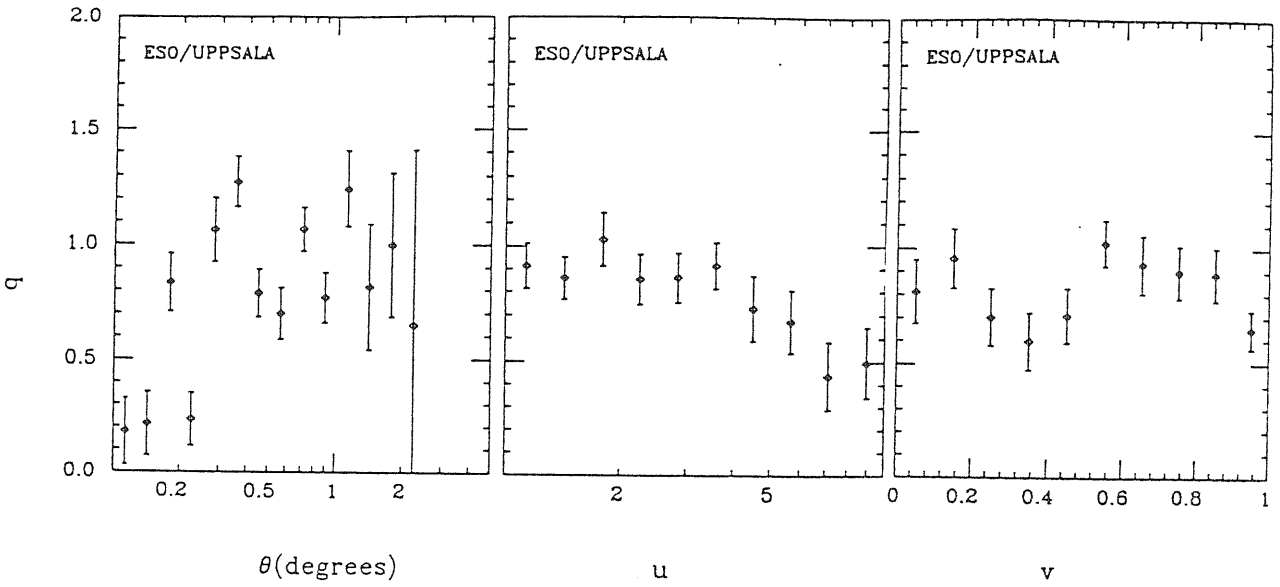

Fig.4.4 — The amplitude (q) of the three-point angular correlation function as a function of (a) the size θ, (b) the shape parameter u and (c) the shape parameter v, obtained by using all bins with triplet-count ≥ 1. The error bars are 1σ variations among bootstrap resampling.

Knowing DDD_{ijk}, RRR_{ijk} and W_{ijk}, we obtain Z_{ijk} for each bin, using eq.(4.7). The angular three-point correlation function can then be calculated from eq.(4.7b). We fit the three-point spatial correlation function by two models (Q and Q_3 are constants):

$$\zeta(r_1,r_2,r_3) = Q[\xi(r_1)\xi(r_2)+\xi(r_2)\xi(r_3)+\xi(r_3)\xi(r_1)]+Q_3\xi(r_1)\xi(r_2)\xi(r_3) \qquad (4.8a)$$

with and without the cubic term. The corresponding models in the angular function can, by assuming the power-law form of $\xi(r)$ in eq.(4.1), be written as (Tóth et al., 1989):

$$\begin{aligned} z(\theta_1,\theta_2,\theta_3) &= q[\omega(\theta_1)\omega(\theta_2)+\omega(\theta_2)\omega(\theta_3)+\omega(\theta_3)\omega(\theta_1)] \\ &\quad + q_3\frac{180}{\pi}\frac{Y(\theta_1,\theta_2,\theta_3)}{H^3(\alpha)}\omega(\theta_1)\omega(\theta_2)\omega(\theta_3). \end{aligned} \qquad (4.8b)$$

where $H(\alpha) = \int_{-\infty}^{\infty} dx(1+x^2)^{-\alpha/2}$; $Y(\theta_1,\theta_2,\theta_3) = \frac{1}{\theta_3}\int_{-\infty}^{\infty} dx[x^2+1]^{-\alpha/2}\int_{-\infty}^{\infty} dy[y^2+1]^{-\alpha/2}[(\frac{\theta_1}{\theta_3}x-\frac{\theta_2}{\theta_3}y)^2+1]^{-\alpha/2}$; q/Q and q_3/Q_3 only depend on the DF and α(For the formulas, see Tóth et al., 1989). Actually we use the weighted least-chi-square to fit equation (4.7b) by expression (4.8b) to obtain q and q_3. The goodness-of-fit is represented by $P(\chi^2 > \chi^2_{min})$. The error in our fitting comes from two kinds of independent statistical uncertainties: that from DDD_{ijk} which is estimated by BRT and that from W_{ijk} which is given by the uncertainty in $\omega(\theta)$. We neglect the error from RRR_{ijk}, since we have constructed a large random sample (6,000 points) and used an interpolation formula for RRR_{ijk}.

For sample E05, there are 894 bins with counts ≥ 1. We only use these bins in our fitting, because BRT error of DDD_{ijk} in empty bins is zero. Had these small number (28)

of empty bins been used, they would have overwhelming weight in χ^2- fitting and lead to incorrect results. In order to check sensitivity to the exclusion of these bins, we also fit the result by using bins with counts $\geq m (m = 2, \cdots, 20)$. All these bin choices give similar results, implying that excluding these empty bins does not influence our conclusions. The χ^2-test shows that the two models can all be accepted (with $P(\chi^2) \approx 1$) for all of the bin choices. This means that the cubic term is not important within the error of the results. The fitting without the cubic term gives a value of q in the range 0.79-0.92 for different bin choices, with $\bar{q} \approx 0.90$, $\sigma_q = 0.03$ (the internal error is about 0.04) and $q_3 < 0.16$. For illustration, we plot q with respect to θ, u, v for the fit with 894 bins in Fig.4.4.

Using the DF given in eq.(4.3), we can find the conversion factors (see Tóth et al., 1989) $q/Q \approx 1.37$, $q_3/Q_3 \approx 8.09$. We then obtain $Q = 0.66 \pm 0.03$ and $|Q_3| < 0.02$. The value of Q obtained here is smaller than that given by GP. GP gave $Q = 1.29 \pm 0.21$. This discrepancy could be due to the fact that galaxy distribution in the southern hemisphere contains less prominent clusters than in the northern hemisphere. The result is in agreement with those given by Peebles (1981) ($Q = 0.68 \pm 0.05$) for the Rood sample and by Efstathiou and Jedrzejewski (1984) ($Q = 0.8 \pm 0.1$; see also Bean et al., 1983) for the CfA, AAT, KOS and KOSS redshift samples, all of which contain no prominent clusters.

We have carried out a similar analysis for sample U05, without removing the apparent galaxy concentration around the north pole of the Galaxy. We found $\bar{q} = 1.78 \pm 0.02$. Using the DF for UGC catalog (LRL), we obtained $q/Q \approx 1.32$; $q_3/Q_3 \approx 5.84$, which leads to $Q = 1.35 \pm 0.02$, $|Q_3| < 0.02$.

It should be pointed out that, if we use error estimate given by a Poissonian distribution rather than by BRT, the result can not be fitted by the two models represented by eq.(4.8) with reasonable degree of acceptance.

4.3.3 Discussion

It is interesting to compare our results with those obtained for other catalogs. The index of the two-point correlation function ($\beta = 0.8$) found here is in agreement with that found for many (northern) sky samples (see §3.2). The correlation length $r_0 = 4.74 \pm 0.20\, h^{-1}$Mpc is also in good agreement with the result ($r_0 = 4.7\, h^{-1}$Mpc) obtained in GP for the Lick catalog. The agreement is remarkable, considering that the Lick catalog is differently selected (magnitude selected), much deeper (about two times as deep) and covers a different sky region ($\delta > -23°$) than the ESO catalog. Our results show that samples selected by diameter give practically the same results for the two-point correlation function of galaxies. The results also demonstrate that $\omega(\theta)$ obeys a scaling relation represented by $\alpha \approx 1.8$ and $r_0 \approx 4.7\, h^{-1}$Mpc for all samples deeper than $\sim 40\, h^{-1}$Mpc.

Very recently Maddox et al. (1990) have reported their results of the two-point correlation functions for samples constructed from the APM galaxy survey. They found a larger correlation length than that obtained here. A possible explanation could be that our correction for the declination dependence might erase some real clustering. If we calculate the two-point correlation function without correcting for the dependence, the correlation length becomes larger and the correlation index becomes smaller. It is unclear whether this declination dependence is due to clustering or it is due to a selection effect. For the UGC catalog, a strong excess of galaxy density was found only at $b^{\rm II} \geq 60°$. It is rea-

sonable to assume that this dependence is due to galaxy clustering (around the galactic north pole) rather than galactic obscuration. In this case, we found a larger value of r_0 ($= 5.8 \pm 0.3\, h^{-1}$Mpc) and a smaller value of α ($= 1.6 \pm 0.1$).

The correlation length r_0 drops to $\sim 3.5\, h^{-1}$Mpc for the shallow samples (with depth $< 30\, h^{-1}$Mpc). This agrees with the result, $r_0 \approx 3.6\, h^{-1}$Mpc, for the bright galaxies (at $m \leq 13$) in the southern hemisphere (Davis et al., 1978). The analysis for UGC samples gives a very similar result. Our results demonstrate clearly that the depth-dependence is produced by the local region with a depth $\leq 40\, h^{-1}$Mpc.

The three-point correlation function has been demonstrated to obey the scaling relation given by eq.(4.2) for galaxies (e.g. GP, Sharp et al., 1984) and for clusters of galaxies (Jing and Zhang, 1989; Tóth et al., 1989). It is found that $Q \approx 1$. Our results show that galaxies in the ESO catalog also obey such a scaling relation, but with a smaller value of Q ($Q = 0.66 \pm 0.03$). This value is much smaller than that found by GP for the Lick catalog ($Q = 1.29 \pm 0.21$) and that obtained for the UGC catalog ($Q = 1.35$) by us. As pointed out by Peebles (1980), the existence of prominent clusters could enhance the value of Q. The low Q value we find for the ESO catalog could be due to the fact that the southern hemisphere contains less prominent clusters than northern hemisphere. It is interesting to note that redshift samples containing no prominent clusters also gave similar values: $Q \approx 0.7$(Peebles, 1981; Efstathiou and Jedrzejewski, 1984).

The error estimates used for different quantities could be quite formal. The error at each bin in the two- and three- point correlation functions is estimated by BRT. The error is used only to weigh each point in the fitting. The errors quoted for the results (ΔB, $\Delta\beta$ for the two-point function; Δq, Δq_3 for the three-point function) for each sample are internal in the sense that they are estimated from the variance of the fit. The external errors based on the scatter of results among independent samples are larger. The universal scaling of $\omega(\theta)$ with depth can be accepted with higher confidence than that given by the χ^2 test. For the correlation length r_0, the standard deviation derived from the scatter of the results among the ten samples with $\log d_{1,\rm lim} < 0.5$ is about $0.2\, h^{-1}$Mpc which is comparable to the deviation ($0.26\, h^{-1}$Mpc) quoted by Peebles (1979) among galaxies of different fields. The deviation could be underestimated because the samples with different diameter limits are not completely independent. The error on Q quoted in our discussion represents only the internal error. The deviation among independent samples can be much larger (GP found $\Delta Q = 0.21$). A similar result might be obtained if we use the scattering among the results of different realizations of the bootstrap resampling.

4.4 Dependence on morphological type

The dependence of the two- and three- point correlation functions is analysed by using samples E05. The diameter limit ($\log_{10} d1 \geq 0.05$) is chosen for the sake of completeness. The sample is further divided into E (elliptical, lenticular and compact), S (Sa, Sab, Sb), and L (Sbc and later types) samples according to morphological types (see Table 4.2). The correction for the selection effects is made, and the two- and three-point correlation functions are estimated in the same way as in the last section.

4.4.1. The two-point correlation function

The two-point angular correlation function $\omega(\theta)$ is estimated by using eq.(4.4). The

Table 4.2
Samples and their two-point correlation function

Sample	Morphology	N_g	θ°_{min}	θ°_{max}	$\beta \pm \Delta\beta$	$B \pm \Delta B$	$P(\chi^2)$	r_0
ESO-E	E-E0-S0a-Comp	861	0.1	4.0	0.96 ± 0.09	1.03 ± 0.10	1.00	8.35
ESO-S	Sa-Sab-Sb	1348	0.1	4.0	0.81 ± 0.09	0.49 ± 0.05	0.95	5.84
ESO-L	Sbc and Later	1719	0.13	4.0	0.83 ± 0.14	0.28 ± 0.03	1.00	4.29

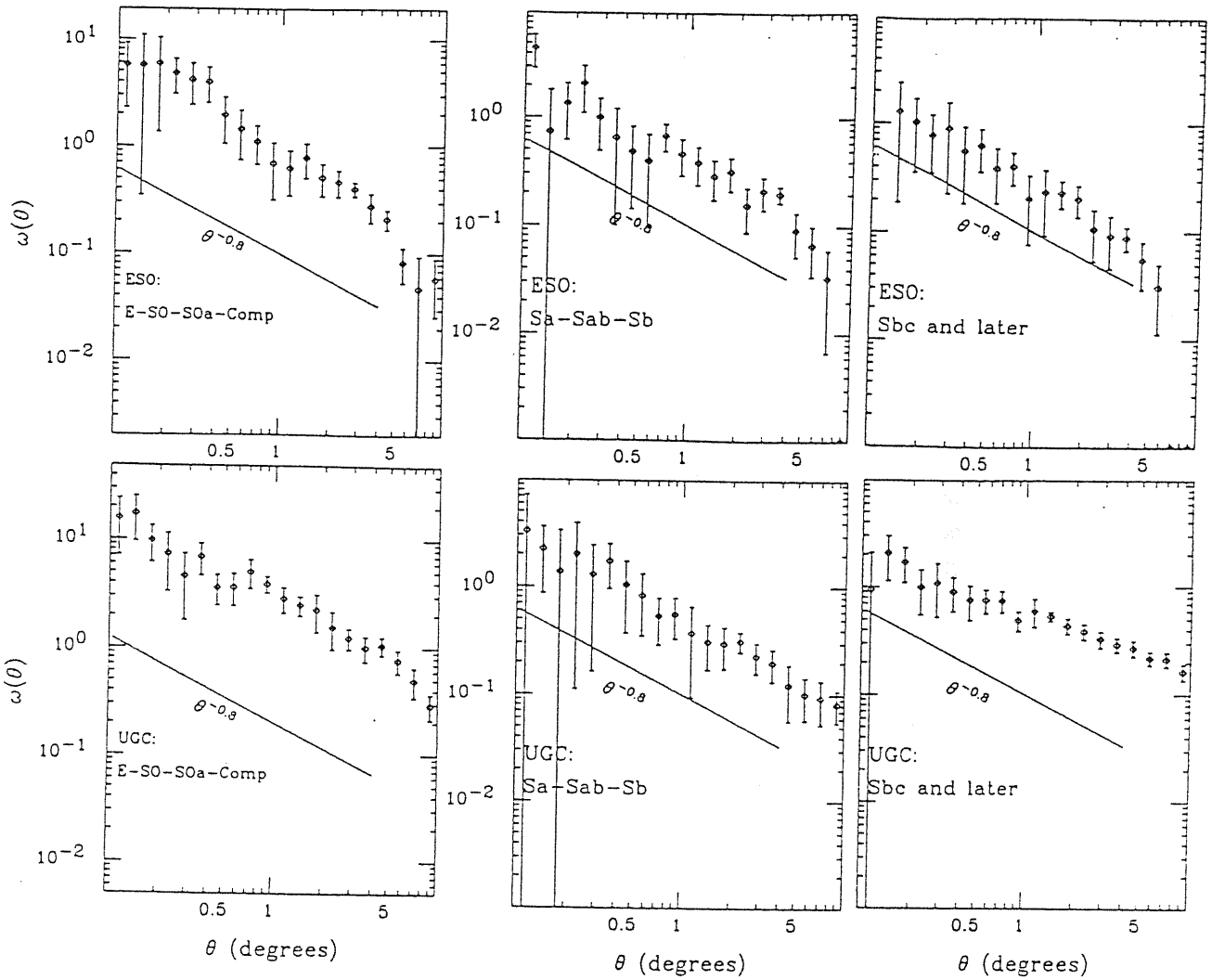

Fig.4.5 — Logarithmic plots of the two-point angular correlation functions for the morphology samples (with their morphological types indicated on the plots). The error bars represent 1σ variations among bootstrap resamplings.

pair counts DD and RR are estimated in 20 bins with the ith bin covering the range $0.1 \cdot (i-1) - 1 < \log\theta \leq 0.1 \cdot i - 1$ for each sample.

In Fig.4.5 we plot $\omega(\theta)$ for different morphological samples. The results clearly show that $\omega(\theta)$ of each sample can be fit by the power-law form (eq.4.5) at $\omega(\theta) \geq 0.1$. In Table 4.2 we present the results of the power-law fitting for $\omega(\theta)$ by using the weighted least χ^2-techniques. The power law form (eq.4.5) is acceptable for each sample. The early type galaxies have a slightly steeper slope than the other two types; the slopes of the S and L samples are comparable. Since $\alpha = \beta + 1$ without depending on the form of the diameter function, the dependence of the slope on the morphological type found here is much weaker than that found by Davis and Geller (1976, they found $\beta = 1.10 \pm 0.09$; 0.71 ± 0.05; 0.69 ± 0.06 for ellipticals, lenticulars and spirals, respectively) and Giovanelli et al (1986, they found $\beta = 0.90 \pm 0.06$, 0.65 ± 0.07 and 0.37 ± 0.04 for the E, S and L types respectively). For the corresponding UGC samples (constructed from U05), we also found a weak morphology dependence: the slopes for the E, S and L samples are respectively 0.82 ± 0.06, 0.87 ± 0.12 and 0.54 ± 0.05.

Since there is no statistical results of the DFs for different morphological types, we assume that different morphological types obey the same form of the diameter function (eq.4.3). We should remember that the correlation length r_0 is sensitive to the form of the diameter function. From the Limber equation (Peebles, 1980), we get the two- point spatial function $\xi(r) = (r_0/r)^{\beta+1}$, where r_0 is also listed in Table 4.2 for each sample. We see that the early type galaxies have a correlation strength about two times that of the S types and about four times that of the L types. The result is the same as that found by Davis and Geller (1976) and Giovanelli et al. (1986) for two-dimensional samples and by Börner et al. (1989) for redshift samples, indicating that the assumption of a universal diameter function for different types is reasonable for our purpose. The effective depth of the ESO catalog is about 70 h^{-1}Mpc. We see that the morphology dependence can exist on scales at least to $D_{eff}\theta_{max} \approx 5\,h^{-1}$Mpc.

4.4.2 The three-point correlation function

The three-point angular function for each morphology sample is calculated by using the following bins of θ, u, v:

$$\Theta_i < \theta \leq \Theta_{i+1} \qquad [\log(\Theta_{i+1}/\Theta_i) = 0.2,\, i = 1, \cdots, i_{max},\, \Theta_1 = 0.1^\circ];$$
$$U_i < u \leq U_{i+1} \qquad [\log(U_{i+1}/U_i) = 0.2,\, i = 1, \cdots, 5,\, U_1 = 1];$$
$$V_i < v \leq V_{i+1} \qquad [V_{i+1} - V_i = 0.2,\, i = 1, \cdots, 5,\, V_1 = 0].$$

We also limit our analysis to triangles with their longest sides less than $\theta_{max} \approx 4.0^\circ$. There are totally 99 bins.

The results of the three-point functions for different morphological samples are presented in Table 4.3. The fitting is done in the same way as in §4.3.2. The upper limits of Q_3 for all of the bin choices are much smaller than Q (Table 4.3) for all the samples. Adding the cubic term reduces χ^2_{min} very little. So the cubic term is not important for galaxies of different morphological types, within the error of the statistics. The results of fitting without Q_3 for different bin choices are presented in Fig.4.6. We can easily see that, the E- and L- type samples have the same Q values within the statistical uncertainty; the mean value is about 0.6, which is in good agreement with the result for *all* galaxies without morphology division. However for the S sample, the Q value is much smaller and no

Table 4.3
The three-point correlation functions

Sample	N_b	Q_3(upper limit)	Q(hierarchical)
ESO-E	92	0.03	0.55 ± 0.12
ESO-S	92	0.02	0.03 ± 0.12
ESO-L	90	0.05	0.48 ± 0.20
UGC-E	92	-0.05	1.08 ± 0.10
UGC-S	77	0.05	0.66 ± 0.20
UGC-L	93	-0.20	1.25 ± 0.10

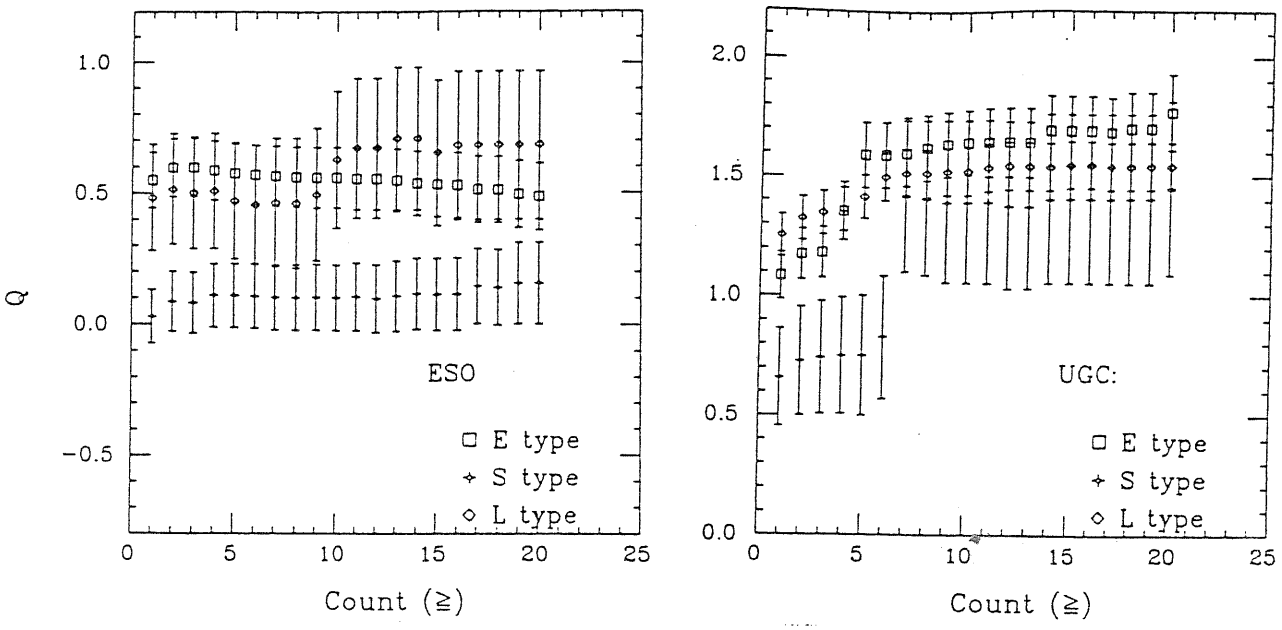

Fig.4.6 — The amplitudes (Q) of the three-point spatial correlation function for different bin choices (The morphological types are indicated on the figure). (a) for the ESO samples; (b) for the UGC samples. The error bars are 1σ variations among bootstrap resamplings.

meaningful signals are detected. A similar behaviour is seen in the results for the sample U05. In this case, the E and L types give a similar value $Q \approx 1.3$ which is in agreement with that found for the total sample; the S sample gives a much smaller value $Q \approx 0.7$. But the fits for bins with counts ≥ 7 give a similar Q value as the E and L samples.

4.4.3 Discussion

Since the slope of the two-point spatial correlation function is related to that of the angular function without depending on the form of the diameter function, our results suggest that the slopes of the two-point correlation functions for different morphological types are similar for a statistically fairer sample. The morphology dependence of the slope found before might be mainly due to galaxies in prominent clusters. The samples used by

Davis and Geller (1976) and Giovanelli et al. (1986) are dominated respectively by the local superclusters and by the Perseus-Pisces supercluster. The fact that the northern sky contains several prominent clusters (Virgo, Coma and Perseus-Pisces) could account for some difference we found between the northern and the southern samples. It is interesting to note that the three dimensional analysis of CfA survey (Börner and Mo, 1990) also gave a weak indication of morphology dependence.

If our assumption of a universal DF for different morphologies is not seriously in error, our results indicate that the clustering strength increases from late- to early- types. The trend is in good agreement with that given by previous studies for 2-D samples (Davis and Geller, 1976; Giovanelli, et al.,1986) and for 3-D samples(Börner and Mo, 1990). A more quantitative comparison between different morphological types needs more accurate knowledge of the DF. We should keep in mind that the uncertainty in DF can easily lead to a difference of a factor of 2 in the amplitude of ξ (Peebles, 1980).

The results are interesting for the theories of galaxy formation. If the morphological segregation of galaxies is due to the fact that the galaxies of different types are formed on different peaks in a density field, as is predicted by the 'natural scheme' of the biased galaxy formation, galaxies with different types should have different two-point correlation strengths but approximately the same slope (Kaiser, 1984; Bardeen et al. 1986). Environmental effects after galaxy formation can change such a relation in dense clusters (Whitmore, 1989). The weak morphology dependence of the correlation slope for samples containing no prominent clusters may be due to biassing.

Previous studies have shown that the three-point correlation functions for galaxies (e.g. GP; Sharp et al. 1984) and clusters of galaxies (e.g. Jing and Zhang, 1989; Toth et al. 1989) all obey the same hierarchical form with $Q \approx 1$. Using the void-probability function, Mo and Börner (1990) showed that the clustering of galaxies of different morphological types obey a similar hierarchical model. The results obtained here show that the three-point correlation functions for galaxies of different types also obey the hierarchical form (eq.4.2). But the Q value for the ESO S sample is much smaller than those for the E and L samples. Such a difference could not be due to the difference in the DFs of different morphologies, since q/Q is insensitive to DFs. So it would be worthwhile to investigate such a difference by using a much larger sample.

4.5. Conclusions

In this paper, we analysed the angular two- and three- point correlation functions and their dependence on morphological types, using the diameter-limited samples constructed from the ESO-Uppsala catalog. We used the diameter function given by Lahav et al. (1988) to obtain the spatial functions. It is found that:

(1) The two-point correlation functions for samples deeper than $\sim 40\,h^{-1}$Mpc can all be fitted by the power law $\xi(r) = (r_0/r)^\alpha$ with $\alpha = 1.8$, $r_0 = 4.74 \pm 0.20\,h^{-1}$Mpc. The result is in good agreement with that obtained for the magnitude-limited samples in the northern hemisphere, demonstrating that the diameter-limited samples can also be used to determine the two-point correlation, that the scalings for the two-point correlation function hold for galaxies in the southern sky.

(2) The correlation length r_0 drops to about $3.5\,h^{-1}$Mpc for samples shallower than

$40\,h^{-1}$Mpc. The result shows clearly that the depth-dependence of the two-point correlation function is produced by the local density enhancement with a depth smaller than $40\,h^{-1}$Mpc.

(3) The early-type (elliptical, lenticular and compact) galaxies have a correlation strength about 2 times that for the early spirals (Sa, Sab, Sb) and about 4 times that for the late types (Sbc and later types). The result is in agreement with that for magnitude-limited samples.

(4) The slope of the two-point correlation function does not depend strongly on morphological type. Our results suggest that the strong morphology dependence found before is mainly due to galaxies in some dominating clusters and that the morphological segregation outside clusters can be due to biassing.

(5) The three-point correlation function for the ESO samples obey the hierarchical relation. The Q value is much smaller than that for the northern samples and in agreement with that for redshift samples containing no dominating clusters. The early spirals (Sa, Sab, Sb) give significantly smaller Q values than the other types. Whether the difference is real or it is due to that the early spirals have a different diameter function is not known.

‡The materials presented in this chapter are based on our paper: Jing, Y.P., Mo, H.J. & Börner, G. 1991, *Astronomy and Astrophysics*, (in press)

5

Is the spatial cluster-cluster correlation function enhanced significantly by contaminations ?

5.1 Introduction

In the past few years, both the angular and spatial cluster-cluster correlation functions have been studied in great detail (Hauser & Peebles 1973; Bahcall & Soneira 1983, hereafter BS83; Klypin & Kopylov 1983; Postman, Geller & Huchra 1986; Bahcall 1988; see §3.2). Their results have consistently shown that Abell clusters (Abell 1958) of richness class $R \geq 1$ have positive correlations out to $70 \sim 100\ h^{-1}$ Mpc. The rich cluster-cluster correlation function, ξ_{cc}, is well represented by a power-law, $\xi_{cc} = (r_\circ/r)^\gamma$, with $\gamma \cong 1.8$ and $r_\circ \cong 25\ h^{-1}$ Mpc. Such a large correlation amplitude and coherence length strongly challenge the traditional galaxy formation theories which assume a Gaussian spectrum of the primordial density perturbations in an $\Omega = 1$ Universe. In particular, the standard biassed CDM model fails to reproduce the observed ξ_{cc} although it is consistent with many other features of galaxy clustering and with the microwave background radiation anisotropies (Davis *et al.* 1985, White *et al.* 1987; Frenk *et al.* 1988).

Since the Abell clusters were selected by eye as surface galaxy-density peaks, some fraction of the clusters could result from the superposition of foreground and/or background galaxies or galaxy groups. If the 'artificial' clusters are the products of such chance superpositions then they would introduce a random component in the cluster catalogue, leaving ξ_{cc} mostly unaffected. If, however, the superposition effect is, as expected (Lucey 1983), correlated with the position of rich clusters (*i.e.*, the high galaxy density around rich Abell clusters tends to increase the mean galaxy density around them and therefore nearby, in angular space, clusters could be revealed that otherwise would not have fulfilled the Abell selection criteria) then the 'artificial' clusters could spuriously enhance the spatial clustering of clusters, which would be manifested especially along the line-of-sight. In this work we are interested in this later type of cluster contamination which presently is in debate whether it can seriously enhance the amplitude of the cluster-cluster correlation function. Several tests like the scaling dependence of ξ_{cc}, the cross-correlation of different distance-class cluster samples and the *finger-of-God* effect (*e.g.*, Bahcall 1988; Szalay, Hollósi & Tóth 1989; Huchra *et al.* 1990) show that contaminations have probably little effect on the estimation of ξ_{cc}. Furthermore, X-ray selected clusters and cD clusters, which should be less affected by contaminations, show as strong correlation functions as those of BS83 (Lahav *et al.* 1989; West & Van den Bergh 1991).

Two approaches have been used in an attempt to model the contamination effects and to correct the original ξ_{cc} and both have shown that ξ_{cc} could be seriously enhanced by such effects.

The first approach has been to correct the original galaxy count of each Abell cluster due to contaminations from neighbouring clusters, according to a model of the spatial and luminosity distribution of galaxies in clusters (Dekel *et al.* 1989; Olivier *et al.* 1990).

These authors construct the galaxy distribution around each cluster centre using the observed cluster-galaxy cross-correlation function (Seldner & Peebles 1977; Lilje & Efstathiou 1988) while assuming spherical cluster halos and using the field galaxy luminosity function (Efstathiou, Ellis & Peterson 1988). Finally, after the above procedure has been applied and 'double' counted galaxies are eliminated, the clusters which have a corrected galaxy count < 50 are excluded from the catalogue. This results in a 10% to 15% decrease of the number of Abell clusters and a significantly weaker 2-point cluster correlation function. However, neither clusters are spherical [in fact they are highly flattened (Binggeli 1982; Plionis, Barrow & Frenk 1991)] and therefore the total projected area covered by each cluster is probably smaller than what expected in the spherical cluster model, nor do galaxies in clusters seem to follow a universal luminosity function (see discussion in Binggeli, Sandage & Tammann 1988). Furthermore, the high percentage of contamination found by the above model is in disagreement with a recent estimate of only a $\sim 3\%$ contamination based on redshift surveys of individual cluster regions (Struble and Rood 1991b). Note that such a small cluster contamination should have negligible effect on the statistics of ξ_{cc} (as compared with those of Olivier *et al.*).

The second approach (Sutherland 1988, hereafter S88 and Sutherland and Efstathiou 1991, hereafter SE91) has been to calculate the redshift correlation function within some fixed angle separation, $\xi_\theta(\Delta z)$, or within some projected separation, $\xi_{r_p}(R_z)$. These authors found that there is a significant excess of cluster pairs relative to random samples, *i.e.* a large positive $\xi_\theta(\Delta z)$ and/or $\xi_{r_p}(R_z)$ at large redshift separations ($\Delta z > 0.02$), and they attributed this effect to significant cluster contamination. Their method, can only indirectly test the superposition/contamination effect but is, however, independent of the contamination model details and so it could be a useful measure of the effect.

The potential importance of the results of Sutherland and Efstathiou prompted us to carefully check their reality. As well known, there are abundant large supercluster chains and voids in the spatial distribution of Abell clusters (*e.g.* Bahcall and Soneira 1984; Batuski & Burns 1985a,b; Tully 1987). Since the numbers of clusters involved in these studies are small, strong clustering of small number of clusters could produce certain specific patterns of superclustering and the resulting redshift correlation functions could be nonzero even on large redshift separations. In §2 we point out that the manifestation of real clustering and of the effects of contamination is rather different and we propose a *consistency* check between different cluster samples as means of discriminating between these two distinctive effects. Three observational data sets are used in our analysis, which are the redshift complete samples of Abell clusters used in S88 and SE91. Our results do not support the contaminations origin of the Sutherland effect but rather, they support real clustering as the origin of this effect.

To substantiate this indication we produced a set of simulated clusters, selected as peaks of a density field, the power spectrum of which is so chosen that the peaks have the same two-point correlation function as the Abell clusters (details in §3). The simulated catalogues are constructed in the same sky area and with the same selection functions as those of the real samples and they are analysed in an attempt to investigate *at what frequency can we observe the Sutherland effect in the simulated data which by construction have no contamination effects.*

5.2 Samples, redshift selection functions and analysis

5.2.1 Samples and definitions

Our first sample (hereafter DR41) includes all 100 clusters in the Abell catalogue with distance class $D \leq 4$, galactic latitudes $|b^{II}| \geq 30°$, richness $R \geq 1$ and redshift $z < 0.12$. This redshift limit is imposed in order to properly compare data and simulations (§5.3) since the simulation volume is a 640 h^{-1} Mpc $\times$640 h^{-1} Mpc $\times$640 h^{-1} Mpc box. Neglecting the 3 clusters with $z > 0.12$ is certainly unimportant to our analysis. Relaxing the richness constraint to include $R = 0$ clusters with measured redshifts $z \leq 0.12$, we obtain our second sample (hereafter DR40) which contains 210 clusters. The third sample (hereafter 'Deep') is from the complete deep survey of Huchra *et. al.* (1990), which contains 132 Abell clusters in the region $58° \leq \delta \leq 78°$ and $10^h \leq \alpha \leq 15^h$ with $z \leq 0.24$. All cluster redshifts used are from the updated compilation of Struble and Rood (1991a) and Huchra *et. al.* (1990). Comoving distances to clusters are estimated from redshifts using the standard relation (Mattig 1958):

$$R = \frac{c}{H_\circ q_\circ^2(1+z)}\left[q_\circ z + (1-q_\circ)(1-\sqrt{2q_\circ z+1})\right] \tag{5.1}$$

with $H_\circ = 100\ h$ km sec^{-1} Mpc^{-1} and $q_\circ = 0.5$ (as used by BS83). We now define the redshift correlation function within a fixed angular or projected spatial separation range:

$$\xi_{\mathcal{A}}(\mu) = \frac{N_{\mathcal{A}}^{cc}}{\langle N_{\mathcal{A}}^{rr}\rangle} - 1 \tag{5.2}$$

where $(\mathcal{A},\mu) = (\theta,\Delta z)$ for the angular separation case and $(\mathcal{A},\mu) = (r_p, R_z)$ for the projected spatial separation case. These correlation functions measure the excess, over random, number of clusters with redshift separation Δz (or R_z) at a certain angular or projected spatial separation range, $\mathcal{A}_1 \leq \mathcal{A} \leq \mathcal{A}_2$. $N_{\mathcal{A}}^{cc}$ is the number of sample cluster pairs and $\langle N_{\mathcal{A}}^{rr}\rangle$ is the expected number of random pairs at the same angular or projected separation range. The random catalogues are, of course, constructed using the same boundaries and selection functions as the real data. In all of the following analysis we adopt the BS83 galactic selection function:

$$P(\mid b \mid) = \text{dex}\ [0.3(1 - \text{cosec} \mid b \mid)] \tag{5.3}$$

5.2.2 Dependence of $\xi_{\mathcal{A}}(\mu)$ on the redshift selection function

If one carefully examines the excess number of DR41 cluster pairs, $\Delta F_\theta(\Delta z)$, given by BS83 (their Figure 8) and $\xi_\theta(\Delta z)$ given by S88 (his Figure 2), she/he can easily find some discrepancies. For the angular separation $10° \leq \theta \leq 25°$ and redshift separation $\Delta z = 0.055 \sim 0.06$, $\Delta F_\theta(\Delta z)$ is negative while $\xi_\theta(\Delta z)$ is positive. Furthermore $\xi_\theta(\Delta z)$ remains almost at a constant value of ~ 0.3 in several redshift bins around $\Delta z = 0.05$, while there are large fluctuations in $\Delta F_\theta(\Delta z)$. These differences cannot be explained even by normalizing $\Delta F_\theta(\Delta z)$ by random pairs to obtain $\xi_\theta(\Delta z)$. Such discrepancies, however, could arise from different choices of the redshift selection function (RSF) used to construct the random samples.

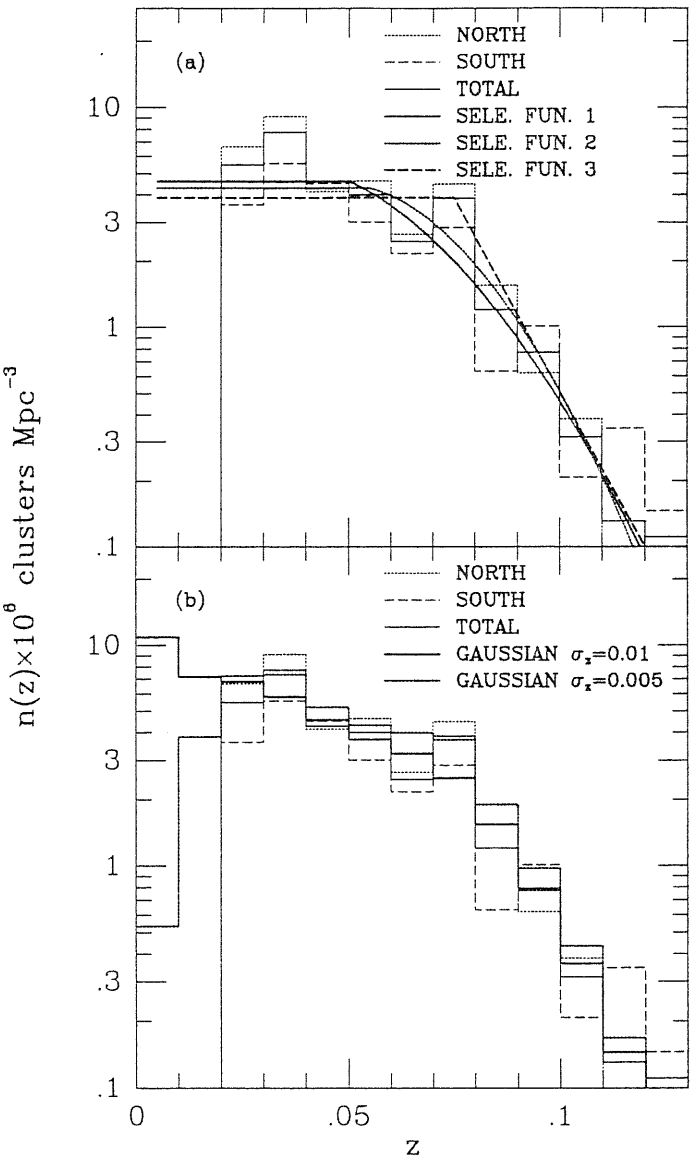

Figure 5.1

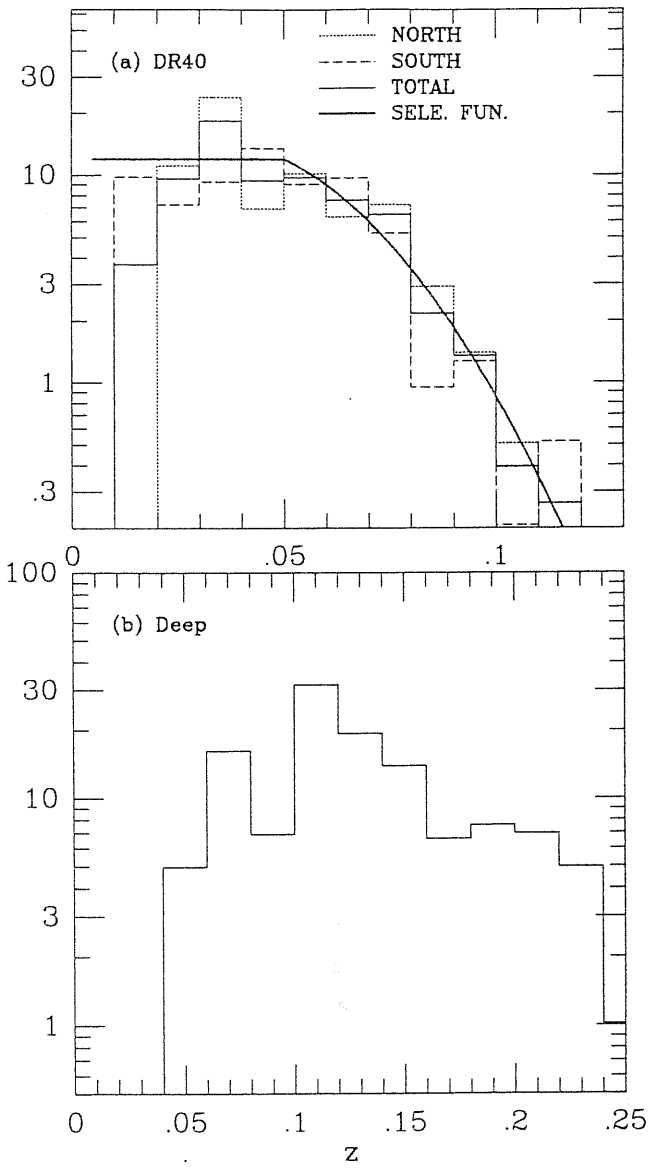

Figure 5.3

Fig.5.1 — The spatial density distribution of DR41 clusters as a function of redshift, plotted respectively for the north and south Galactic hemispheres as well as for the whole sky (details in the text). (*a*) The three smooth redshift selection functions; (*b*) The two selection functions based on a Gaussian convolution of the observed cluster redshifts with a dispersion σ_z (indicated in the plot).

Fig.5.3 — The spatial density distributions of: (*a*) DR40 cluster sample (together with the RSF); (*b*) 'Deep' cluster sample.

We choose the $\xi_\theta(\Delta z)$ measure and the DR41 sample to illustrate the sensitivity of

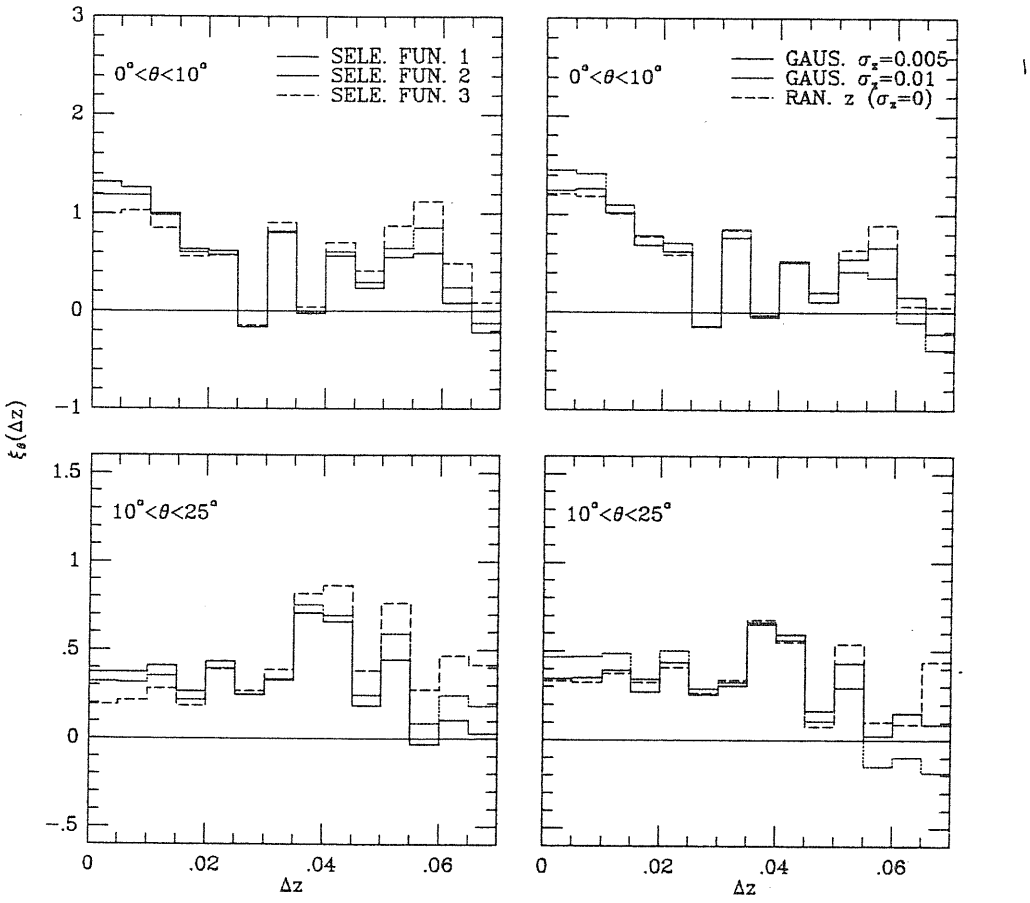

Fig.5.2 — The DR41 redshift correlation functions $\xi_\theta(\Delta z)$ estimated from the six different selection functions, shown in Fig.5.1.

the redshift correlation analysis to the choice of the RSF. Since the spatial distribution of clusters is rather clumpy and we have no *a priori* knowledge of the intrinsic RSF, we use six different RSF models. In Figure 5.1 we plot the DR41 cluster density distribution and the different RSF models. The first three RSFs are smooth fits to the density distribution, giving different weight to the peak at $z = 0.075$. The other three RSFs are given by random assignments of the observed redshifts perturbed with a Gaussian dispersion in z of $\sigma_z = 0.0$, 0.005 and 0.01 (if $\sigma_z = 0$ then the RSF is identical to the sample density distribution). The RSFs with $\sigma_z = 0.005$ and 0.01, shown in Figure 5.1b, are estimated by constructing 1000 random samples. Since the peak around $z \approx 0.075$ is the result of strong clustering of several superclusters (Bahcall and Soneira 1984), we think that the solid line in Fig.5.1(a) probably represents better the sample redshift selection effects than the dotted or dashed lines.

The dependance of $\xi_\theta(\Delta z)$ [for the DR41 sample] on the different RSFs is shown in Figure 5.2. Different histograms correspond to the different RSFs. It is evident that $\xi_\theta(\Delta z)$ is quite sensitive to different RSFs, especially at small and large Δz. Some distinctive peaks at $\Delta z > 0.05$ in S88 vanish or are compressed significantly by choosing certain RSFs (*e.g.*, the first RSF and the one based on random redshift assignments with a Gaussian

dispersion). However, some high peaks around $\Delta z \sim 0.04$ do not disappear under any reasonable choice of the RSF, confirming the S88 effect. It is valuable to keep in mind that our inaccurate knowledge of the RSF can quite easily lead to a $\sim$ 25% - 30% uncertainty in $\xi_\theta(\Delta z)$ although the dependence of the spatial correlation function $\xi(r)$ on the different RSFs is much weaker than that of $\xi_\theta(\Delta z)$ (less than 5% difference for the different RSFs models at $r < 50\ h^{-1}$ Mpc).

In the following analysis we use the RSF represented by the solid line of Figure 5.1 (RSF No 1) for the DR41 sample but note that our final results are mostly independent of this choice. The cluster density distribution of the DR40 sample with its smooth fit and the 'Deep' samples are plotted in Figure 5.3. A smooth function does not fit nicely the density distribution of the 'Deep' sample and we therefore use the RSF based on random assignments of the observed redshifts perturbed with a Gaussian dispersion of $\sigma_z = 0.01$.

5.2.3 Consistent comparison between three samples

S88 examined the redshift correlation functions $\xi_\theta(\Delta z)$ for the DR41 sample at angular separations $0° \leq \theta \leq 10°$ and $10° \leq \theta \leq 25°$, and for the DR40 sample at separations $0° \leq \theta \leq 6°$ and $6° \leq \theta \leq 12°$. SE91 analysed the 'Deep' sample using the redshift correlation function $\xi_{r_p}(R_z)$ at projected separations $0 \leq r_p \leq 10\ h^{-1}$Mpc and $10 \leq r_p \leq 20\ h^{-1}$Mpc. Both studies have shown the same tendency; $\xi_\theta(\Delta z)$ and $\xi_{r_p}(R_z)$ do not vanish at large line-of-sight separations, which S88 and SE91 ascribed as evidences of strong cluster contaminations.

We should point out that the projected separations used in these two studies are quite different; angular separations of 10° correspond for the DR41 and DR40 samples to projected separations of $\sim 30\ h^{-1}$Mpc. In order to properly study the contamination effect using different samples, it is important to use the same physical projected separation. If the contamination effects are due to a unique physical process, they should show up at similar projected separations in the different samples. Furthermore, we should expect more contamination in samples including $R = 0$ clusters because of the higher cluster density and the possible incompleteness of the $R = 0$ clusters in the catalogue (Abell 1958). So a comparison between samples of different richness can give us an indication whether contamination is important. We should expect contaminations to be more significant at smaller angular and projected separations than in larger ones. Therefore, we feel that it is important to make a consistency check, applying the same technique and using the same projected separation on samples of different richness.

For the two shallow samples we study two bins in θ: $0° < \theta < 10°$ and $10° < \theta < 25°$, which are the ones used by S88 for the DR41 sample. Since the 'Deep' sample is about 3 times deeper than the DR41 and DR40, we use $0° < \theta < 3.3°$ and $3.3° < \theta < 8.3°$. The redshift correlation function $\xi_\theta(\Delta z)$ within these angular separations is shown in Figs. 5.4(a) and 5.4(b). The results are very instructive:

1.) On all angular and redshift separations, $\xi_\theta(\Delta z)$ of the DR40 sample is less than that of the DR41 sample. In fact, $\xi_\theta(\Delta z)$ of the DR41 sample is about 2 times larger than that of the DR40 sample [with only exception at $\Delta z > 0.035$ in the range $0° < \theta < 10°$ where the two samples have comparable $\xi_\theta(\Delta z)$]. This is consistent with the well-known richness dependent cluster clustering and inconsistent with the

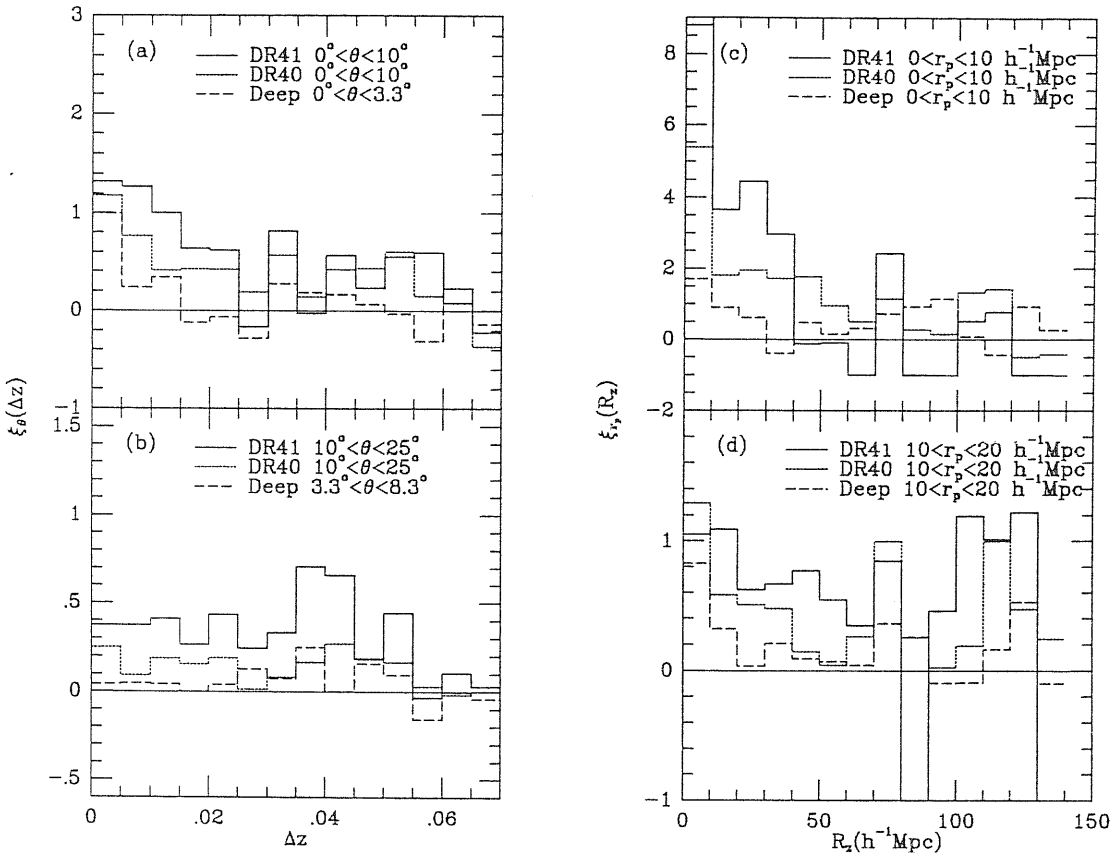

Fig.5.4 — The redshift correlation functions $\xi_\theta(\Delta z)$ [panels (a) and (b)] and $\xi_{r_p}(R_z)$ [(panels (c) and (d)] of the three Abell cluster samples.

expectation the contaminations would have affected more the $R \geq 0$ sample.

2.) The only significant ($\geq 2\sigma$) peaks in $\xi_\theta(\Delta z)$, at the large angular separation range, appear in the DR41 sample at $\Delta z = 0.0375$ and 0.04. These peaks are even larger than at the same Δz of the smaller angular separation range while, in general, we would expect contaminations to be more significant at the latter angular range.

3.) At the smaller angular range, $\xi_\theta(\Delta z)$ of the 'Deep' sample decreases much faster than that of the shallow samples and it is consistent with zero, within the typical Poisson error ($\sigma_\xi \approx 0.23$) for $\Delta z > 0.015$ (error bars have not been plotted on Figure 5.4 for clarity). The noticeable peaks at large Δz which show up in the two shallow samples do not appear in the 'Deep' one. Note that also for the 'Deep' sample we get that $\xi_\theta(\Delta z > 0.02)$ has similar or even higher values at the large angular separation range than at the smaller one.

Clearly all these points are contrary to the suggestion that contaminations are the main cause of the Sutherland effect.

Now we turn to the redshift correlation function $\xi_{r_p}(\Delta z)$ within a fixed projected separation range. We choose the same projected separations as in SE91. The results are

presented in Figs. 5.4(c) and 5.4(d) and can be summarized as following:

1.) For the DR41 sample, $\xi_{r_p}(R_z)$ is consistent with no correlation at $R_z > 40h^{-1}$Mpc for $r_p < 10\ h^{-1}$Mpc, while it does have some positive peaks at large $R_z = 50 \sim 130\ h^{-1}$Mpc for $10 < r_p < 20\ h^{-1}$Mpc most of which do not show up at the smaller r_p range (and at the same R_z).

2.) At the small projected separation range and for $R_z \geq 40\ h^{-1}$Mpc, $\xi_{r_p}(R_z)$ is generally higher in the two $R \geq 0$ samples than in the DR41 sample, which is consistent with our expectation that some contaminations may exist in the $R \geq 0$ samples.

3) At both, the small projected separation range with $R_z \leq 40\ h^{-1}$Mpc and the large one with the whole R_z range, $\xi_{r_p}(R_z)$ is systematically lower in the DR40 and 'Deep' samples than in the DR41 sample, consistent with richness-dependence clustering as proposed by BS83. We, therefore, have no evidence for significant contamination effects for $r_p \geq 10\ h^{-1}$Mpc even in the $R \geq 0$ samples.

Because of strong clustering and the small number of clusters involved, some significant peaks in the shallow samples might come from the particular way with which clusters are spatially distributed (e.g., certain orientation of supercluster chains, supercluster elongations, large voids, etc). The similarity of the shape of the redshift correlation functions of the DR40 and DR41 samples (which cover the same region of the sky), but with amplitudes about a factor 2 lower, is completely consistent with the dependence of cluster clustering on cluster richness, as found by BS83. However, for the DR40 sample some peaks in ξ_θ and ξ_{r_p} at the small angular and projected separations which are as high or higher than those of the DR41 sample, could be, at least partially, due to contamination effects.

In conclusion of this section; we have carefully examined the correlation functions $\xi_\theta(\Delta z)$ and $\xi_{r_p}(R_z)$ at two separation ranges for three redshift samples of Abell clusters. Our detailed, *consistency* check does not support that the distinctive peaks, seen in the two correlation measures, are mainly due to the contamination effects, as suggested by S88 and SE91. More precisely, we found no evidence for any significant contamination of the richness $R \geq 1$ cluster sample but we did find weak evidence, mostly from the $\xi_{r_p}(R_z)$ analysis, that the $R \geq 0$ samples (especially the DR40 sample) could be affected by contaminations. However, these effects could influence the clustering analysis of the $R \geq 0$ samples only at small projected separations ($r_p \leq 10\ h^{-1}$Mpc). Although the contaminations seem not to be the main cause of the distinctive peaks in the $\xi_{\mathcal{A}}(\mu)$, it is difficult with the present analysis to quantify the amount of contaminations in the Abell catalogue.

5.3 Comparison with simulations

In this section we will attempt to assess the probability of observing significant peaks in the redshift correlation function by analysing simulated cluster catalogues, which have similar clustering properties as the real samples and which are free, by construction, of the contamination effects.

5.3.1 Simulated cluster catalogues

The method we use to generate our simulated catalogues is similar to that of Postman *et al.* (1989) and it will be described in detail in a forthcoming paper (Plionis, Valdarnini & Jing 1991). Here we shall only briefly describe the main points of our simulation method.

The simulations are performed in a cubic box with 64^3 grid cells corresponding to a volume 640 h^{-1}Mpc $\times$ 640 h^{-1}Mpc $\times$ 640 h^{-1}Mpc. Our simulated clusters are identified as high peaks of a density fluctuation field which is a Gaussian random field with a power-law power spectrum:

$$P(k) = \langle \mid \delta_k \mid^2 \rangle \propto k^n \tag{5.4}$$

A large number of points (> 70000) are randomly distributed inside the cube and each of them is assigned a density contrast $\delta_{\vec{g}} = \nu\sigma$ (where σ is the *rms* density fluctuation within the cube and $\vec{g}$ is the nearest grid point to the particle). Those particles with $\nu > \nu_{min}$ (here $\nu_{min} = 1.3$) are chosen as clusters. The amplitude and slope of the power spectrum are so adjusted that the simulated clusters have a two-point correlation function, $\xi = (r_\circ/r)^\gamma$, in the range of $10 \sim 70$ h^{-1}Mpc with $r_\circ \geq 20$ h^{-1} Mpc and $\gamma = 1.8$. We generate two sets of simulated cluster catalogues (of 50 simulations each); one with $\langle r_\circ \rangle = 20$ h^{-1} Mpc, corresponding to the DR40 and 'Deep' sample correlation function and $\langle r_\circ \rangle = 25$ h^{-1} Mpc, corresponding to that of the DR41 sample.

Our final simulated cluster catalogues have the same geometrical boundaries as the real data and the individual clusters have been selected according firstly to the galactic latitude selection function and secondly applying the real-sample RSF. This procedure was stopped when the number of points was the same as the number of clusters in the real catalogues. To construct simulated cluster catalogues that resemble the DR41 or DR40 samples we set the *observer* at the centre of the simulation box while to simulate the 'Deep' sample we place the *observer* at one of the cube vertex. The RSF we use for both the DR40 and DR41 simulated samples is the smooth solid line shown in Figure 5.1 and 5.3. For the 'Deep' sample we use the RSF obtained by a random assignment of the observed redshifts perturbed by a Gaussian dispersion $\sigma_z = 0.01$. Note, however, that the redshift correlation function of the simulated catalogues depend rather weakly on the RSF choice, since the effects of the RSF are canceled by using the same RSF in the random catalogues which are used in order to obtain $\xi_{\mathcal{A}}(\mu)$.

5.3.2 Qualitative comparison of simulations with observations

Using the simulated cluster catalogues, we find that the distinctive peaks in the redshift correlation functions are quite common even at large redshift separations. As an illustration, we choose to present $\xi_\theta(\Delta z)$ of the simulated DR41 sample (qualitatively similar results are also obtained from the other samples).

In Figure 5.5, we plot the redshift correlation functions $\xi_\theta(\Delta z)$ for the first six DR41 simulated cluster catalogues (this choice is equivalent to a random one). Some features in the figure are very noticeable. Peaks and valleys are quite common even at large Δz. The amplitude of these peaks are comparable with those found in the observed sample. The peaks (or valleys) often appear coherent over some large range of redshift separations, Δz, probably because of the specific location of cluster associations in space.

In Figure 5.6, we plot $\xi_\theta(\Delta z)$ for another four simulated samples which have more similar $\xi_\theta(\Delta z)$ to that of the real data. In these simulated catalogues, $\xi_\theta(\Delta z)$ remain positive

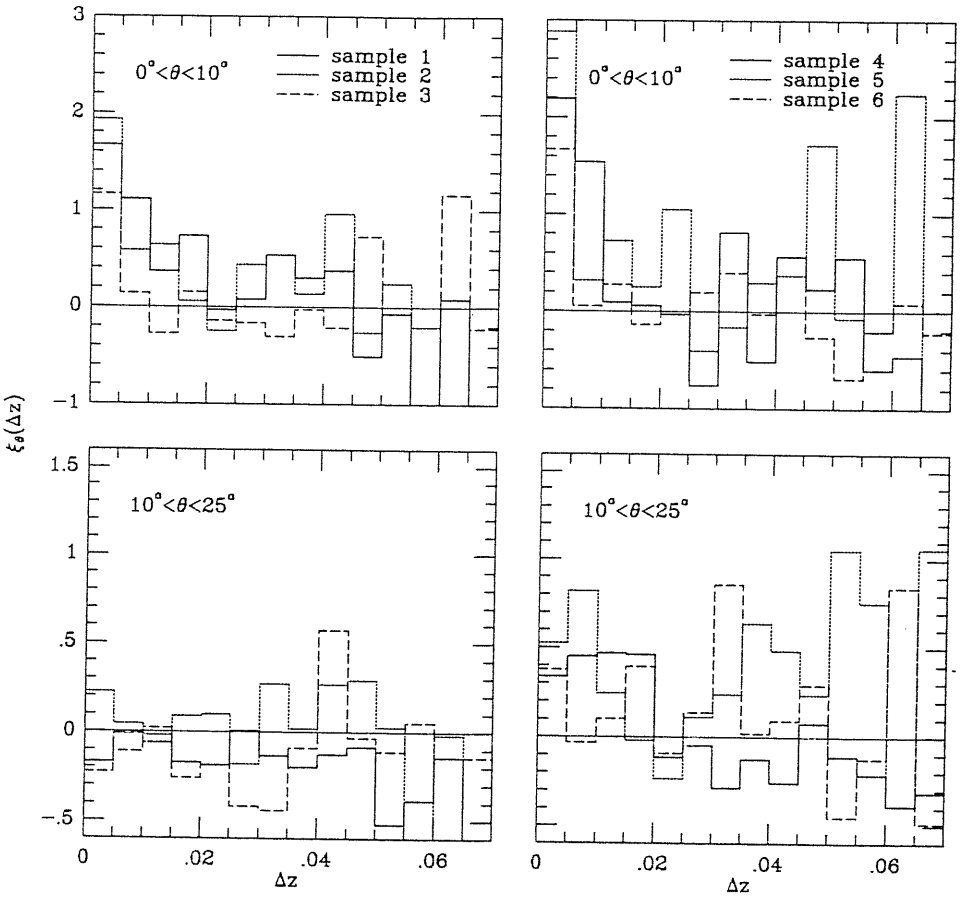

Fig.5.5 — The redshift correlation functions, $\xi_\theta(\Delta z)$, of the first six simulated DR41 cluster samples (this choice is equivalent to a random one).

on (almost) all redshift separations in the both small and large angular separations. We have checked whether this fact arises due to stronger cluster clustering in these samples, by calculating the two-point spatial correlation function $\xi(R)$ (Figure 5.7). Different symbols represent the correlation function of different samples, as indicated in the figure. The mean $\xi(R)$ over the fifty simulated samples and its standard deviation, σ, is also shown (dotted lines). We find no evidence that $\xi(R)$ of these four samples are systematically higher than the mean simulation values or than the real data values. This supports our expectations, stated in the previous section, that the distinctive peaks of the redshift correlation function in the real data are probably due to certain spatial superclustering patterns rather than being due to the contamination effects. Thus, the method of S88 to remove these peaks, which he regarded as being due to projection effects, would artificially remove signal of real clustering.

Another interesting feature that has been observed in the Abell cluster samples is the *redshift elongation* or *Finger-of-God* effect (Bahcall, Soneira & Burgett 1986). This manifests itself in the scatter-diagram of cluster pair separations as a systematic excess of pairs along the redshift axis R_z with respect to the orthogonal R_δ or R_α axis (declination and right ascension axes respectively), while limiting the separations along the third axis to $< 5\ h^{-1}$ Mpc. Bahcall, Soneira & Burgett (1986) attributed this effect to the existence

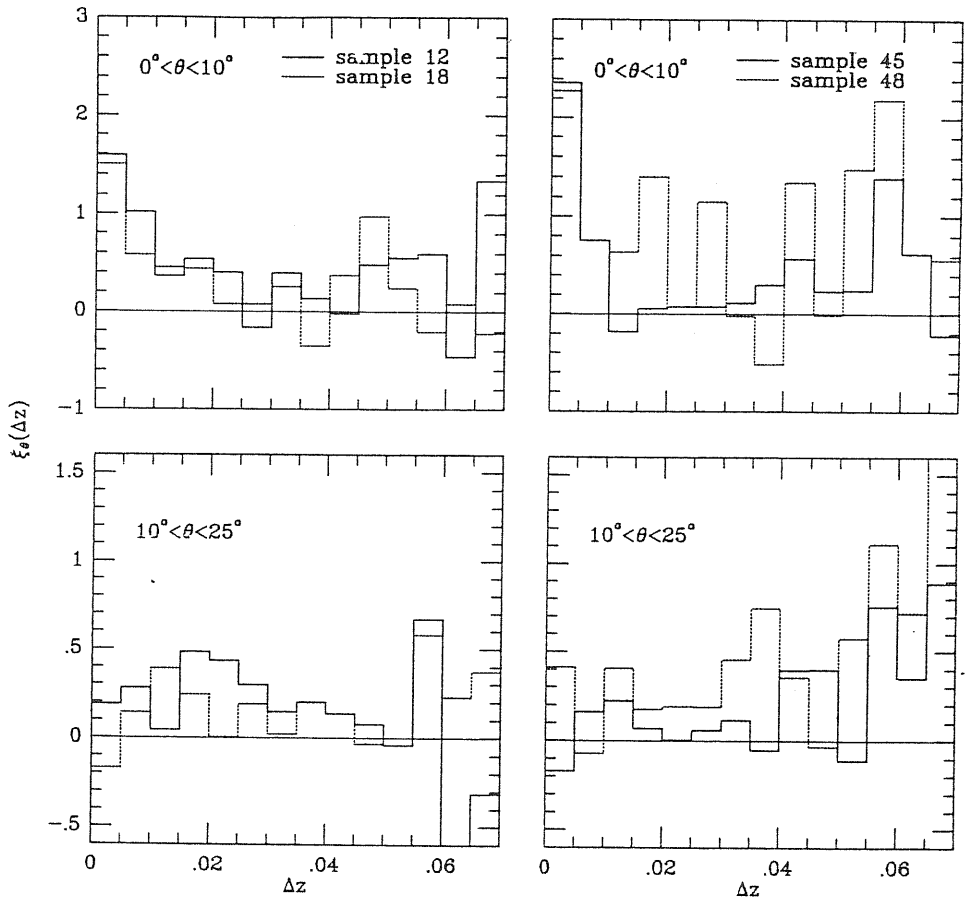

Fig.5.6 — The redshift correlation functions, $\xi_\theta(\Delta z)$, of four simulated DR41 cluster samples that resemble the features in $\xi_\theta(\Delta z)$ of the observed DR41 sample.

of large ($\sim$ 2000 km s^{-1}) peculiar motions of clusters that belong in superclusters. To test this suggestion we checked whether this effect is apparent in any of our simulations (which we remind the reader are not dynamically evolved). Indeed, we did find that some of our simulations showed the same elongation effect, along the R_z axis (Figure 5.8), while some showed similar elongation effects along the orthogonal axis and others showed no such effects at all. However, the real data show a slightly crispier elongation along the R_z axis. Therefore, we conclude that a big part of the observed elongation effect could arise from low-order $(2-p)$ cluster clustering coupled with the small number of clusters which often result in supercluster elongations along the line-of-sight (geometrical elongation was suggested as a possible explanation by Bahcall, Soneira & Burgett 1986). The rest of the signal could come from cluster peculiar velocities but of significantly lower amplitude < 1000 km s^{-1}. Such cluster peculiar velocities are suggested by independent estimates (e.g., Aaronson *et al.* 1986, Lucey and Carter 1988; Huchra *et al.* 1990).

5.3.3 Quantitative comparison of simulations with observations

Now we quantitatively assess the statistical significance of our results. In Figure 5.9 and 5.10, we present the mean simulation redshift correlation functions (dotted lines) as well as those of the real samples (solid lines). In both angular separations (Figure 5.9),

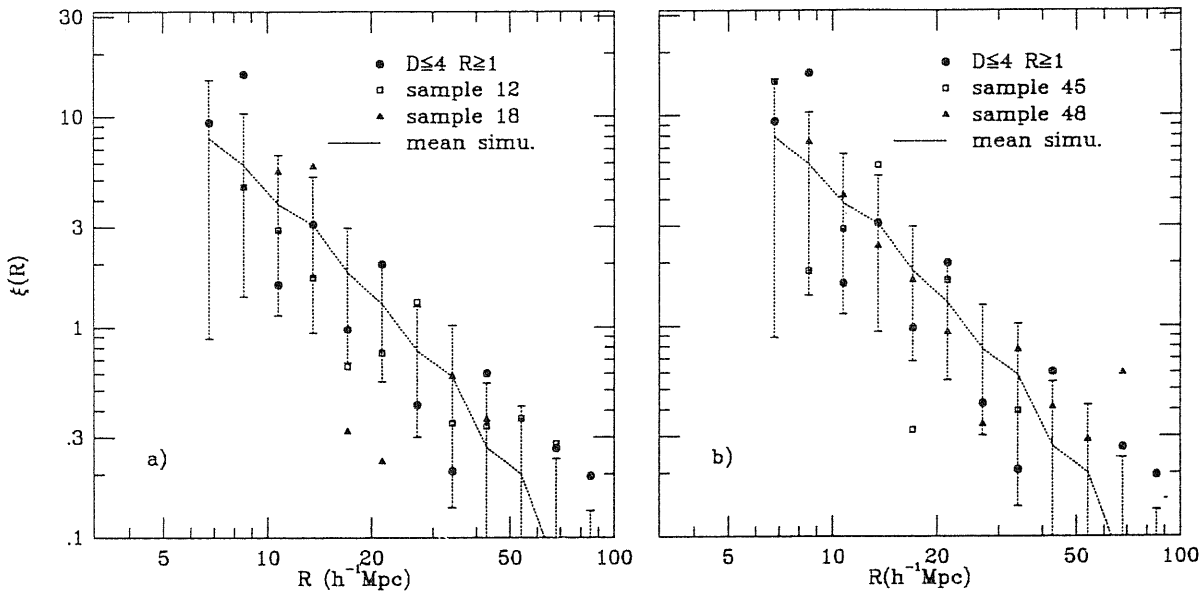

Fig.5.7 — The two-point spatial correlation functions, $\xi(R)$, of the the four simulated DR41 cluster samples of Fig.5.6 and of the DR41 sample. The mean values and the 1σ error bars from the 50 simulations are also plotted (dotted lines).

all $\xi_\theta(\Delta z)$ of the all three samples are consistent with the simulations within the $1 \sim 1.5\sigma$ significance level except for two peaks of the DR40 sample ($0° < \theta < 10°$ at $\Delta z = 0.0275$ and 0.0525) and for two peaks of the DR41 sample ($10° < \theta < 25°$ at $\Delta z = 0.0375$ and 0.04) which lie at $\geq 2\sigma$ level. Similar results are obtained analysing $\xi_{r_p}(R_z)$ (Figure 5.10). The most significant deviations ($2 \sim 3\sigma$) between the observed and simulation average values of $\xi_{r_p}(R_z)$ appear at the smaller projected separation range between 30 $h^{-1} \leq R_z \leq 40$ h^{-1} Mpc only for the DR41 and DR40 samples. No such deviations are apparent in the 'Deep' sample.

To quantify these deviations we apply the χ^2-test. The χ^2 for each sample is estimated by:

$$\chi^2 = \sum_{i=1}^{14} \frac{[\xi_{\mathcal{A}}(\mu_i) - \langle \xi^s_{\mathcal{A}}(\mu_i) \rangle]^2}{\sigma_i^2(\xi)} , \tag{5.5}$$

where $\xi_{\mathcal{A}}(\mu_i)$ is the redshift correlation function of the real sample and $\langle \xi^s_{\mathcal{A}}(\mu_i) \rangle$ is its mean value from the 50 simulations, while the summation is over 14 redshift separation intervals. The error model for $\sigma_i^2(\xi)$ is constructed by taking into account three types of errors which enter the $\xi_{\mathcal{A}}(\mu)$ estimation; the Poissonian error due to the discreteness of the cluster distribution, the fluctuations due to strong clustering and uncertainties which arise from our inaccurate knowledge of both redshift and galactic selection functions. The first two types of errors could be well represented by the standard deviation $\sigma_s(\xi)$ of the simulations. However, the third type of error is not included in σ_s because we use the same selection functions to select simulated clusters and to calculate correlation functions. Although this kind of error is not known *a priori*, the discussion in §5.2 showed that the uncertainty in $\xi_{\mathcal{A}}$, due to such errors, could be as high as 25% - 30%. Assuming that the

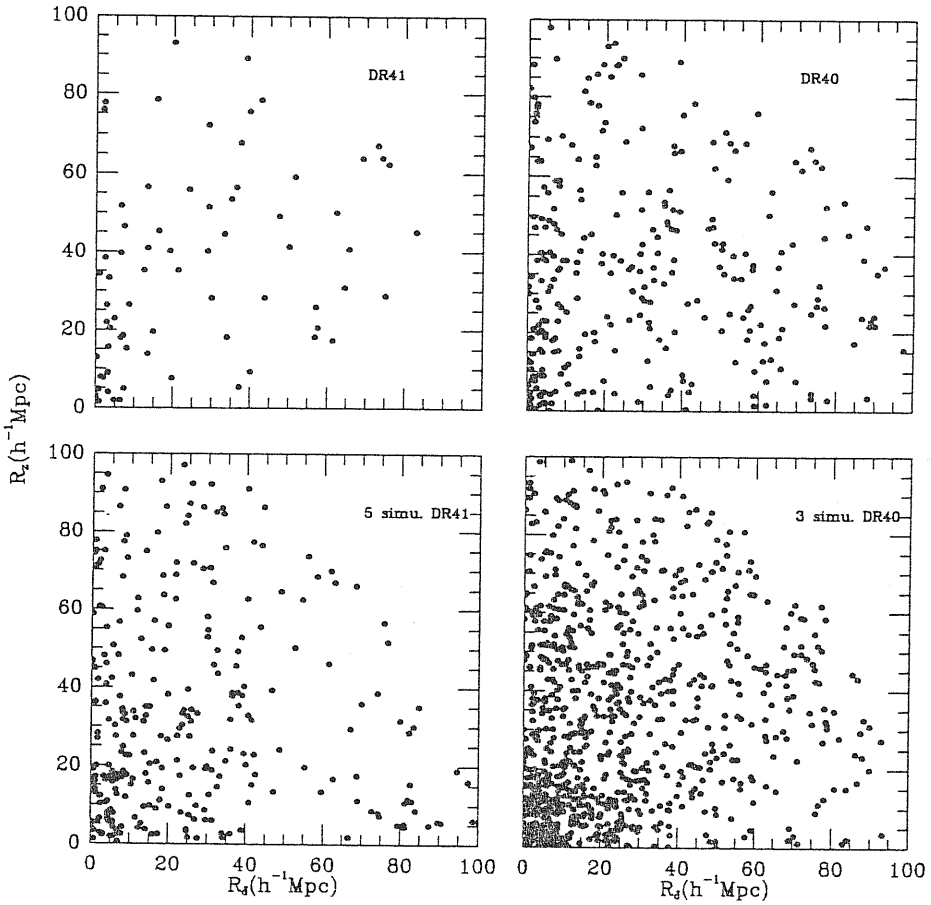

Fig.5.8 — Scatter diagrams of Abell cluster pairs (upper panels) and simulated pairs (lower panels) in the R_δ - R_z plane (in h^{-1} Mpc), with separations along the perpendicular plane $< 5\ h^{-1}$ Mpc (as in Bahcall *et al.* 1986). The elongation along the R_z direction is apparent in the real but also in the simulated data (although in the real case it seems crispier). The simulated catalogues used here where selected exactly because they appeared to have similar R_z - R_δ diagrams with those of the real data.

different types of errors are independent we take as our error model the following:

$$\sigma_i^2(\xi) = \sigma_s^2 + \eta^2 \xi_{\mathcal{A}}^2(\mu) \ . \tag{5.6}$$

In the following discussion, η is set to 0.25. The results of the χ^2 test are listed in the second to fourth column of Table 5.1. P($> \chi^2$) represents the probability that the real cluster samples have significantly larger deviations from the simulation mean values, indicating at what level is our suggestion, that the high peaks of $\xi_{\mathcal{A}}$ are due to strong clustering, accepted. The results clearly show that the observed redshift correlation functions are consistent with real clustering. The lowest two probabilities for $(\mathcal{A}, \mu) = (\theta, \Delta z)$ and (r_p, R_z) are 0.17, 0.25 and 0.07, 0.32 respectively, still significantly high. The lowest probabilities, of 0.17 and 0.07, occur for the DR40 sample at the smaller angular and projected separation range respectively. This is consistent with our expectation that projection effects

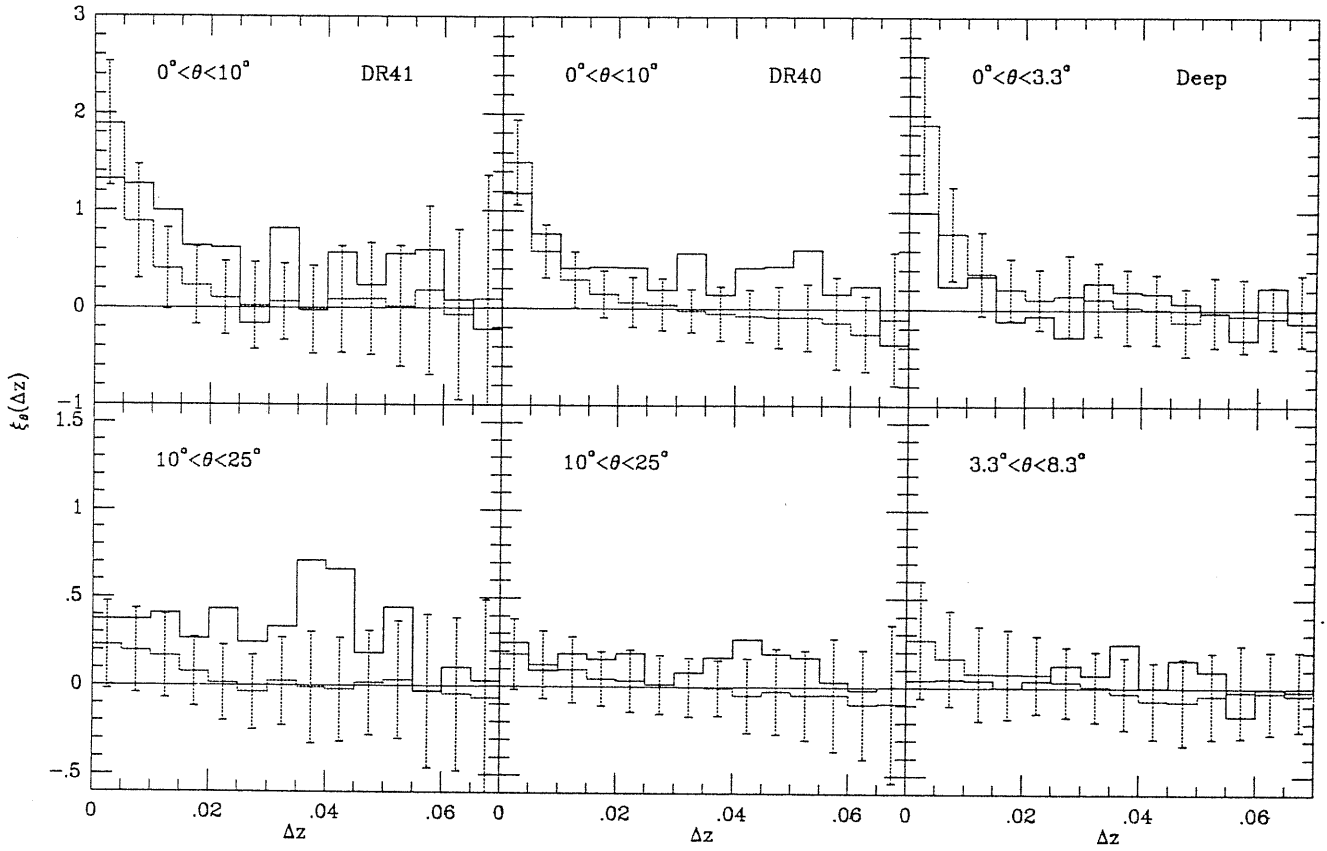

Fig.5.9 — The redshift correlation functions $\xi_\theta(\Delta z)$ of the three samples compared with the mean value of the 50 simulations. Error bars represent 1σ fluctuations.

Table 5.1

χ^2 tests of $\xi_\theta(\Delta z)$ and $\xi_{r_p}(R_z)$

Sample	θ [in °]	χ^2	P($>\chi^2$)	r_p [in h^{-1} Mpc]	χ^2	P($>\chi^2$)
DR41	$0 < \theta < 10$	9.17	0.82	$0 < r_p < 10$	15.9	0.32
	$10 < \theta < 25$	17.1	0.25	$10 < r_p < 20$	12.0	0.60
DR40	$0 < \theta < 10$	18.8	0.17	$0 < r_p < 10$	22.7	0.07
	$10 < \theta < 25$	6.43	0.95	$10 < r_p < 20$	10.7	0.71
'Deep'	$0 < \theta < 3.3$	7.25	0.92	$0 < r_p < 10$	16.2	0.30
	$3.3 < \theta < 8.3$	4.4	0.99	$10 < r_p < 20$	4.90	0.99

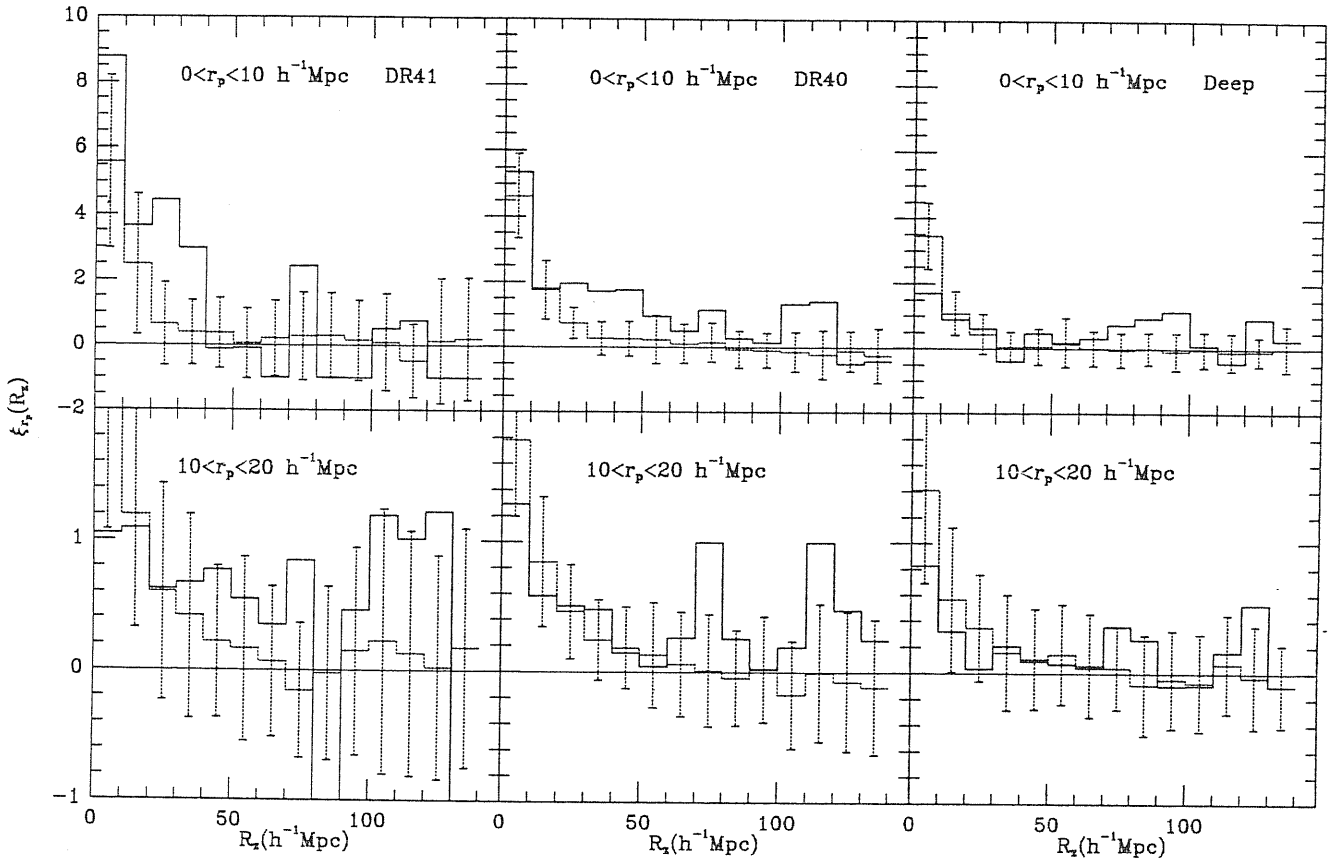

Fig.10 — As in Fig.5.9 but for the redshift correlation functions $\xi_{r_p}(R_z)$.

should affect the $R \geq 0$ samples more efficiently than the $R \geq 1$ samples. Note, however, that these effects are marginally (in the sense that even a probability of 0.07 is still large) noticeable in the DR40 sample but not at all in the other $R \geq 0$ sample ['Deep'].

The test is rather sensitive to the existence of high peaks. For example, if in the DR41 sample we ignored the two peaks at $z \approx 0.04$ and $10° < \theta < 25°$, the $P(> \chi^2)$ would be raised from 0.25 to 0.63. These two peaks result mainly from 16 clusters in two well-known superclusters: the Hercules supercluster at $z \sim 0.035$ (Chincarini, Rood & Thompson 1981; Bahcall & Soneira, 1984) and the Corona Borealis supercluster at $z \sim 0.075$ (Bahcall & Soneira 1984; Postman, Geller & Huchra 1988). If these 16 clusters were excluded *a posteriori*, $\xi_\theta(\Delta z)$ would be lowered to 0.25, well within 1σ level. It seems, therefore, that these peaks are more probably produced by real superclustering rather than by contamination effects.

Furthermore, the fluctuations of the two-point (redshift) correlation function depend strongly on the higher order cluster clustering; the more high-order clustering, the more fluctuations in ξ (see *e.g.*, Peebles 1980). We have checked the three-point correlation function for the simulated clusters and found it to be about 2 times weaker ($Q_{sim} \approx 0.4$) than the value for the Abell cluster catalogue (Jing and Zhang 1989; Tóth, Hollósi & Szalay 1989; Jing & Valdarnini 1991; Gott, Gao & Park 1991). Clearly, the probabilities $P(> \chi^2)$ in Table 5.1 would be even higher if the simulated clusters had stronger high-

order clustering and therefore some significantly high peaks, seen especially in Figure 5.10 at small R_z's, could be a reflection of the stronger high-order clustering of the Abell clusters.

Therefore, our simulations show that both $\xi_{r_p}(R_z)$ and $\xi_\theta(\Delta z)$ of the observed samples are consistent with being the result of real clustering with weak evidence for some contamination effects in only one sample (DR40). This means that we do not need to invoke the contamination effects to explain *most* of the distinctive features in $\xi_{r_p}(R_z)$ and $\xi_\theta(\Delta z)$ appearing on large redshift separations.

5.4 Conclusions and implications

1.) Six different redshift selection functions (RSFs) for the DR41 sample are used to test the sensitivity of redshift correlation function to the RSF choice. We found that our inaccurate knowledge of the RSF can easily result in a $\sim 30\%$ uncertainty in the redshift correlation estimates. Any reasonable choice of the RSF, however, cannot remove all the high peaks seen in the redshift correlation functions at large redshift separations.

2.) Our careful and consistent comparison of $\xi_{\mathcal{A}}(\mu)$ between three Abell cluster samples does not support the contamination origin of these peaks, as was proposed by S88 and SE91. We find no evidence for significant contamination of the DR41 sample. However, we cannot exclude the possibility of moderate contamination effects in richness $R \geq 0$ samples. The observed properties of redshift correlation functions can be easily interpreted as the results of strong, richness-dependent clustering of *small numbers* of clusters, *i.e.*, the peaks in $\xi_{\mathcal{A}}$ could be due to some specific superclustering pattern of clusters (*e.g.*, geometrical elongation).

3.) Our suggestion that these peaks could originate from real clustering, was tested by numerical simulations. We constructed sets of simulated cluster catalogues which have the same sky boundaries, same selection functions, same number of clusters, and same two-point correlation functions as the real samples. Of course the simulated catalogues are free of the contamination effects and the coherent peaks (or valleys) observed in the redshift correlation function, on large Δz or R_z, are very common also in the simulations. The χ^2-test shows that we have more than $15\% \sim 30\%$ probability to obtain peaks in $\xi_{\mathcal{A}}(\mu)$, as large as the ones observed in the real cluster samples, due only to the low-order $(2-p)$ clustering of a small number of clusters and the fact that we have only one realization of the process that forms clusters. Therefore, we do not need to invoke the contamination effects to interpret the features seen in the observed ξ_{r_p} and ξ_θ.

4.) It is important to emphasize here that previous confrontations of the observed ξ_{cc} with that predicted by theories of galaxy formation are mainly based on the result obtained from the DR41 sample (BS83). Our results support the BS83 results and therefore imply that the biassed CDM model is in gross disagreement with the observed cluster clustering, as originally thought.

5.) The elongation of cluster pairs in the redshift direction, found by Bahcall, Soneira & Burgett (1986) occurs quite often in our simulations. This suggests that the effect could be explained as being partly due to the statistical fluctuations in $\xi_{\mathcal{A}}$, without assuming the large ($\sim$ 2000 km s^{-1}) cluster peculiar velocities advocated by Bahcall *et al.*. In fact, even Bahcall *et al.* noted that such an effect may partly come from peculiar velocity of clusters but partly also from a geometrical elongation of superclusters.

‡The materials presented in this chapter are based on our paper: Jing, Y.P., Plionis, M. & Valdarnini, R. 1991, *The Astrophysical Journal*, (submitted)

6

The Three-point Correlation Functions of Abell Clusters

The two-point correlation function of rich clusters found by Bahcall and Soneira (1983) is of great value to understanding the large scale structures in the Universe. However, as is well known, a full description of the distribution of Abell clusters needs all N-point correlation functions. A statistical study of the three point correlation function would be necessary. Furthermore, because the three-point correlation function ζ is independent of the two-point function ξ, we would expect that ζ will put another constraint on the galaxy formation theories and therefore narrow the possible models. In this chapter, I shall present our original contributions to these statistics.

6.1 The three-point angular correlation functions of $R \geq 1$ Abell clusters

Our study is based on the statistical catalog of $R \geq 1$ Abell clusters with high galactic latitude $\mid b^{II} \mid \geq 30°$ (Abell 1958). This sample includes 1651 clusters, of which 1055 are distributed in 2.64 sr of the northern hemisphere and the rest are in the 1.62 sr of the southern hemisphere. Its survey boundaries were given in Table 1 of Abell (1958).

We estimate the angular three-point correlation function $z(\theta_{12}, \theta_{23}, \theta_{31})$ following eq.(3.1.4b). Instead of using the variables θ_{12}, θ_{23}, and θ_{31}, we use the another set variables θ, u and v as in §4.3.2. In order to estimate $< DDR >$ and $< RRR >$ of eq.(3.1.4b), we construct a random sample of twice number of points than the real sample. As usual, the selection function eq.(5.3) is adopted in the construction of the random sample.

In order to improve the accuracy of estimating z, we used the interpolation techniques of Peebles and Groth (1975). We take the constant logarithmic intervals in θ, $\Delta\theta/\theta =$ constant, so that at small θ, and for the fixed u and v, the expected counts $< RRR > \propto \theta^4$ and $(< DDR > -3 < RRR >) \propto \omega(\theta)\theta^4$. We use these interpolation formulae to estimate the $< RRR >$ and $< DDR >$ for those intervals in which $< RRR >$ or/and $(< DDR > -3 < RRR >)$ are less than 200. To good accuracy, $\omega(\theta) \propto \theta^{-0.9}$ for Abell clusters (see below).

Since computer cost is rapidly increased with the increase of θ_{31} ($\propto \theta_{31}^4$), we limit our estimation to $\theta_{31} \leq 10°$ triplets. Evidently, the cutoff is reasonable for our study because, as we know, the two-point angular correlation function of $R \geq 1$ Abell clusters was also well determined to a similar separation range. The determination of z starts at $\theta_{12} = 0.5°$.

Our results for the whole statistical sample of $R \geq 1$ Abell clusters are presented in Figure 6.1. In the figure, the constant intervals $\Delta \log_{10} u = 0.2$ and $\Delta \log_{10} \theta = 0.1$ are taken for the variables u and θ, respectively. For the variable v, two bins $0 \leq v \leq 0.5$ and $0 \leq v \leq 0.5$ are used. The capital letters for each bin in the figure correspond to those given in Table 1, and the shape parameters u, v of the corresponding triplets are also listed in the table. The vertical coordinate $\log_{10} z$ in the figure for every bin is shifted by a factor given in Table 6.1. The filled triangle represents the averaged value of z over the two neighboring bins, in one of which z is very small (same in the following).

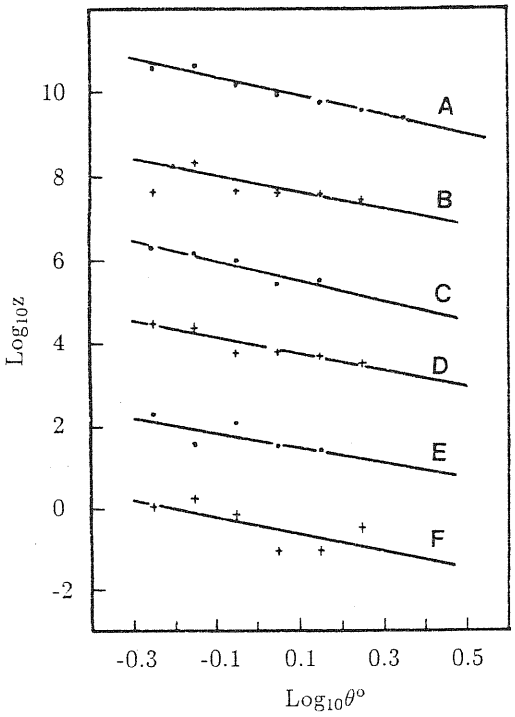

Fig.6.1— The three-point angular correlation function z of the whole statistical sample. Upper case letters correspond to the shape range (u,v) listed in Table 6.1. Estimates have been multiplied by a power of 10, as indicated in Table 6.1. The straight lines represent the least-square power-law fits.

Table 6.1

THE b-VALUES OF THE STATISTICAL SAMPLE

	$\log u$		
v	0.0–0.2	0.2–0.4	0.4–0.6
0.0–0.5	A × 10^{10}	B × 10^{8}	C × 10^{6}
	−2.26	−2.03	−2.43
0.5–1.0	D × 10^{4}	E × 10^{2}	F
	−2.02	−1.80	−2.10
Mean value	-2.10 ± 0.21		

We can be sure, from Figure 6.1, that there exists three-body correlation function among Abell clusters. This is expected, since there are many complex large-scale structures composed of Abell clusters(e.g., Bahcall & Soneira 1984; Tully 1987, and references therein). For quantitative analysis, a power-law form for z,

$$\log_{10} z = a + b \log_{10} \theta, \tag{6.1}$$

is assumed. The least-square fit to $z(\theta, u, v)$ (with u and v fixed) gives value b for every bin. All values of b are listed in Table 6.1, and we can see that from bin to bin, the values of b do not change much, and remain close to -2.0. Assuming all 6 b-values are statistically independent for simplicity (some coherence might exist), then we get the mean value $\bar{b}$:

$$\bar{b} = -2.10 \pm 0.21, \tag{6.2}$$

where the quoted error is the standard deviation of six b-values from the mean. The above value of $\bar{b}$ (about twice the slope of the two-point angular correlation function) reminds us the three-point correlation of Abell clusters may also have a hierarchical form,

$$z = q(\omega_1\omega_2 + \omega_2\omega_3 + \omega_3\omega_1), \tag{6.3}$$

just as for galaxies, here q is a constant.

The angular correlation functions $\omega(\theta)$ have been estimated by Bahcall and Soneira (1983) for $D = 5 + 6$ Abell clusters (including separate determinations for the northern and for the southern portions). Their samples are almost the same as those used here. However, there is some difference between two sets of samples; namely, that in the present study $D \leq 4$ clusters are included. Also, random samples can be produced in the same way in estimating z and $\omega(\theta)$. Moreover, because only triplets with $0.5° \leq \theta_{12} \leq \theta_{31} \leq 10°$ are included, our determination fits $\omega(\theta)$ to statistical data for the similar angle range. For all these reasons, a more accurate determination of the constant q is to be obtained by our own estimation of $\omega(\theta)$

Thus we estimate the two-point angular correlation function for the three samples discussed here. The results are plotted in Figure 6.2. The least-squares fits $\omega(\theta) \propto \theta^{-\beta}$ to these data(excluding the 0.5°–0.64° bin) show that for these samples, the power slopes β are 0.87 (for the whole sample; hereafter SW), 0.78 (for the northern sample; SN), 0.90 (for the southern sample; SS), all very close to 0.90. The single-power fits give $0.89\theta^{-0.9}$ (SW), $0.75\theta^{-0.9}$ (SN), and $1.25\theta^{-0.9}$ (SS), respectively. These expressions are to be used through equation(6.3) to get q.

The single power-law fits $z \propto \theta^{-1.8}$ to the statistical data of Figure 6.1 give q for each (u,v) bin, listed in Table 6.2. We can see from the table that q remains almost a constant from bin to bin, and is nearly independent of triangle shape u and v. This means that the three-point correlation function of Abell clusters can be well represented by the scaling form(8), just as in the case of galaxies. Also, assuming all q values for each bin are statistically independent, we get their mean value:

$$\bar{q} = 0.68 \pm 0.14. \tag{6.4}$$

The three-point correlation functions have also been estimated for the northern and the southern portions separately. The results are plotted in Figure 6.3. The straight lines in the figure represent the single power law $z \propto \theta^{-1.8}$ fits, and the corresponding q values are given in Table 6.2. It can be easily found that the scaling form of equation (6.3) fits the statistical data of z of the southern and northern samples well. The mean q-values are 0.57 ± 0.19 for SN and 0.87 ± 0.20 for SS, both of which are in agreement with the estimation of the statistical sample. These results support the conclusion that z of Abell clusters has the hierarchical form, although, compared with the statistical sample, their fluctuations (especially of SN) are a little larger, which could be expected. There is a difference, although very slight, of ω and z between SN and SS. However, the cause is now unclear. It might be connected with the fact that the distribution of Abell clusters is a little more clumpy in the southern sky than in the northern sky. But it may also be caused by observational effects, such as the strip with "bad" Palomar plates at $\delta = 72°+$,

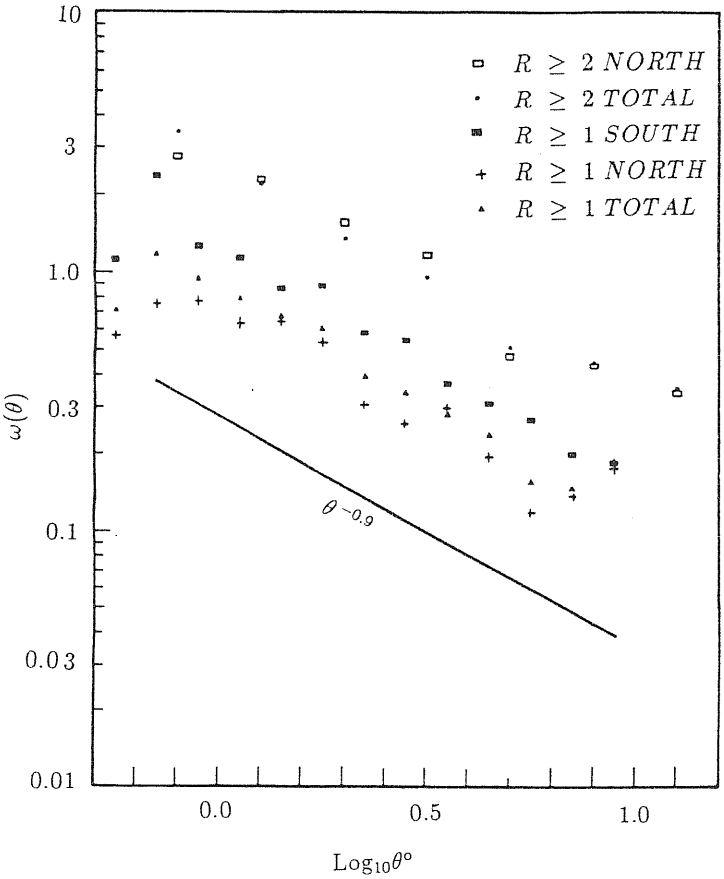

Fig.6.2 — The two-point angular correlation functions of the whole statistical sample for different zones and different richness classes.

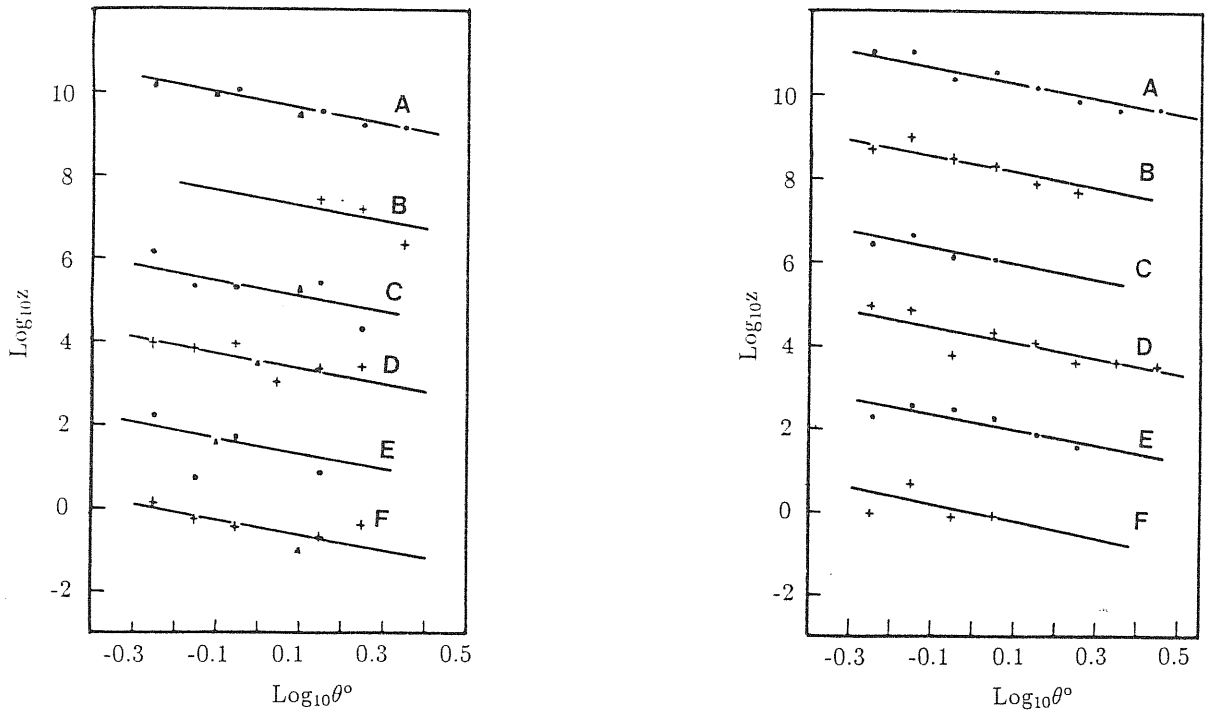

Fig.6.3 — The three-point angular correlation functions of *(a)* the northern sample and *(b)* the southern sample. Others are same as Fig.6.1, except that the lines represent single power-law $\theta^{-1.8}$ fits.

TABLE 6.2

THE q-VALUES FOR THREE SAMPLES

SAMPLE	v	Log u 0.0–0.2	0.2–0.4	0.4–0.6
All	0.0–0.5	0.760	0.674	0.903
	0.5–1.0	0.589	0.504	0.650
Mean value		0.680 ± 0.139		
South	0.0–0.5	0.956	1.071	1.081
	0.5–1.0	0.628	0.764	0.694
Mean value		0.865 ± 0.196		
North	0.0–0.5	0.597	0.437	0.495
	0.5–1.0	0.420	0.542	0.924
Mean value		0.569 ± 0.186		

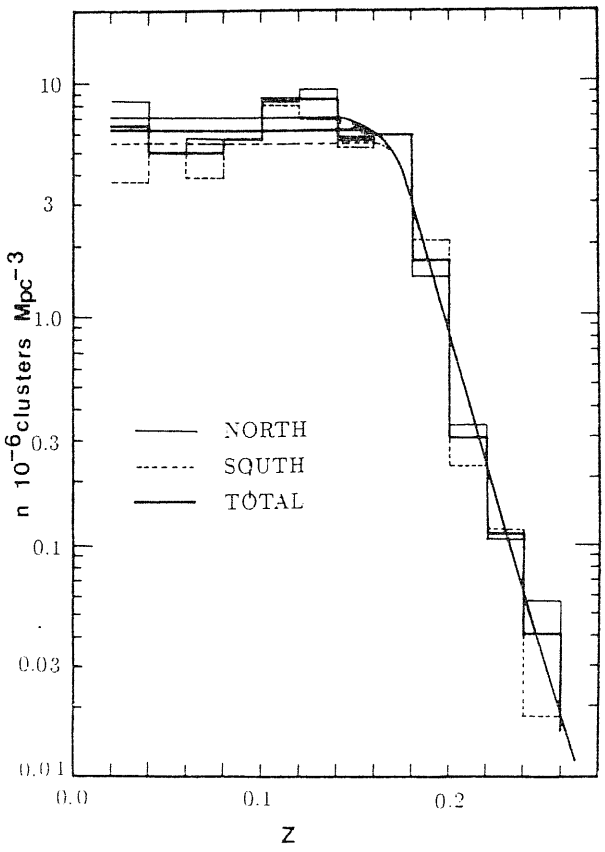

Fig.6.4 — Spatial density distributions vs. redshift of northern sample (*thin lines*), southern sample (*dashed lines*), and the total sample (*thick lines*). The solid thin, dashed, and thick lines represent their underlying mean density profiles, respectively.

which contribute an extra modulation in the cluster distribution. However, in any case, the coincidence between the two subsamples is reasonable. And the 3-D study of §6.2 and §6.4 imply the later might be the main cause.

6.2 The spatial three-point correlation functions of $R \geq 1$ Abell clusters — based on the estimated redshifts

We have also estimated the spatial three-point correlation functions for $R \geq 1$ Abell clusters. The samples are same as those used in the last section. Since there are only 25% clusters having measured redshift, we use the estimated redshift based on the magnitude-redshift relation (kindly available to us by Y.Gao). The accuracy of his redshift estimates is $\sigma \log_{10} Z \approx 0.1$. We are fully aware that the accuracy is not good enough to arrive at a definite conclusion about spatial correlation functions, which have to await the of a large redshift sample. The main purpose of doing so is only to test and, if possible, to confirm the results of the last subsection.

The redshift selection functions are obtained by examining the spatial density distributions, which are plotted in Figure 6.4 for the three samples. The smooth lines are reasonably taken as their selection functions. We have tested the sensitivity of ζ and Q to redshift selection function and found the effect is weak.

The distances to clusters are calculated in the same way as in §5.2, and the galactic extinction effect is corrected as in §6.1. We used the method of §6.1 to estimate ζ, so we will not repeat the details.

As in the last section, we first examine the spatial two-point correlation functions which are plotted in Figure 6.5 for the samples concerned here. The least-squares fits $\xi \propto r^{\gamma}$ to the data of different samples show γ of about -1.2, considerably larger than the standard value -1.8. However, this result is expected because of the errors in estimated redshift, and is consistent with Postman *et al.* (1986) who used the redshift estimates of Leir & van den Bergh (1977).

The three-point correlation function of the statistical sample is presented in Figure 6.6. The meanings of symbols in the figure are clear, and are not discussed for any more. The least-squares fits of the power law $\zeta \propto r^{\nu}$ to the statistical data of each bin with fixed u and v give the slopes ν, which are listed in Table 6.3. The mean value of ν is

$$\overline{\nu} = -2.30 \pm 0.68, \tag{6.5}$$

if it is assumed that ν is statistically independent from bin to bin.

The slope ν would be considerably underestimated because the estimated redshifts are used. But it seems that this will not affect our discussions and conclusions much. Our main purpose is to determine whether ζ has a scaling form, and, if it does, how large the constant Q is. If the effect of the redshift estimates on ξ is modeled by $P(r)$, *i.e.*, $\xi_{est} = \xi P(r)$, then the effect on ζ should be $\zeta_{est} = \zeta P(r)^2$ to the first order. Thus the estimated ζ_{est} is

$$\zeta_{est} \approx Q(\xi_{12}\xi_{23} + \xi_{23}\xi_{31} + \xi_{31}\xi_{12})_{est}, \tag{6.6}$$

if the hierarchical form (2.1.7) establishes. Clearly, the equation (6.5) is consistent with the hierarchical assumption (2.1.7).

The Q-values obtained through eq.(6.6) are listed in Table 6.4. The values remain almost constant and have no systematic change with u and v. Its mean value is

$$\overline{Q} = 0.67 \pm 0.17. \tag{6.7}$$

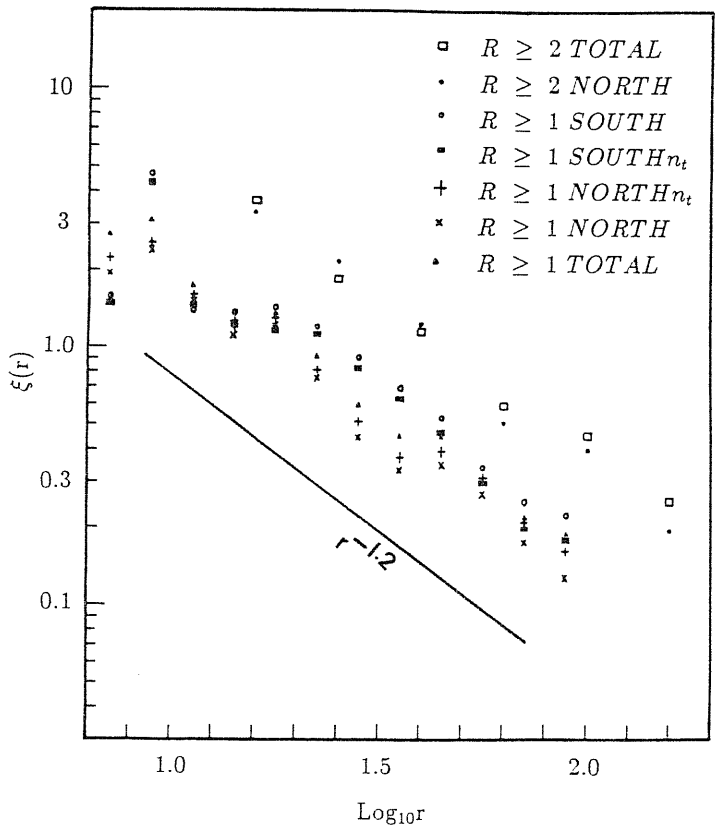

Fig.6.5 — Two-point spatial correlation functions of the statistical sample for different zones, for different redshift selection functions,and for different richness classes (as indicated on the figure).

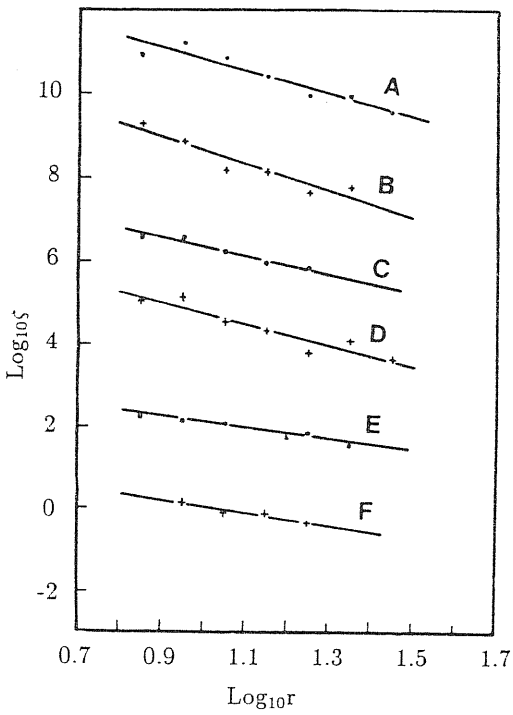

Fig.6.6 — The spatial three-point correlation function of the whole statistical sample. Others are the same as Fig.1.

Table 6.3

THE v-VALUES FOR THE STATISTICAL SAMPLE

	Log u		
v	0.0–02.	0.2–0.4	0.4–0.6
0.0–0.5	−2.73	−3.19	−2.18
0.5–1.0	−2.48	−1.39	−1.54
Mean value	-2.30 ± 0.68		

We noted that the obtained Q is not sensitive to the γ of ξ adopted. Even if we take $\gamma = 1.8$, the mean value now is 0.44 ± 0.12, not different from eq.(6.7) too much(see also Table 6.4).

Our separate analyses of the northern and southern samples are consistent with the analysis of the whole sample, and I omit the figures here. The values of Q given by the power-law fits, however, are also listed in Table 4. The mean values of Q are 0.87 ± 0.29 for northern clusters and 0.68 ± 0.15 for the southern clusters, both in agreement with the estimation of the whole sample.

Now we check the consistency between the angular and spatial three-point correlation functions. Using the Limber equation (2.1.9) and the selection function of Figure 6.4, we find $q/Q = 1.1$. Evidently, the angular and spatial analyses are consistent[see eqs.(6.6) &

Table 6.4

THE Q-VALUES FOR THREE SAMPLES[a]

SAMPLE	v	Log u 0.0–02	0.2–0.4	0.4–0.6
All	0.0–0.5	0.691	0.760	0.833
		0.376	0.477	0.626
	0.5–1.0	0.723	0.398	0.564
		0.419	0.253	0.473
Mean value		0.670 ± 0.168		
		0.437 ± 0.124		
North	0.0–0.5	1.007	0.845	0.947
		0.488	0.543	0.599
	0.5–1.0	0.742	0.411	1.263
		0.440	0.275	1.256
Mean values		0.869 ± 0.285		
		0.599 ± 0.337		
South	0.0–0.5	0.834	0.642	0.659
		0.543	0.505	0.465
	0.5–1.0	0.817	0.715	0.426
		0.493	0.560	0.349
Mean value		0.682 ± 0.148		
		0.486 ± 0.075		

[a] For each (u, v) bin, two Q-values are given. Upper data are from $r^{-2.4}$ fits, and lower data are from $r^{-3.6}$ fits.

(6.7)].

6.3 The three-point correlation functions of $R \geq 2$ clusters and Q independence on their richness

The correlation-richness dependence is very useful in constraining theories of galaxy formation. Concerning the three-point correlation functions, it is natural to ask how they depend on the richness of clusters. In order to answer such a question, we estimate the three-point correlation functions for $R \geq 2$ clusters in what follows.

In the whole statistical sample, there are 445 clusters with richness $R \geq 2$, of which 266 are distributed in the northern hemisphere. Three-point angular, as well as spatial, correlation functions are estimated for two samples: sample SN2, including all northern $R \geq 2$ clusters; and sample SW2 of all $R \geq 2$ clusters. No statistics have been done for the southern cluster subsample alone because of the relatively fewer clusters included. The same techniques as used in the last two sections are applied in calculating ζ and z, except that 3 times more random clusters than the observed ones are produced as a comparison catalog, and the larger interval separations of r and θ, $\Delta \log_{10} r = \Delta \log_{10} \theta = 0.2$ are adopted in order to minimize the random fluctuations due to the smaller number of clusters included and to improve the accuracy of estimation of z and ζ. The ranges of triplets are set to $0.8^\circ \leq \theta \leq \theta_{31} \leq 10^\circ$ or $15 \leq r \leq r_{31} \leq 250h^{-1}$Mpc.

The redshift selection functions are obtained by examining the density distributions, but here we omit the plot. As in the case of $R \geq 1$ clusters, the two-point correlation functions, which have already been shown in Figures 6.2 and 6.6, are estimated. The least-squares analysis techniques show that the slopes for both samples are all very close to -0.9 and -1.2(with differences less than 10%), respectively, just as $R \geq 1$ clusters.

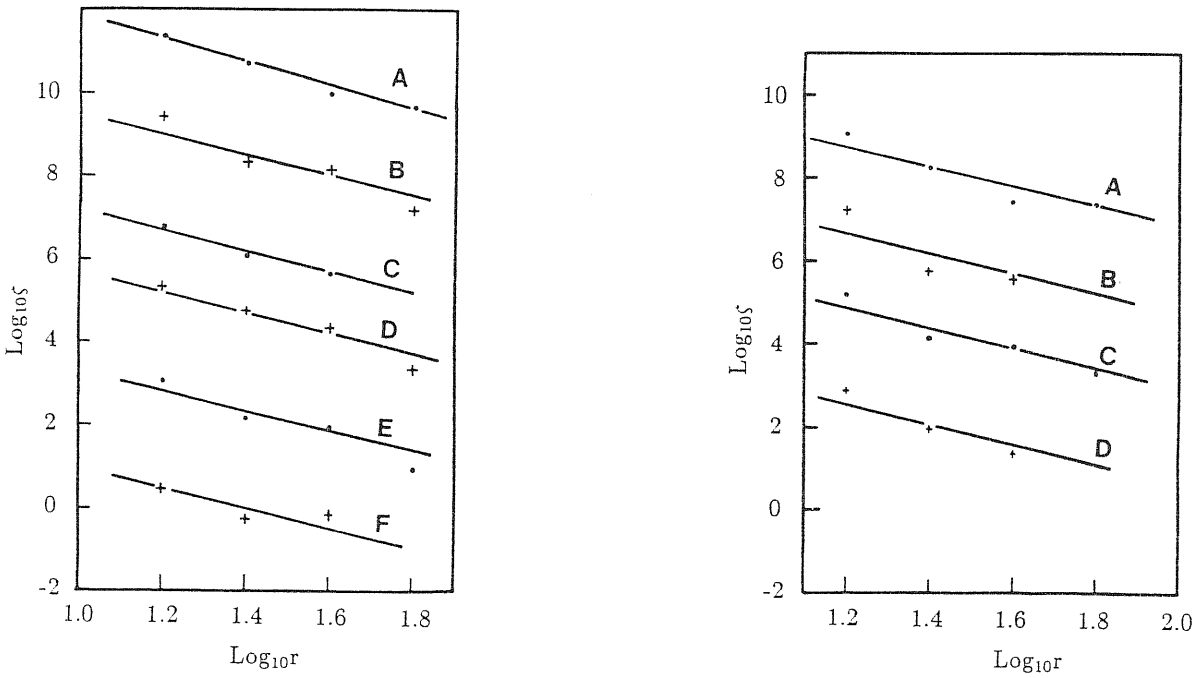

Fig.6.7 — Three-point spatial correlation functions of (a) the northern $R \geq 2$ sample and (b) the total $R \geq 2$ sample. The upper case letters and vertical shfit factors of (a) correspond to those in Table 6.4 and of (b) to Table 6.5.

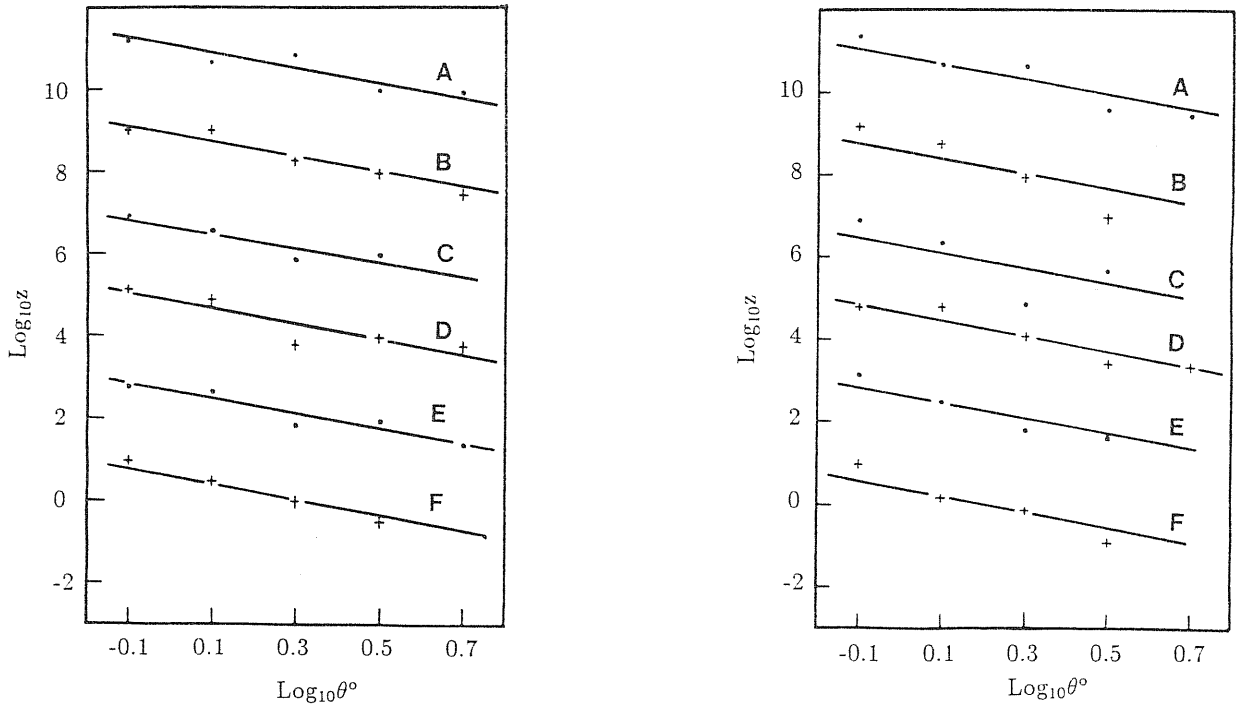

Fig.6.8 — Three-point angualr correlation functions of (a) the northern $R \geq 2$ sample and (b) the total $R \geq 2$ sample. Others are same as Fig.6.3.

Table 6.5

THE Q-VALUES OF $R \geq 2$ CLUSTERS[a]

SAMPLE	v	Log u 0.0–0.2	0.2–0.4	0.4–0.6
All	0.0–0.5	A $\times 10^8$	B $\times 10^6$	
		0.24	0.38	
		0.18	0.28	
	0.5–1.0	C $\times 10^4$	D $\times 10^2$	
		0.42	0.33	
		0.25	0.25	
Mean value		0.34 ± 0.07		
		0.24 ± 0.04		
North	0.0–0.5	0.73	0.92	0.80
		0.54	0.90	0.76
	0.5–1.0	0.85	0.65	0.57
		0.66	0.66	0.57
Mean value		0.75 ± 0.13		
		0.86 ± 0.13		

[a] See note to Table 4.

Table 6.6

THE q-VALUES OF $R \geq 2$ CLUSTERS

SAMPLE	v	Log u 0.0–0.2	0.2–0.4	0.4–0.6
All	0.0–0.5	0.52	0.40	0.35
	0.5–1.0	0.32	0.49	0.44
Mean value		0.42 ± 0.08		
North	0.0–0.5	0.74	0.75	0.78
	0.5–1.0	0.51	0.52	0.68
Mean value		0.66 ± 0.12		

Figures 6.7 and 6.8 show our estimated ζ and z for the $R \geq 2$ cluster samples. It's evident that the three-point correlation function of $R \geq 2$ clusters is much larger than that of $R \geq 1$ clusters. To give a quantitative comparison with $R \geq 1$ clusters, we use the hierarchical forms (eqs.[3.1.7] & [3.1.8]) with $\xi \propto r^{-1.2}$ and $\omega \propto \theta^{-0.9}$ to fit the estimated results. The straight lines in the figures represent these fits. We can be sure, from the figures, that the hierarchical form are consistent with the data. The Q- and q-values thus obtained are given in Tables 6.5 and 6.6. As in the last section, we also estimate the Q taking $\xi \propto r^{-1.8}$(see Table 6.5).

If we note $q/Q = 1.1$ according to the Limber equation, we would find that our angular and spatial results are in good agreement. The Q values of the SN2 sample are very close to those of $R \geq 1$ clusters, indicating that Q is richness independent. However, the SW2 sample has a smaller Q value(about a half of $Q_{R\geq 1}$). The discrepancy is not well understood. According to our check of $< DDD >$, $< DDR >$, and $< RRR >$, we find there are relatively fewer triplets in the southern sky (so the samples may not be 'fair').

Only if we note the existing sampling error and also the fact that ζ is ten times stronger than that of $R \geq 1$ clusters, we would think that Q is almost richness independent even concerning the sample SW2.

6.4 An analysis of a small redshift complete sample

All the above results are based on the 2-D samples. Even in the 3-D studies, redshift is estimated by the magnitude-redshift relation. In this section, I present our recent analysis of a small sample which is almost redshift complete. The results obviously complement the previous sections.

6.4.1 The sample and the method

The data we use are from the ACO catalog of rich clusters of galaxies. In what follows, we shall treat the north and the south separately. As for the north sample, we select those clusters with $\delta \geq -27°$, $|b^{II}| \geq 30°$, richness $R \geq 0$ and the tenth brightest magnitude $m_{10} \leq 16.4$. As a result we have 227 clusters. For 212 of them the redshifts are measured.

As for the southern hemisphere, the ACO catalog is complete for $\delta \leq -17°$. We select only those clusters with $m_{10} \leq 16.4$ and $R \geq 0$. The southern sample is built considering all clusters with $b^{II} < -30°$ and $\delta < -17°$. These selection criteria leave us with 103 clusters. We shall be using the estimated redshifts for 44 of them.

For those clusters without redshifts Z, we use the magnitude-redshift relation to estimate Z. For the north sample we adopt the m_{10}-Z of Postman *et al.* (1986) and for the south sample, we follow Couchman *et al.* (1989). Again the galactic obscuration effect is corrected according to eq.(5.3) and redshift selection function is fit to the density distributions.

In this section, we used the moment method to calculate the three-point correlation function. All necessary formulae are given in the Appendix A. The method was thought to be effective in analysing small samples, when we did the work. Recently, from analysing simulations, I found the method is not as effective as initially thought in treating small samples(see §3.1.5 for discussion). In spite of the limitation(*i.e.*, large errors), the results we got are still significant. We are now analysing similar samples by the direct counting method(Plionis, Valdarnini & Jing 1991) which shall complement this section.

6.4.2 Results

We shall report the results obtained on the basis of (3.1.7). North and south sample results will be shown separately. In Table 6.7, we report the intervals $Q - \Delta Q, Q + \Delta Q$ obtained, for different radial shells, according to (A.11) and (A.16). The first column gives the results for the whole north sample, and the second column for the southern sample. The limits chosen to define the shells are 7, 11, 16, 21 , and $26h^{-1}$Mpc. From the table, we find that there is no systematic difference of Q between northern and southern hemispheres from bin to bin, in contrast with the previous 2-D analyses(see §6.1). Especially the mean value of Q for the largest bin 7 — 26 h^{-1}Mpc coincides (~ 0.7) so well for the both samples, which implies that the discrepancy found previously might be due to largely some "bad" Palomer plates and (or) to different project effects, but not due to the different intrinsic clustering properties.

The data of Table 6.7 are also plotted in Figure 6.9 versus r_k for Q. Error bars are the uncertainties quoted in Table 6.7. The continuous line is for the north sample and the

Table 6.6

Estimated Q-values for different shells and samples. The last line shows the errors estimated by the bootstrap method.

	North	South
7—11	0.309 ± 0.073	0.718 ± 0.135
11—16	0.750 ± 0.041	0.268 ± 0.012
16—21	0.453 ± 0.051	0.184 ± 0.011
21—26	0.367 ± 0.020	0.945 ± 0.019
7—26	0.777 ± 0.003	0.702 ± 0.002
bootstrap	0.77 ± 0.35	0.70 ± 0.47

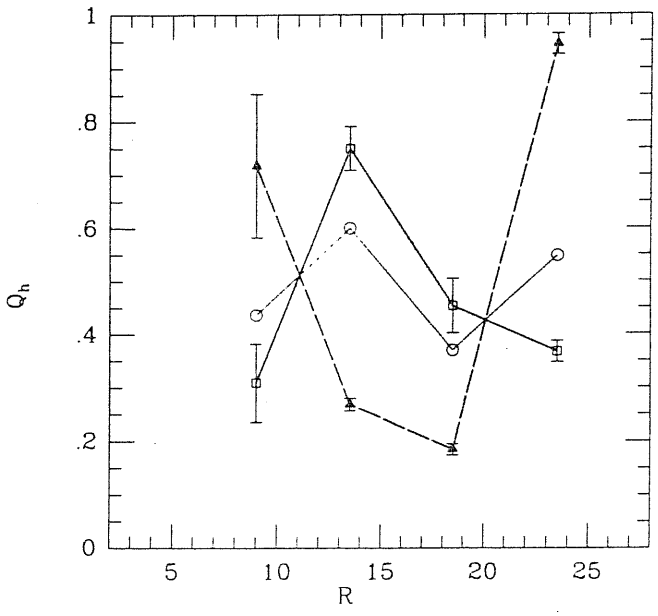

Fig.6.9 — Q for the north (continues line) and the south (dashed line) versus radial distance. The continues (thin) line is an average of this sample and the north one. The plotted points correspond to $(r_k + r_{k-1})/2$. Data are taken from Table 6.6

dashed line for the south one. We also plot an average of the two samples with a weight proportional to their cluster number. The averaged data seem to suggest that Q is nearly constant (0.5) consistent with the previous 2-D studies.

The errors given by (A.16) are quite formal and the actual error would be much larger. However, the *real* error of Q is not easy to obtain. By the bootstrap technique, we found the typical error is ~ 0.35 even for the single bin $7\text{–}26h^{-1}$Mpc. Such a large error may arise partly from the small size of the samples and partly from the waste of possible configurations of the method itself.

In summary, this 3-D study confirms the hierarchical form (2.1.7) as a good approximation to ζ of clusters. The Q values is about 0.7, well consistent with the previous 2-D studies. The discrepancy of Q between the northern and southern samples detected in the 2-D study (see §6.1), is greatly reduced, and the results of the north and south estimates

are marginally consistent within internal errors.

6.5 Discussions and further remarks

It would be interesting to compare ζ of Abell clusters with that of galaxies. As summarized in §3.2.1, the Q of galaxies is ~ 1.3 based on the Zwicky and Lick catalogues, and ~ 0.8 based on the available redshift samples and the ESO/Uppsala catalogue. These values, especially the later one, are nearly same as those of Abell clusters obtained here. This would indicate that from galaxies to $R \geq 2$ clusters, although their three-point correlation functions change by more than 10^3 in amplitude, they possess the same hierarchical form (3.1.7) with the constant $Q \approx 0.7$ independent of the richness of galaxy systems.

This universal hierarchical form is important for galaxy formation theories. For example, in the Gaussian model of biased galaxy formation, Jensen and Szalay (1986) have calculated the three-point correlation function and predicted that the equivalent Q increases with the biasing threshold (*i.e*, richness). However, our results show no such tendency. Moreover, the high amplitude of ξ_{cc} strongly suggests that rich clusters form at the sites of high peaks(Kaiser 1984), and as discussed in §3.2, the high peak approximation predicts (3.2.9) for ζ_{ccc}, apparently contradictory with our results. If there were the cubic term of (3.2.9) in the observational data, it would have manifested in our above analysis at small separations. The independent analysis of Tóth *et al.*(1989), which was designed especially to search for the cubic term, confirmed the lack of this term.

The hierarchical form of ζ_{ccc} at least suggests that the analytical biasing models are unable to describe the distribution of rich clusters. The recent N-body simulation of the biased CDM model (Gott *et al.* 1991), however, reproduced the hierarchical form, and they attributed the lack of cubic term to the merge effect of nearby high peaks. Their results thus indicate that the analytical prescriptions are too simple and the biasing schemes can explain the distribution of clusters if the nonlinear or merge effects are taken into account.

I noted two problems which should be further explored. 1.) Gott *et al.*(1991) have run three sets of simulation and chosen only one. *Are their results general?*. Since there are large fluctuations in the simulations(see their paper), more simulations are needed to give affirmative conclusions. 2.) The merge effect should be effective only on the small separations. An analysis of ζ_{ccc} *only on large separations*, can tell us whether the biasing model works without running large N-body simulations. The work in these directions are in progress.

Since conventional models fail to reproduce the ξ_{cc}, an alternative — explosion model of galaxy formation, is explored and is found to have a strong cluster-cluster correlation function (*e.g.* Weinberg *et al.* 1989). I found that in this scenario, the hierarchical form can be reproduced, nearly independent of model details(see next chapter).

‡The materials presented in this chapter are based on our two papers: Jing, Y.P. & Zhang, J.L. 1989, *The Astrophysical Journal*, **342**, 639; Jing, Y.P. & Valdarnini, R. 1991, *Astronomy and Astrophysics*, (in press). The discussion of the last section is updated.

7

Three-point functions of clusters in the bubble Universe

The spatial distributions of clusters of galaxies provide us with good opportunities of testing current theories of galaxy formation. In this chapter, by assuming that the Universe is filled with bubbles and clusters form at sites where three bubbles intersect(*i.e.* toy models of the Ostriker explosion scenario), we demonstrate the types of three-point correlation function ζ of clusters, that are predicted, thus testing the bubble models by comparing them with that of observed cluster catalogs.

7.1 Introduction

While several possible models(such as the biasing model, the cosmic string picture) have been proposed to explain the two-point function of clusters (and other observational effects), how to naturally reproduce ξ still remains a great puzzle for cosmologists(e.g, Kaiser, 1984; White et al., 1987; Turok, 1985; Jing & Zhang, 1987; see §3.2 & §5.1). Another interesting approach to the problem was recently proposed: galaxies are distributed on shells and clusters form at the intersections of shells(Bahcall, 1988a; Ostriker, 1988; and Dekel, 1988). This was actually predicted by the explosion theory of galaxy formation(Ostriker and Cowie, 1981; Ikeuchi, 1981), and is inferred from the recent observations of large bubbles in the redshift slice surveys(de Lapparent et al., 1986; hereafter LGH; Geller and Huchra, 1989). In the explosion scenario, early explosions at redshift $z \sim 10$ swept their surrounding primordial gas into hot, dense shells, and galaxies form when the shells cool and fragment(Ostriker and Cowie, 1981). The detailed dynamical N-body simulations(Weinberg et al., 1990) show further that clusters form preferentially at sites of shell intersections, in accordance with the observations of redshift slice surveys(LGH). Although it still remains uncertain to which physical processes are responsible for the initial explosions of such high energies, there exist several physical candidate mechanisms: explosions of supermassive stars and of supernovae, electromagnetic radiations of superconducting cosmic strings, etc.(Carr et al., 1984; Ostriker and Cowie, 1981; and Ostriker et al., 1987).

Weinberg, Ostriker and Dekel(1989, hereafter WOD) have made detailed numerical simulations to study spatial distributions of clusters, by identifying clusters as "knots" where three shells intersect(see also a similar discussion of Bahcall et al., 1989). In their simulations, shells have spherical geometry, with constant radius R or power law distribution of radius $P(R) \propto R^{\beta}$. They considered various effects, such as the dynamical and observational mergers of clusters, the shell mergers, etc., and included these effects in their simulation by some hand-input criteria. By adopting the mass recipe that cluster mass M_{cl} is proportional to the product of the three shell radii, i.e., $M_{cl} \propto R_1 R_2 R_3$ (based on the N-body simulations of Weinberg et al., 1990 and on the reasonable theoretical arguments), they obtained the mass function of clusters. By assuming the mass-to-light ratio remains a constant for clusters, they used luminosity function(LF) of clusters(Bahcall, 1979) to constraint the possible model parameters. They also studied the two-point function of

clusters and its richness dependence(Bahcall, 1988b). Finally they found that if they take appropriate values for the model parameters, e.g., $\beta \sim -4$ and the filling factor(its definition given below) $f \sim 0.3$, the model can produce the right LF of clusters, right trend of correlation-richness dependence, right slope of ξ, but too high a correlation amplitude when distance scaled to the mean separation of Abell clusters which could be acceptable only at 2σ level(however, see Bahcall et al., 1989). The overclustering problem might be relaxed if only certain fraction of "knots"(not dependent of M_{cl}) actually succeed in producing Abell clusters and (or) if there is a random component of clusters which uniformly distribute in space and have the similar mass distribution.

It would be very interesting to use the three-point function of clusters ζ to further test the bubble model. In the following sections, I shall present the predictions of ζ in various bubble models. §7.2 & §7.3 respectively study the two simplest models: 1) The radii of shells are assumed to be a constant (hereafter constant model); and 2) Shells have a power law radius distribution, n(R) $\propto$ R^{β} (hereafter power law model). The motivation to study these two cases has threefold. First, these two models perhaps could be solved analytically, like Kulsrud and Cowley (1989, hereafter KC) for the two-point correlation function. The simulation can help to test such an analysis. Secondly, the simulation can give some features such as the scales where three clusters correlates, which would remain valid in more realistic models. Finally, due to large differences in the shell radius distributions of the two models, we can find out how three-point correlations depend on the models.

However, the models above might be too simplified. Physically, all shells cannot have the same radius. Even in the power law models, two shells which overlap greatly and essentially sweep the same primordial gas, should be regarded as one shell, thus one of the two shells has actually loses its identity(This is the so-called anticorrelation effect of shells or shell mergers in WOD). Another important effect is cluster mergers: two primeval clusters of small separation would evolve dynamically into, or would be later observationally identified as one cluster. §7.4 studies ζ in the power law models by including these effects. In order to distinguish ones with the pure power law models of §7.3, we call them the modified power law models.

7.2. Equal-size shells

In this section, we study the three-point correlation functions of clusters intersected by equal-size shells. As KC and WOD showed, this model is completely fixed by two parameters: the shell radius R and the filling factor $f = (4\pi/3)n_{sh}R^3$, where n_{sh} is the spatial density of shells. KC obtained analytically the mean density n_{cl} of clusters

$$n_{cl} = \frac{9\pi}{16} f^3 R^{-3}, \tag{7.1}$$

and the cluster-cluster two-point correlation function ξ_{cl}:

$$\xi_{cl}(y) = \frac{3}{4f}\frac{1}{y} + \frac{1}{\pi^2 f^2}\frac{(1-y^2)(1+3y^2)}{y^2} + \frac{1}{3\pi^2 f^3}\frac{(1-y^2)^2}{y} \tag{7.2}$$

where y $\equiv r/2R$. Note: we can easily find a minor error (a factor 2 in the numerator of the second term) in the expression ξ_{cl}(y) of KC; this has been corrected in Eq.(7.2). This expression has already been verified by the numerical experiment of WOD.

The method of our simulation is somewhat different from that of WOD. We adopt $f = 0.4$, 0.6and 0.8 for the filling factor. We choose a spherical space of radius R_{sim} for the simulation. R_{sim} is determined by the condition that for $f = 0.4$, there are 1000 clusters produced in one realization[see Eq.(7.1)]. Considering the boundary effect of the simulation space(i.e. clusters could be formed by intersections of the inner shells and the shells whose centers just lie out of the space), we in fact first randomly place (centers of) shells in a larger sphere of radius $R_{sim} + R$, and find out all knots (clusters) where three shells intersect. Then we include all those clusters within the sphere of R_{sim} in our later calculation, thus correcting the boundary effect. The same simulation space is used for $f = 0.6$ and $f = 0.8$ models. Certainly there would be $(0.6/0.4)^3 \times 1000 \simeq 3400$ and $(0.8/0.4)^3 \times 1000 = 8000$ clusters produced in one realization of $f = 0.6$ and of $f = 0.8$. Because the computational cost is rapidly increased with N_{cl} ($\propto N_{cl}^3$) in calculating ζ, we will randomly choose 1000 clusters (hereafter "child" sample) in each realization of $f = 0.6$ and $f = 0.8$ models for our calculation. It is easy to prove that the "child"sample has all the same N-point correlation functions as its "parent" sample, that is, all intrinsic clustering properties will remain. This argument is similar to that of the sparse sampling of a redshift survey (Kaiser 1986; Metcalfe, *et al.* 1989). Why we don't take a smaller simulation volume for $f = 0.6$ and $f = 0.8$ is for the "fair" sample reason. As we show below that the three-point correlation functions remain positive out to 4R (the largest side of a triangle), and as R_{sim} we now take is $R_{sim} = 12.8R$, reducing sample volume would probably influence the final results. This method has been verified when we checked the two-point correlation functions of the above three f cases, which reproduced the data of WOD and was completely consistent with the expression (7.2). [see also §7.3]. For each model, we make ten realizations.

The procedure of estimating three-point correlation function is same as Jing and Zhang (1989; see §6.1). In Fig.7.1, we illustrate the three-point correlation functions ζ of several typical (u, v) bins for the $f = 0.4$ model. Figure 7.1(a) shows the four cases with the fixed $v = 0.05$ but different u, which covers equilateral triangles to highly elongated atute isosceles ones. We can find that three clusters are strongly correlated on small scales and ζ remains positive out to $r < 2R$ and $(u + v)r \simeq ur \simeq 2R$. Figure 7.1($b$) represents the other four cases with fixed $u \simeq 1.1$ but different v, which includes approximate equilateral triangles to highly oblated obtuse isosceles ones. Again high three-point correlations are found on small scales. However, all ζ start vanish at $r \simeq ur \simeq 2R$. This means ζ could remain positive out to $r_{31} = (u + v)r$, which is about $4R$ for $v = 0.85$. We can conclude that there are strong three-point correlations in triangles of two smaller sides r_{12}, $r_{23} \leq 2R$ and of the longest $r_{31} \leq 4R$. We have also checked ζ for the $f = 0.6$ and $f = 0.8$ models. The three-point clustering behaviours of these two models is very similar to that of $f = 0.4$ model, and we omit the corresponding figures here.

This phenomenon can be easily explained by a sketch map(Fig.7.2, taken from KC). It illustrates the all four configurations of producing two clusters(P, Q). If a third cluster formed by three other shells(no one belongs to the shells of Fig.7.2), and the first two clusters are produced by Fig.7.2d, such triplets contribute to the first term of Eq.(3.1.3). If the first two clusters are formed by either case of Figs. 7.2a, 7.2b and 7.2c, and the third cluster formed by the three independent shells, or if a third cluster formed on either

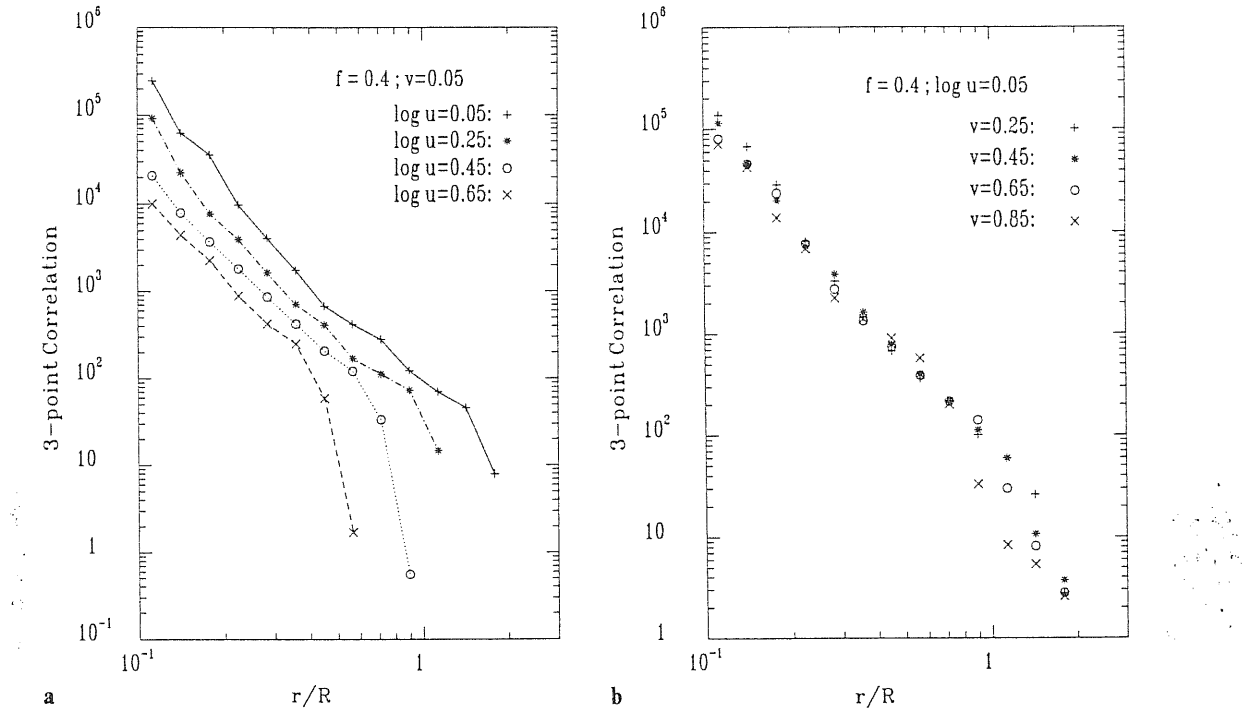

Fig.7.1 — The three-point correlation functions of the $f = 0.4$ constant model in eight typical (u, v)-bins. (a) for the fixed $v = 0.05$; (b) for the fixed $u \simeq 1.1$.

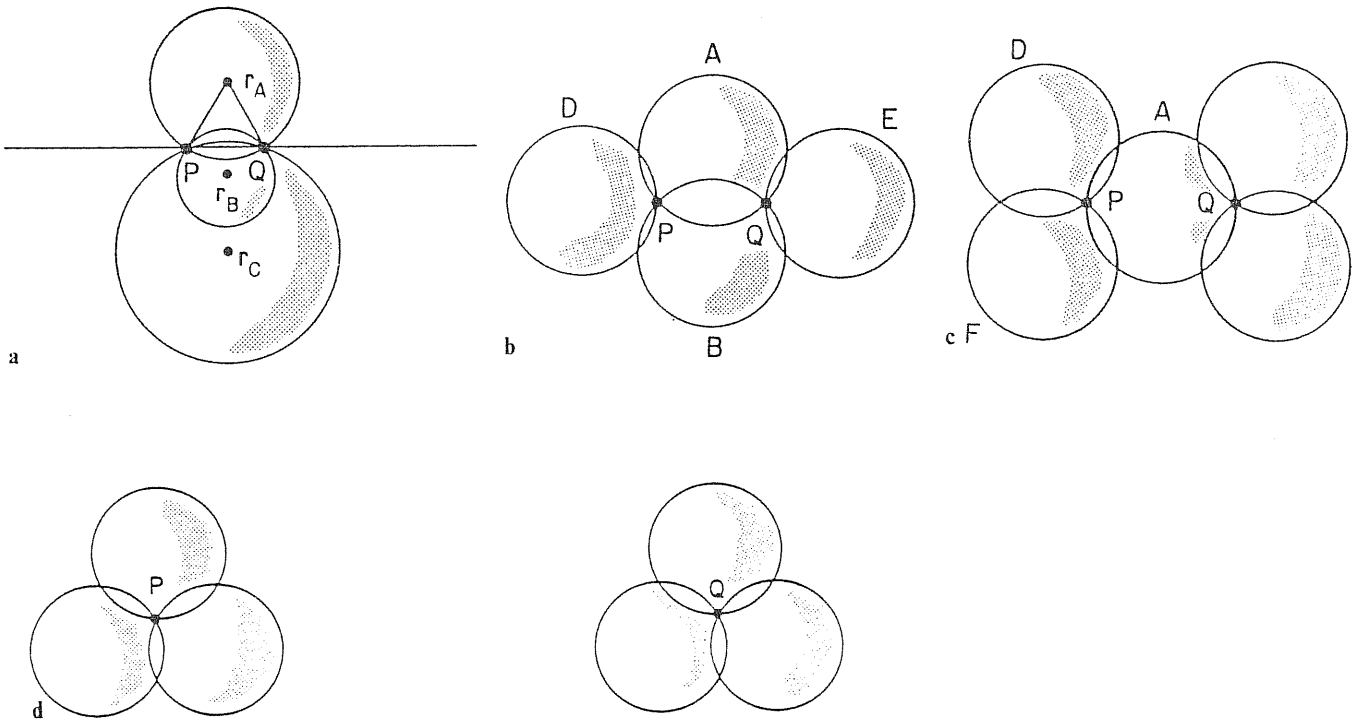

Fig.7.2 — The configurations of shells which produce two clusters. (a) Three common shells; (b) Two common shells; (c) One common shells; (d) All shells are different. This figure is taken from Kulsrud and Cowley (1989)

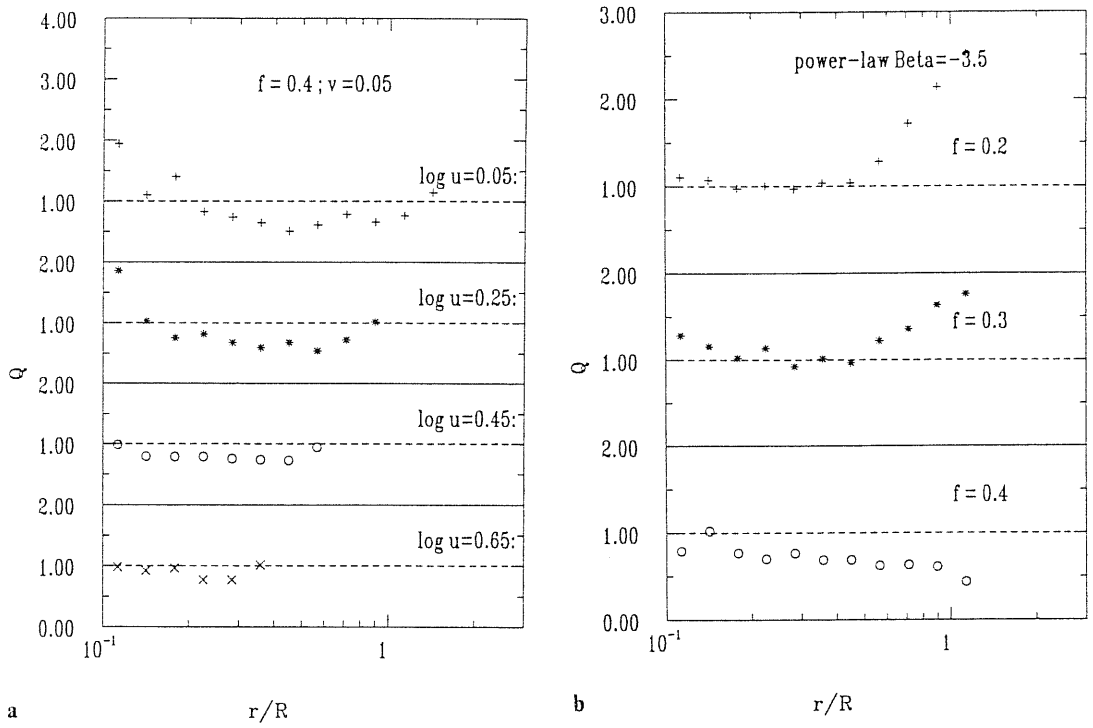

Fig.7.3 — The scaled three-point correlation functions Q [see equ.(3.1.7)] of the $f = 0.4$ model. (a) corresponds to Fig. 1a; and (b) to Fig. 1b

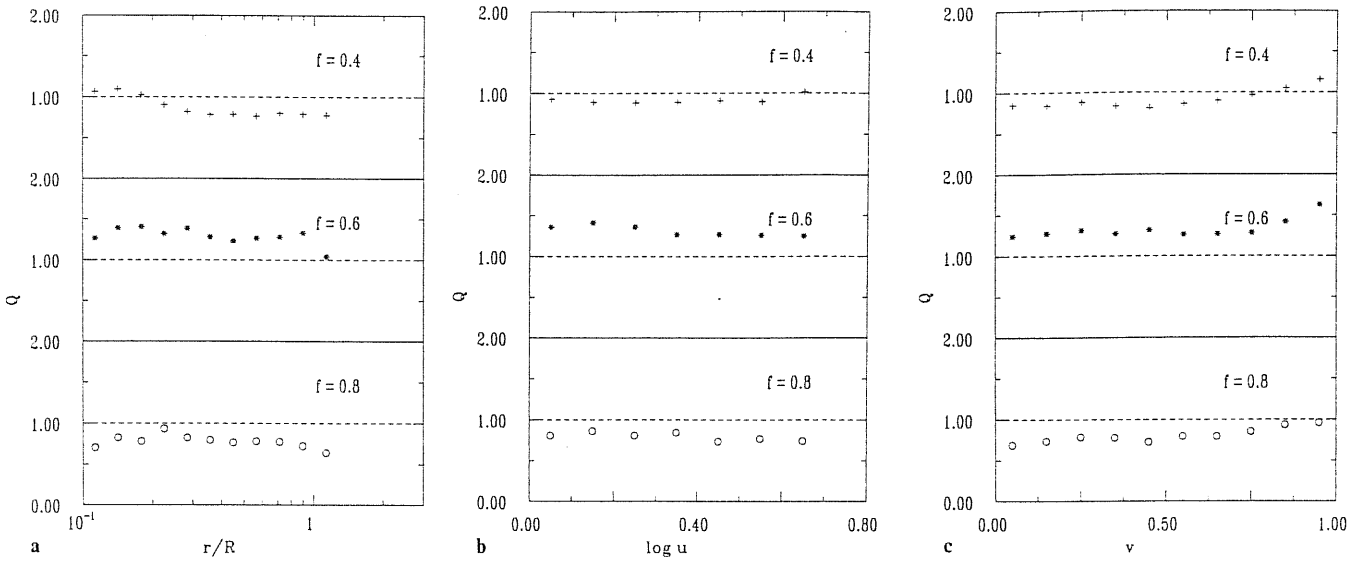

Fig.7.4 — The mean values of Q for the three constant models of different f. (a) The average values of Q over all triplets with the fixed r; (b) The average values of Q over all triplets with the fixed u; (c) The average values of Q over all triplets with the fixed v.

shell of Fig.7.2d and the first two clusters are P, Q of Fig.7.2d, such triplets contribute to the three ξ-terms of Eq.(3.1.3). It is only when a third cluster S is formed on shells of

Fig. 7.2a, 7.2b or 7.2c (*i.e.*, at least one common shell forming S, and P or (and) Q) that triplets PQS would contribute to the reduced three-point correlation term of Eq.(3.1.3). It is easy to see that such triplets PQS always have two sides smaller than 2R and the longest side less than 4R.

In order for comparing with the observations, it is convenient to use Q(r,u,v):

$$Q(r,u,v) = \frac{\zeta(r,u,v)}{\xi(r)\xi(ur) + \xi(ur)\xi((u+v)r) + \xi((u+v)r)\xi(r)} \tag{7.3}$$

that is the three-point correlation function scaled to the products of two-point correlation functions. The previous observational studies of Abell clusters show that Q is a constant between 0.5 and 1.1 (see Chapter 6). The amplitude of Q(r,u,v) and its r-, u- and v-dependences could be used to test the models.

In Fig.7.3, we show the scaled three-point correlation functions Q of Fig.7.1. Most of Q fall in the range between 0.5 and 1.1. This is very encouraging. Q depends on u very weekly, and the average values of different u-bins remain almost a constant(see Fig.7.3a), although ζ for different u have very different magnitudes(Fig.7.1a). Similarly, Q also have a very week v-dependence(Fig.7.3b). For r from 0.1R to 2R, ζ changes by four magnitudes, whereas Q varies very slightly(within a factor of 2).

To study the r-, u- and v-dependences of Q more detailedly, we separately study each dependence as Groth and Peebles(1977). Fig.7.4a presents the arithmetic averages of $Q(r,u,v)$ over all (u,v) bins for the three different f models. Here and below we average Q over all triangles of three sides less than $2R$. It is only for the reason that the two-point correlation function vanishes at $r > 2R$. From the figure, we find that Q of all three models depends on r very weakly, and could be regarded as a constant with a high precision($\sim$ 15%). In Fig.7.4b, we plot the arithmetic averages of Q over (r,v)-bins. For different u, Q changes very slightly for three models, and again could be considered as a constant for each model. Fig.7.4c shows the averages of Q over all (r,u)-bins. Although Q depends on v again very weakly, we can easily find a minor systematic variation: all models remain a constant at $v \leq 0.7$, however rise slightly with v at the larger v.

In conclusion of this section, although the models taken here are the simplest possible ones of the explosion scenario, the results are encouraging: the observed scaling relation (3.1.7) can be easily reproduced in these models. The slight dependences of Q on r, u, and v may exist, but ζ of the models indeed could be expressed by the hierarchical form (3.1.7) with a high precision. The mean Q values are about 0.9 (for f = 0.4), and 0.8 (f = 0.8), comparable favorably to the observed value $Q_{abs} = 0.8 \pm 0.3$; while Q of the f = 0.6 model is about 1.3, which could be accepted within the 2σ level. Now we are unclear what leads to the slight variation of Q with f. It might be the real feature of the model, or be caused by statistical fluctuations in the simulations.

7.3 Power-law radius distributions

In this section, we study the models, in which the radii of shells are distributed in power laws. We assume that the mean density of shells with radius $R_1 \sim R_1 + dR_1$ is

$$n(R_1)dR_1 = n_o(R_1/R)^\beta dR_1, \tag{7.4}$$

where R is the maximum radius of shells. As WOD pointed out, $\beta \simeq -4$ is of most interest, and also as their simulations have shown that such β could reproduce the mass function of Abell clusters well, we will adopt $\beta = -3.5$ and -4.5 here. Because the number of shells in a definite volume will diverge at $\beta \leq -4$, we must put the lower radius cutoff. The radius of shells will be limited to $R/4 \leq R_1 \leq R$.

We adopt the notations of KC. Let $n_l \equiv \int_l^\infty n(R_1)dR_1$, $a_l^2 \equiv \frac{1}{n_l}\int_l^\infty n(R_1)R_1^2 dR_1$, $\overline{n} = n_l\mid_{l=0}$, $a^2 = a_l^2\mid_{l=0}$, and the effective filling factor: $f = \frac{4\pi}{3}a^3\overline{n}$. Then the cluster density is (KC)

$$n_{cl} = \frac{9\pi}{16}f^3 a^{-3}. \tag{7.5}$$

The method of simulation is similar to that of the constant models. For each β, we choose three f values: 0.2, 0.3 and 0.4. The simulation space is still taken to be a spherical volume. However, its radius R_{sim} is chosen by the condition that there are 1000 clusters [cf Eq.(7.5)] in each realization of f = 0.2 models. Now $R_{sim} = 9.2R$ for the $\beta = -4.5$ model, and $R_{sim} = 10.3R$ for $\beta = -3.5$. As only triplets of sides less 2R are considered below, this simulation space, we think, is already large enough. Again in order to correct the boundary effects, we first randomly place (centers of) shells in the sphere of radius $R_{sim} + R$ for each (f, β) model, under the condition that shells have the power law distribution (7.4). Then we find out all "knots"(clusters) where three shells intersect, and include only those clusters which are in the sphere of R_{sim} in our later calculation of correlation functions. Other procedures are same as §7.2, and we need not repeat them.

KC have analytically obtained the two-point correlation function and the mass function for the power law models. In Fig.7.5, we plotted the two-point correlation functions estimated by our simulations. Due to the domination of numbers of small shells, ξ at small scale has very alike behaviours of the constant models, and could be represented by a power law(the index is about -2). At the larger scale, ξ falls more rapidly than the constant models. The turning point appears at $r \sim 0.5R$, which could be expected because the radius of the smallest shell is 0.25R. The analytical results of KC are plotted in the figure for comparison. We find that the data of simulations are fitted very well by the analytical formulae of KC. In Fig.7.6, we show the mass function of clusters obtained from our simulations. Here we adopt the mass recipe of WOD that the mass of a cluster is proportional to the product of the three shell radii,that is $M = KR_1R_2R_3$. In the figure, cluster masses are in unit of $M_{max} = KR^3$, and the mass functions are in unit of $M_{max}^{-1}R^{-3}$. The smooth lines are the analytical results of KC, which fits the simulations very well. The consistency between the analytical and the simulation results proves the work of KC as well as our simulation methods correct.

Now we calculate the three-point correlation functions for the models. We have not plotted ζ for several selected (u,v)-bins as Fig.7.1 and Fig.7.3, because they can't reveal anything new, except they reconfirm that strong three-point correlations exist in triplets with two smaller sides less 2R and the longest side less 4R. Instead we present the means of Q. Fig.7.7 shows the averages of Q with the fixed r over all configurations. Q remains almost a constant about 1 at $r \leq 0.5R$. However at larger scales, Q of f = 0.2 and 0.3 models rises by a factor of 1 or 2, while Q of f = 0.4 models falls by a factor of 0.5 or 1. Because the contributions to the small scales are dominated by small shells, a constant Q

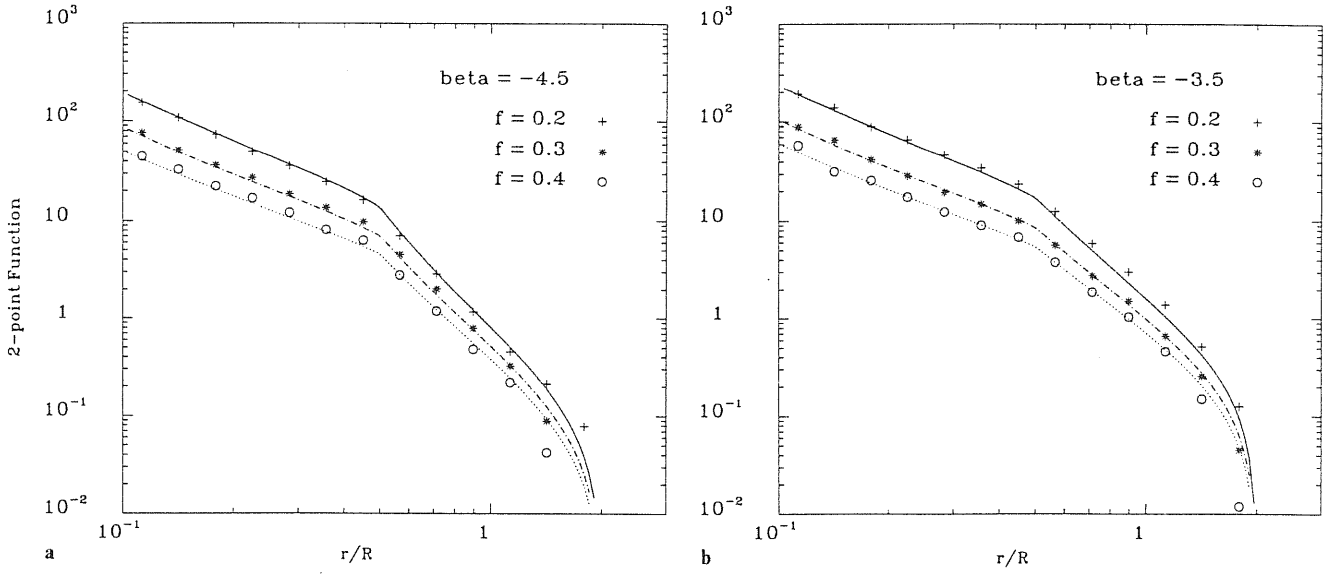

Fig.7.5 — (a) The two-point correlation functions of the $\beta = -4.5$ power-law models with different filling factors. The symbols are the results of the simulations (this paper), and the smooth lines are the analytical results of Kulsrud and Cowley (1989). (b) Same as the 7.5a, but for $\beta = -3.5$

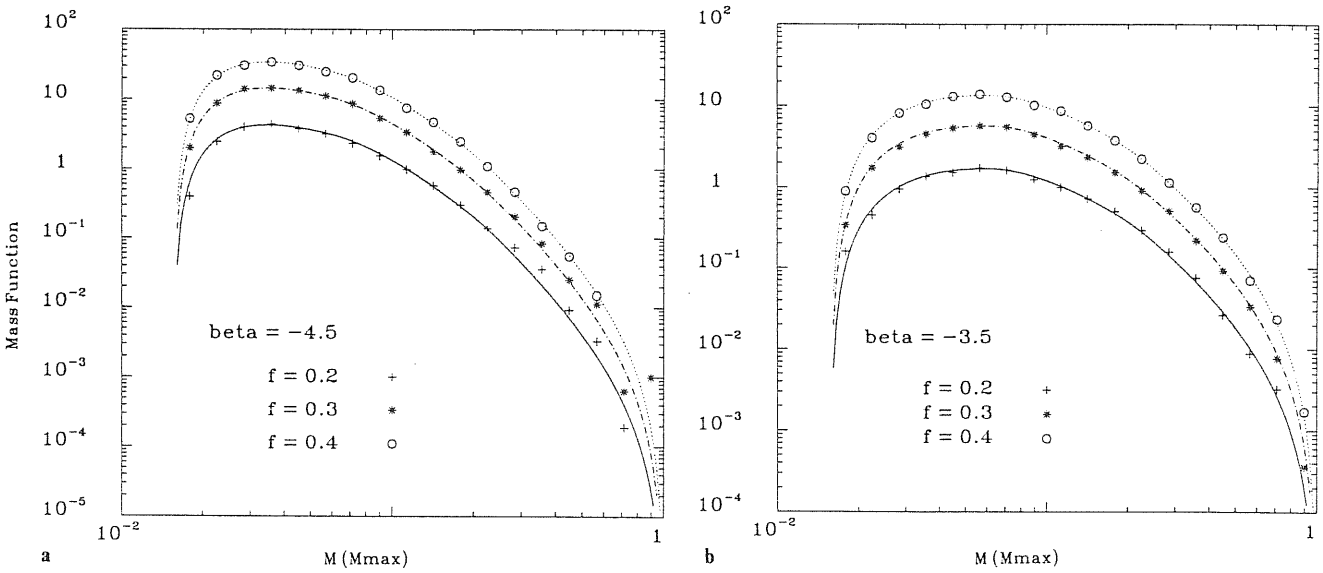

Fig.7.6 — (a) The mass functions of the $\beta = -4.5$ power-law models with different filling factors. The symbols are the results of the simulations (this paper), and the smooth lines are the analytical results of Kulsrud and Cowley (1989). (b) Same as the 7.6a, but for $\beta = -3.5$

could be expected from the last section. The variations of Q at large scale maybe reflects the large range of the shell radii.

In Fig.7.8, we present the averages of Q with the fixed u over all (r,v)-bins. For all

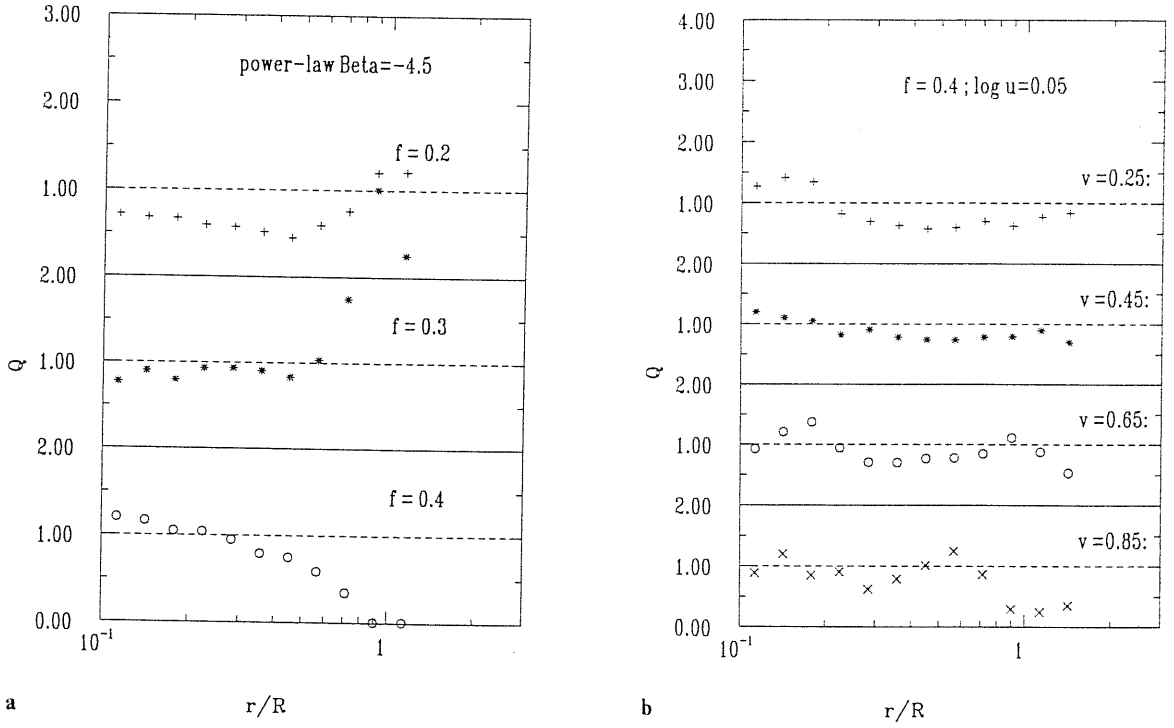

Fig.7.7 — (a) The averages of Q over all triplets with the fixed r for the $\beta = -4.5$ power-law models with different filling factors. — (b) Same as 7.7(a), but for $\beta = -3.5$

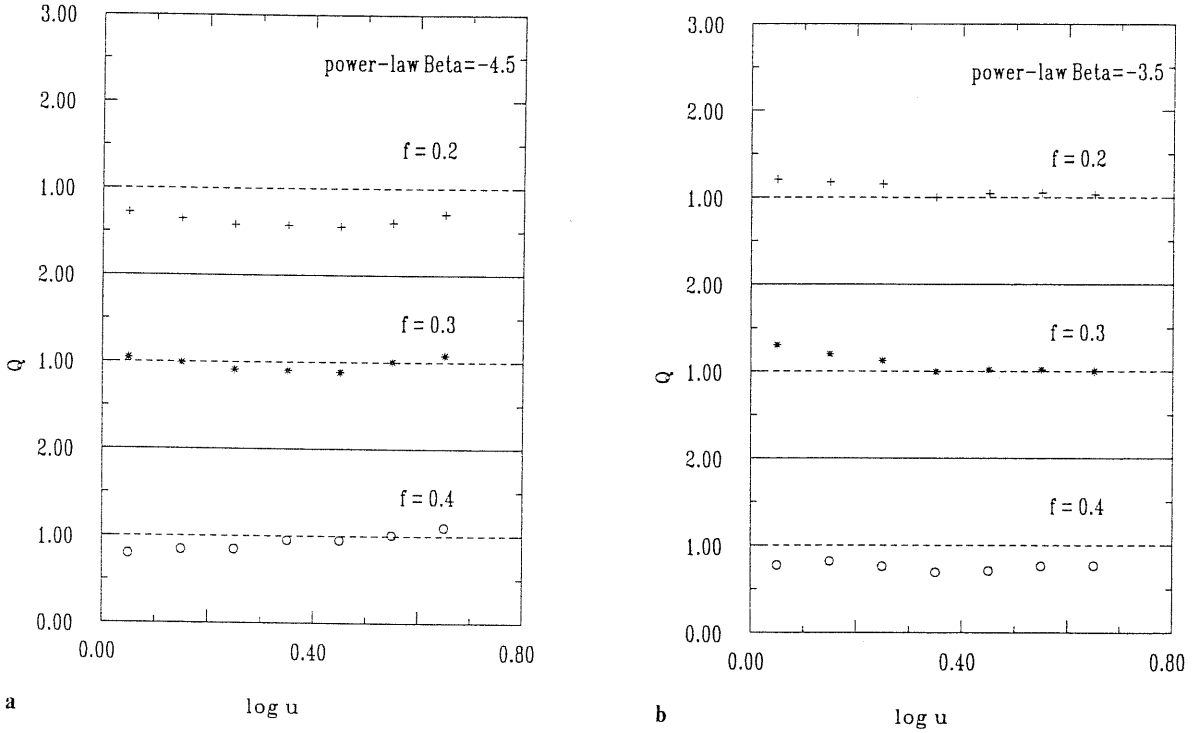

Fig.7.8 — (a) The averages of Q over all triplets with the fixed u for the $\beta = -4.5$ power-law models with different filling factors. (b) Same as 7.8(a), but for $\beta = -3.5$

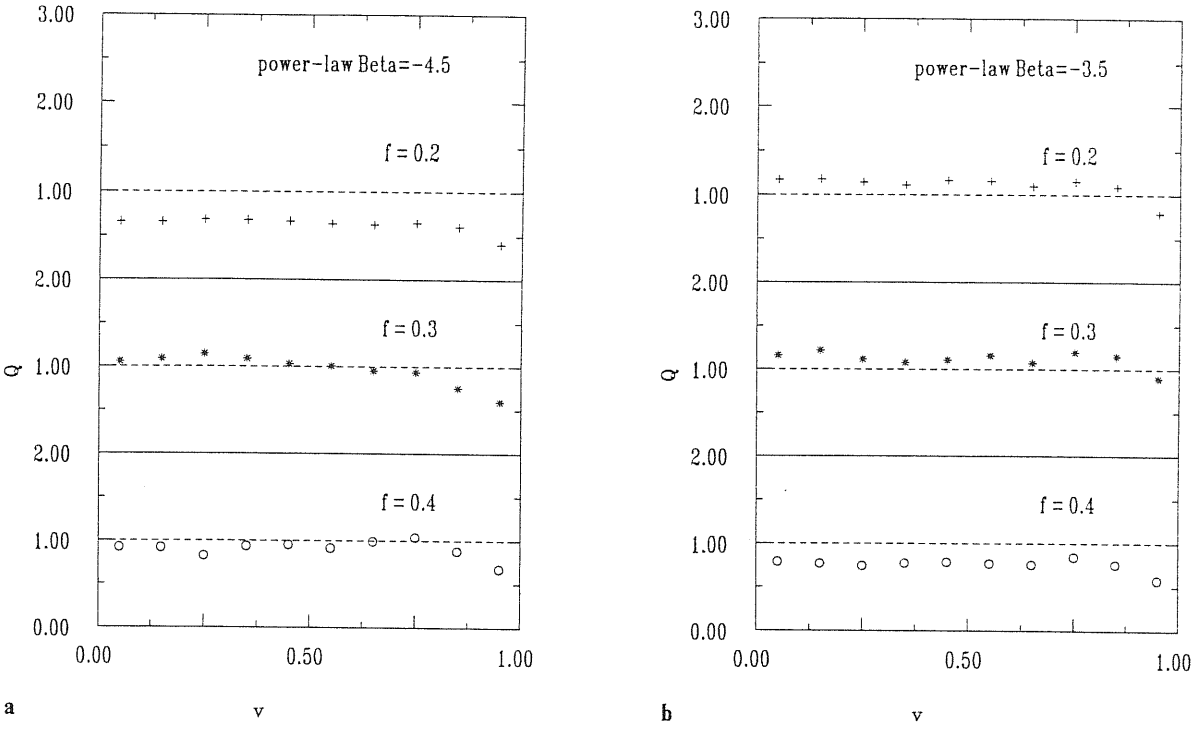

Fig.7.9 — (a) The averages of Q over all triplets with the fixed v for the $\beta = -4.5$ power-law models with different filling factors. (b) Same as 7.9(a), but for $\beta = -3.5$

six (f,β) models, Q depend on u very weakly, and could be regarded well as constants. Fig.7.9 shows the dependence of Q on v. All models have a constant Q at v $\leq$ 0.8, while fall a little at the larger v. We could conclude that Q is almost independent of the shape parameters u and v. The mean values of Q are about 0.7(f = 0.2), 1.0(f = 0.3) and 1.0(f = 0.4) for the $\beta = -4.5$ models, and 1.1(f = 0.2), 1.1(f = 0.3) and 0.8(f = 0.4) for the $\beta = -3.5$ models, so all six models are acceptable within 1σ level by the observation.

7.4 Modified Power Law Models

In contrast with the last section, here we eliminate all shells which are entirely inside larger shells. Because a certain fraction of small shells will lose their identity, we define the filling factor f only with the largest shells $1/2R_{max} < R < R_{max}$, as in WOD. [Note: the meaning of R_{max} is equivalent to that of he R of §7.3 and R is to R_1 there.] The model is completely fixed by three parameters: f, β and R_{max}.

The model is essentially equivalent to the general power law model of WOD, except we take $R_{min} = R_{max}/4$ instead of $R_{max}/8$. Since most of small shells would be eliminated due to lying inside larger shells, and since we are only interested in Abell-like clusters(not smaller clusters or groups), this difference has little influence on our discussion(see also below). So we can directly adopt some results of WOD for our simulation.

From comparison of the theoretical mass function with the observational LF of Abell clusters, WOD concluded that objects which could be identified as Abell clusters should

have mass $M \geq M_*$, and

$$M_* = \begin{cases} 0.14 M_{max}, & \beta = -4.5 \\ 0.23 M_{max}, & \beta = -3.5 \end{cases},$$

and that the mean separation of these objects is

$$\overline{d}_* = \begin{cases} 0.29 R_{max} f^{-1}, & \beta = -4.5 \\ 0.52 R_{max} f^{-1}, & \beta = -3.5 \end{cases}. \tag{7.6}$$

The simulation method is similar to that used in §7.3, but the equation (7.6) is used to fix the simulation volume so as that there are about 1000 clusters of $M \geq M_*$ for $f = 0.2$ in each realization. So for $\beta = -3.5$, $R_{sim} = 15.8 R_{max}$; and for $\beta = -4.5$, $R_{sim} = 9.0 R_{max}$.

As a test of our simulation methods, we compare the mass function and the number density of clusters with those of WOD. In Figure 7.10, we plot the cluster mass functions of our simulations for $M \geq M_*$. Compared with Fig. 3 of WOD, our results are reasonably consistent with their results. The resultant mean separation of $M \geq M_*$ clusters deviates from equation (7.6) less that 3%. Since in WOD equation(7.6) was obtained from fitting the simulation data by Schechter-like function, and since there exist fluctuations in simulation due to strong clustering, this deviation is not unexpected.

In Figures 7.11 and 7.12, we present the results of Q for the modified power law models of different indexes β and different filling factors f. Figures 7.11a and 7.12a give the averaged $\overline{Q}$ as a function of r. For a small filling factor $f = 0.2$, $\overline{Q}$ decrease about 50% with the increase of r about one magnitude. This dependence is weakened as f increases. For the both values of β, $\overline{Q}$ of $f = 0.3 \sim 0.4$ could be well regarded as a constant with high precision($\leq$ 15%). Comparing these results with those of Paper I, we find that the modified power law models have much weaker r-dependence of $\overline{Q}$ than the pure power law models. The variations of $\overline{Q}$ with r are only comparable to those of the constant models, which is very interesting. These results were expected, because the modifications(that is, to remove shells which lie entirely within larger shells and to only include Abell like clusters) mainly eliminate the effects of small shells, thus narrowing the shell radius distribution.

To see the dependence on u, we plot $\overline{Q}$ as a function of u in Figures 7.11b and 7.12b. We can easily find that for all six models $\overline{Q}$ depends on u very weakly. The models of $f = 0.2$ have about 10% fluctuations around their mean values. The fluctuations of $f = 0.3 \sim 0.4$ models are much smaller. The results are very similar to those of the constant models. However, the models have weaker u-dependence compared with the pure power-law models(Paper I).

The dependences of $\overline{Q}$ on v are shown in Figures 7.11c and 7.12c. For all the models, $\overline{Q}$ are approximately constants on $v \leq 0.7$ and rise $15 \sim 30\%$ on the larger v. The similar behaviour was seen in the constant models. In contrast, $\overline{Q}$ remains almost constant on $v \leq 0.8$ but fall about 30% on the larger v in the pure power law models.

To summarize, the modifications considered in this paper greatly improve the power law models on producing the hierarchical form (1). Compared with the constant models, the modified ones produce similar ζ but are more realistic in physical sense and better

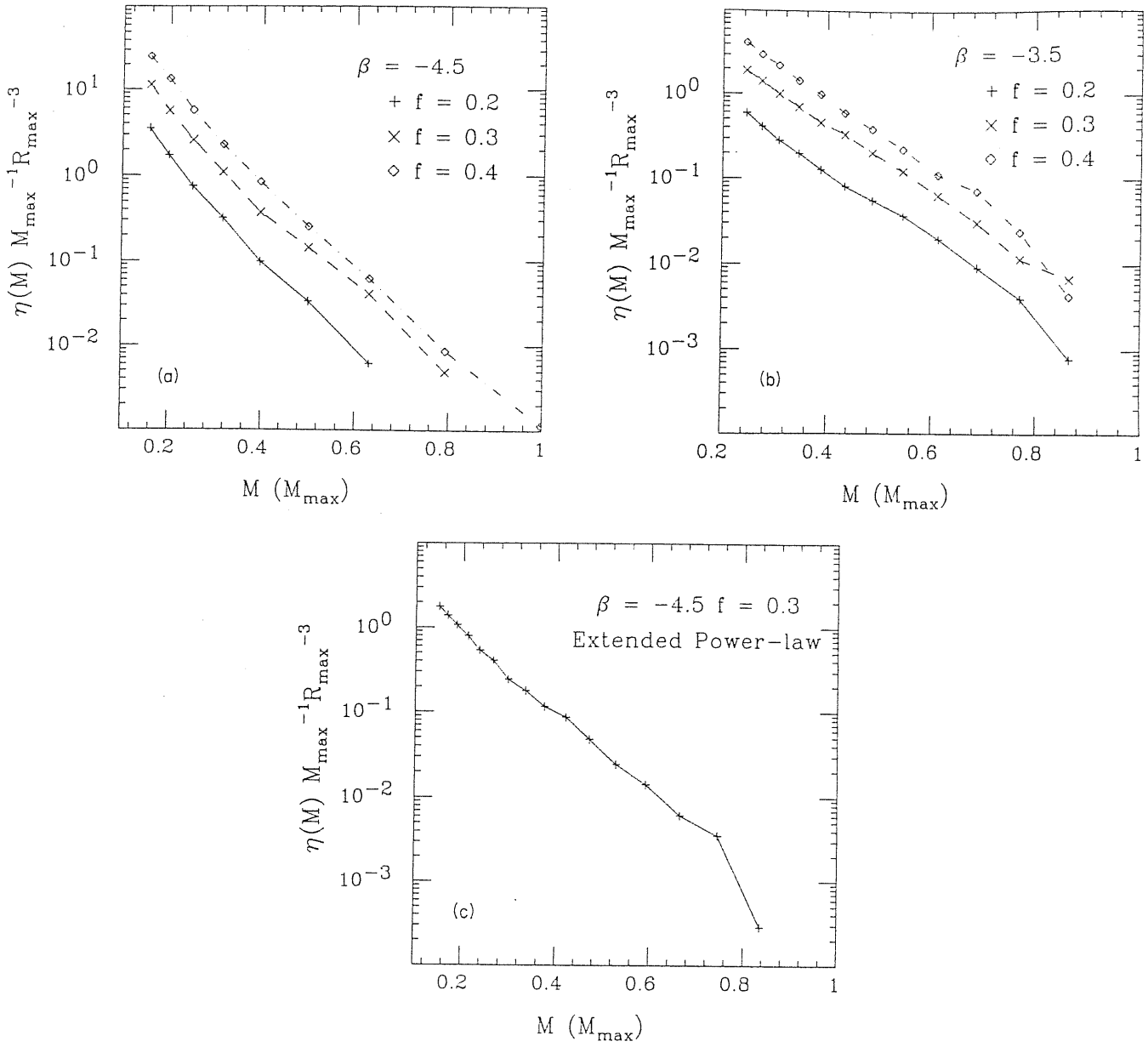

Fig.7.10 — (*a*) The mass functions for the $\beta = -4.5$ modified power law models of different filling factors. (*b*) Same as 7.10(a), but for $\beta = -3.5$. (*c*) Same as 7.10(a), but for the "extended" model. These data are fairly consistent with Weinberg et al.(1989)

on accounting for observational facts , such as, LF of Abell clusters, the observed bubbles in redshift slice surveys, the two-point cluster-cluster function, etc.. If we take into account the observational uncertainties (see, Jing and Zhang, 1989) and the theoretical uncertainties, the modified models can explain well the observed hierarchical form. The mean values of Q are all about 0.85 for $\beta = -4.5$, well consistent with the observations. For $\beta = -3.5$, only the model of $f = 0.3$ produces the right value of Q (~ 0.9); those of $f = 0.2$ and $f = 0.4$ have too high Q values(1.3 and 1.2 respectively) though they are

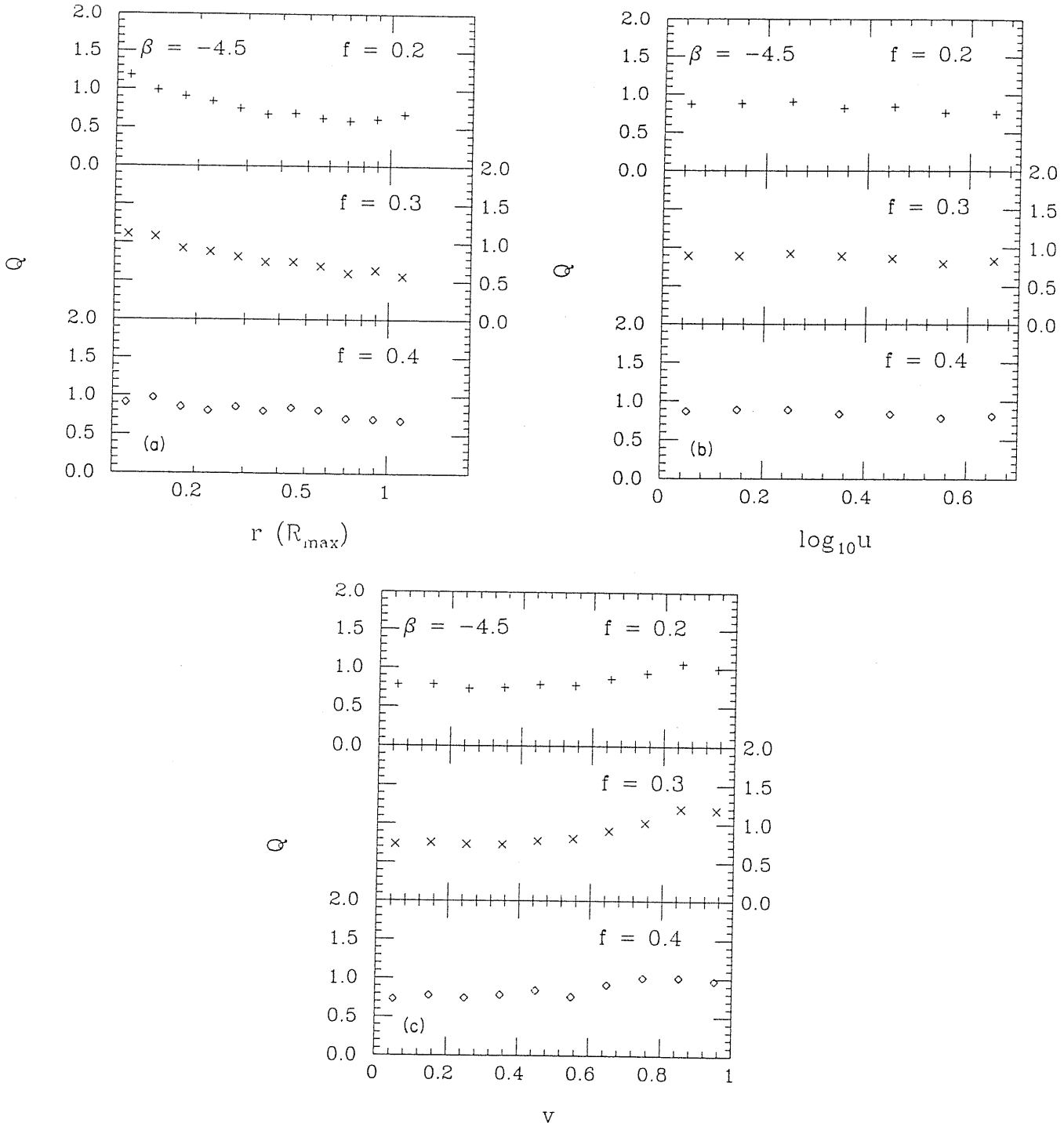

Fig.7.11 — The scaled three-point correlation function Q of the $\beta = -4.5$ models. (a) The averages of Q over all triplets with a fixed r. (b) The averages of Q over all triplets with a fixed u. (c) The averages of Q over all triplets with a fixed v

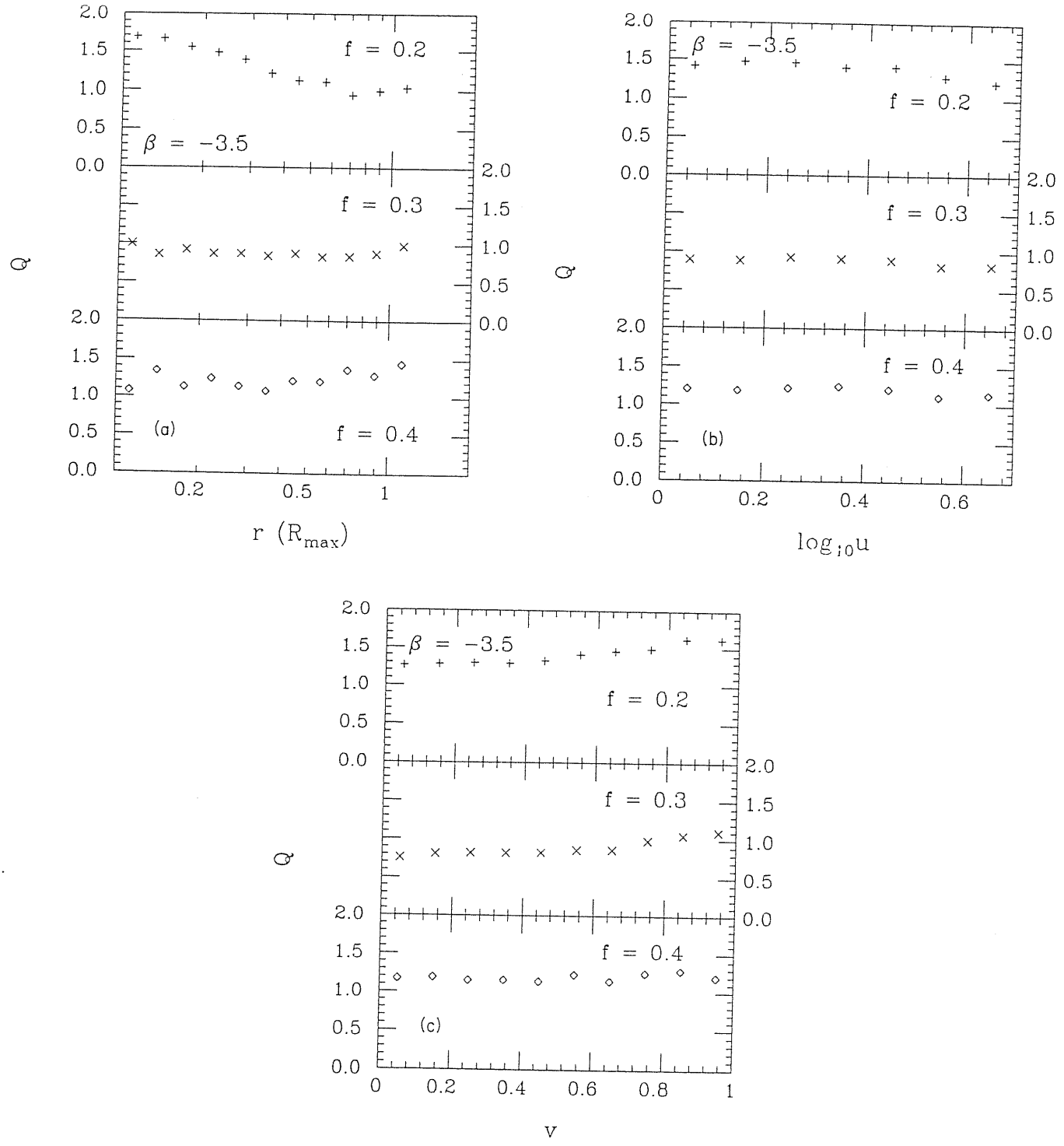

Fig.7.12 — Same as Fig.7.11 but for $\beta = -3.5$

marginally acceptable at 1.5σ. The variations of Q with f of the $\beta = -3.5$ models bother

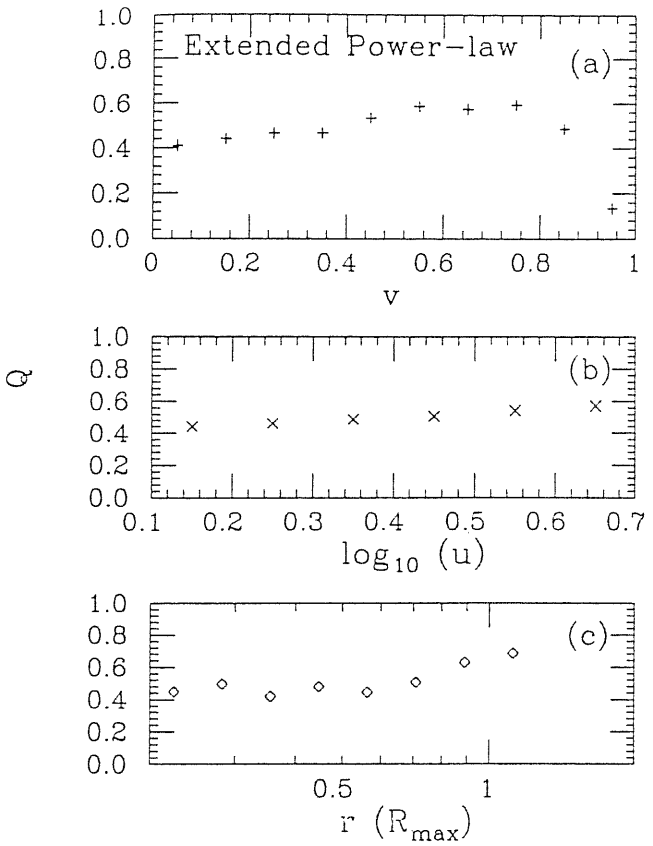

Fig.7.13 Same as Fig.7.11 but for the "extended" model

us. At this stage, it's difficult to judge whether they are caused by the simulation fluctuations or by real features of the models. We are approaching this problem by running larger simulations.

As described in the introduction, it seems inevitable that cluster mergers and shell mergers happen in the real world. WOD show that inclusion of these effects greatly improves the model on fitting the two-point correlation function of Abell clusters. Here we will consider these effects following the techniques of WOD. We merge each group of objects which are separated by less than $R_{max}/5$ into each cluster, and the merged mass is assigned by the mass of its largest component. To approximate the shell mergers, we simply follow the procedures of WOD: eliminate all seeds which lie inside larger shells. We adopt $\beta = -4.5$ and $f = 0.3$, so the model is just the "extended" model of WOD, which was regarded by them as the most successful model on fitting both LF and two-point function of Abell clusters. In Fig. 7.10c, we plot the mass function for clusters of this model, which again accords well with that of WOD.

In Figure 7.13, we present its averaged $\overline{Q}$ as a function of one of the three variables. It is easily seen that for each variable, the mean fluctuations of Q around its mean value are less than about 15%(Here we excluded the point at $v = 0.95$). So the model could be acceptable on reproducing the observed hierarchical form. The mean value of $\overline{Q}$ is about 0.5, close to the lower observational limit.

7.5 Conclusions

We have constructed a set of numerical simulations and studied the three-point correlation functions ζ of clusters in the bubble models. The main conclusions can be summarized as the following.

1). The ζ of the constant models can be expressed well by the hierarchical form with the constant Q about 1, consistent with the observations (except for the f = 0.6 model is at 2σ level).

2). In the power law model, the scaled three-point correlation function Q(r,u,v) depends on u and v very weakly, while has some dependence on r. At small scale r $\leq$ 0.5R, Q remains a constant about 1, however it changes a factor of 1 or 2 at the larger scale.

3). The removal of small shells which lie entirely inside larger shells greatly improves the power law models on producing the observed hierarchical form. The modified models of $\beta = -4.5$ are completely consistent with the observations of ζ. While the modified model of $\beta = -3.5$ and $f = 0.3$ fits the observed ζ very well, those of $f = 0.2$ and $f = 0.4$ have a little too high Q values although they could be acceptable at 1.5σ level.

4). The "extended" model could pass the observational test of ζ, although its mean Q value is close to the lower observational limit.

5). This study has already covered a wide class of bubble models. We are aware that the models presented here are still simplified. However, it is very impressive that the three-point function of clusters, expressed in the hierarchical form, are not very sensitive to the model details. This may indicate that the bubble models meet no obstacle on passing the observational test of ζ.

‡The materials presented in this chapter are based on my two papers: Jing, Y.P. 1990, *Astronomy and Astrophysics*, **233**, 7; Jing, Y.P. 1991, *Monthly Notices of the Royal Astronomical Society*, **248**, 559.

8

Void distributions in ACO cluster catalogue

As discussed in §3.3, the void probability function(VPF) is a very useful tool to extract information on high-order clusterings. In this chapter, I shall present the VPFs of the ACO clusters in two dimensions. Although three-dimensional analysis in principle is much richer than two-dimensional one, several obvious properties lead us to do it. 1) 2-D sample is incomparably larger than 3-D one, because only a small portion of clusters have the measured redshifts; 2) 3-D sample may suffer from the problem of large peculiar velocities(Bahcall *et al.* 1986; however see §5.4), redshifts being not the true distance indicators; 3)As shown by Schaeffer(1987), a universal function $\Sigma(q)$ (its definition will be given below) is approximately same in 2-D and 3-D statistics with corresponding definitions of q, provided clustering is scale invariant, which is just the case for clusters(see below). All this makes the 2-D analysis very attractive.

8.1 Samples and Method

The samples used here are from the new Abell cluster catalogue(Abell, Corwin and Olowin, 1989). We restrict ourselves to analysing the high latitude samples with $|b^{II}| \geq 40°$. We first determine void probability and count probabilities for the largest sample (DR61) with richness $R \geq 1$ and distance $D \leq 6$. In order to study the scaling properties of holes, we separately estimate the VPFs for a subsample (DR51) of $D \leq 5$ and for a subsample (DR62) of $R \geq 2$. A summary of samples is given in Table 8.1

Table 8.1

A Summary of Samples

Sample	b^{II}	Distance	Richness	Number
DR61	$\mid b^{II} \mid \geq 40°$	$\leq$ 6	$\geq$ 1	1950
DR61N	$b^{II} \geq 40°$	$\leq$ 6	$\geq$ 1	919
DR61S	$b^{II} \leq -40°$	$\leq$ 6	$\geq$ 1	1031
DR51	$\mid b^{II} \mid \geq 40°$	$\leq$ 5	$\geq$ 1	829
DR62	$\mid b^{II} \mid \geq 40°$	$\leq$ 6	$\geq$ 2	523

The method to determine the count probability $P_N(\theta)$, which is defined as the probability of finding exactly N clusters in a circle of radius θ, is somewhat similar to that of Bouchet and Lachieze-Rey(1986). We randomly place a set of points in the survey area. For each random point, we draw a set of circles around it with different radius θ, and count the number of clusters in each circle. If a circle crosses the boundaries of the sample, we will throw it away, thus correcting the boundary effects. Then we can easily get the probability functions $P_N(\theta)$, and also obtain the expected counts $<N(\theta)>= \sigma\Omega$ (where σ

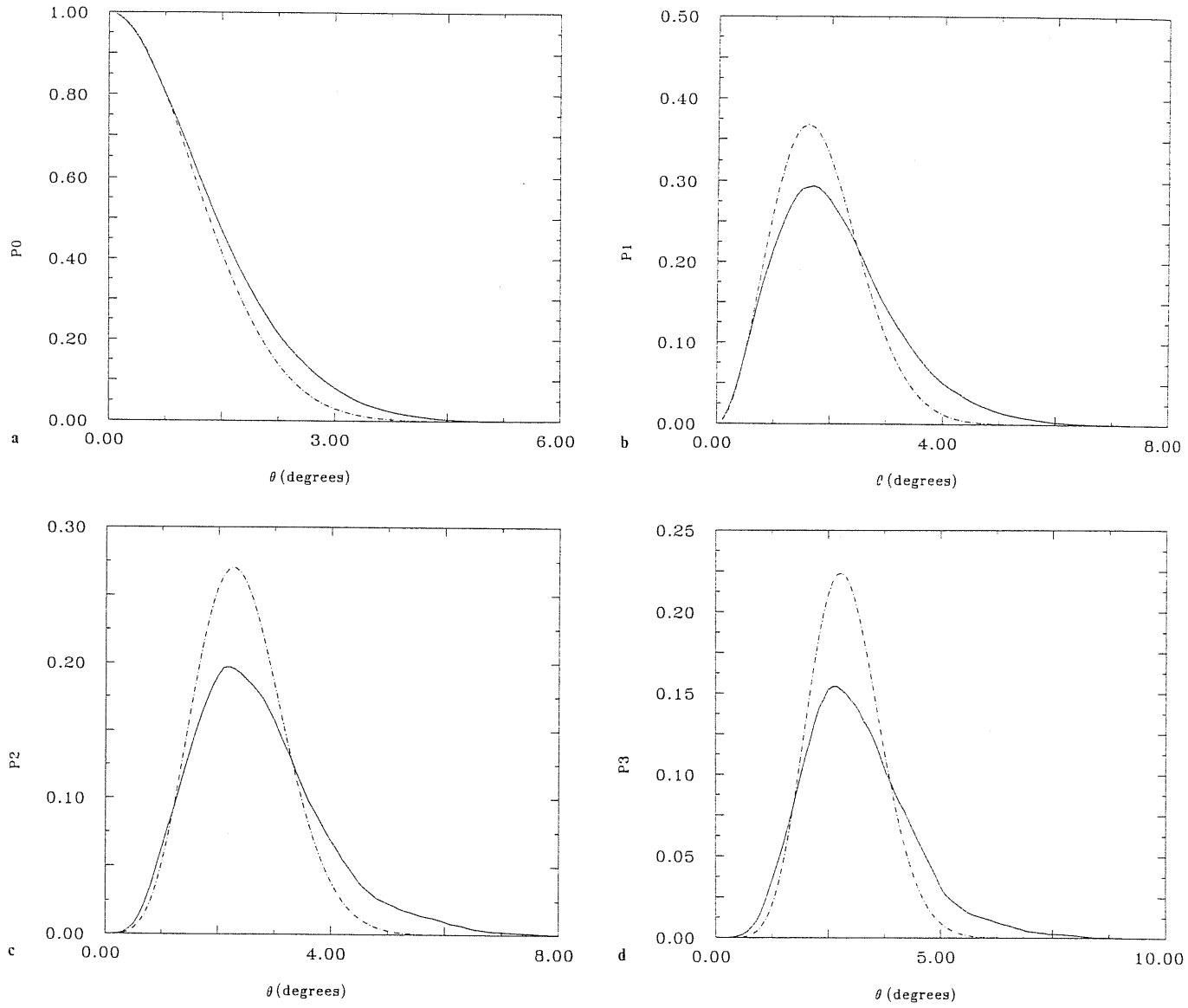

Fig. 8.1 — The count probabilities $P_N(\theta)$, with N = 0–3 (*a–d*) for DR61 sample(the solid lines). The dot-dashed lines represent $P_N(\theta)$ expected for a random catalogue.

is the surface number density of clusters, and Ω is the solid angle of a circle) and its second moment $< (N - < N >)^2 >$. Thus we can simultaneously get the function Σ, which is defined as $\Sigma \equiv \ln P_0/\sigma\Omega$, and the scaling variable $q \equiv \sigma\Omega\overline{\omega(\theta)} =< (N - < N >)^2 > /\sigma\Omega - 1$ (cf. Peebles, 1980), where $\overline{\omega(\theta)} \equiv \frac{1}{\Omega^2}\int \omega(\theta_{12}) d\Omega_1 d\Omega_2$, the average two-point angular correlation function. In the previous papers, q was usually calculated from the two-point correlation function. So our method by passes this problem, and can self-consistently get Σ and q. Here 120,000 random points are taken for DR51 and DR61 samples and 200,000 for DR62 sample, thus minimizing the statistical uncertainty induced by the method. Since the sample lies at the high latitude, galactic extinction effect is very small and we have ignored it in our calculation. The radius θ was taken continously from 0.1° to the largest one, where only one void was detected, with the separation of 0.1°.

8.2 Results and Discussions

8.2.1 Count probabilities

In Figure 8.1, we present the count probabilities $P_N(\theta)$ with N=0—3 for the DR61 sample(solid lines) as well as for a random sample(dot-dashed lines). Although the general behaviours are same in real and random samples, we can find that clustering exists. As expected, there are always more voids in the actual distribution than in the random distribution. For $N \neq 0$, $P_N(\theta)$ flattens more in the cluster catalogue. For small and large circles(as compared with the circle where the maximum P_N shows up), $P_N(\theta)$ of real catalogue is larger, which is also consistent with the fact that superclusters and voids exist in the the real sample.

8.2.2 Function $\Sigma \equiv \ln P_0/\sigma\Omega$ and scaling

As pointed out §3.3, if all n-point correlation functions are scale-invariant, the $\Sigma \equiv \ln P_0/\sigma\Omega$ is only the function of the scaling variable q(White, 1979; Schaeffer, 1984). Sharp (1981) and Bouchet and Lachieze-Rey(1986) analysed the angular void distribution in the Zwicky and CfA catalogue and reached the conclusion that galaxy distribution has scaling invariance.

In Figure 8.2, we plot $\ln P_0/\sigma\Omega$—q for DR61 sample (solid line). Due to large amount of random circles placed, the statistical uncertainties introduced by the method itself are negligible. To see this, we can use the formula of Maurogordato and Lachieze-Rey (1987, hereafter ML) to estimate them. As ML claimed, such errors are significant both on small and on large sizes. We found that the errors of $\Sigma(q)$ are 0.01 at q = 0.1, 0.01 at q = 1.9, 0.02 at q = 2.3 and increase much faster at the larger sizes. So for most part of $q \leq 2.0$, which we are mostly interested in, this kind of error should be much less 0.01. However, the intrinsic errors of sample to sample can not be avoided. To check this, we also analyse the north (DR61N) and south (DR61S) subsamples separately, and the results are also plotted in Figure 8.2. The deviations of the north and of the south from the whole sample can be considered as the intrinsic uncertainties. As the figure shows, for q less than 1.5 (i.e. $\theta < 3.2°$ or r < 30 Mpch^{-1}), Σ of the north and of the south are fitted very well (their differences are less 0.02), so the results in Figure 8.2 of q < 1.5 can be regarded as the true representation of Σ for clusters. For q > 1.5, fluctuation is very large because only a few of voids are detected and the sampling errors become large. Such large intrinsic errors have already prevented us from extracting any useful information on q > 1.5, and from telling whether the decrease of Σ in DR61 for q > 1.5 is the real feature of clustering or not. Below we will only consider Σ for q < 1.5.

To check the scaling, we plot Σ(q) of DR61 sample (solid line) and of DR51 sample(dot-dashed line) separately in Figure 8.3. We can see that for q < 1.5, two curves are superposed with a high accuracy($\Delta\Sigma < 0.01$). That means that the scaling relation is verified. We note that these two samples are very different in mean surface density and in mean depth. And q = 1.5 corresponds $\theta = 3.2°$ or r =30 Mpch^{-1} for DR61 sample and $\theta = 3.6°$ or r = 25 Mpch^{-1} for DR51 sample. So our results support the assumption that cluster distribution is scale-invariant.

8.2.3 A second scaling

As Jing and Zhang(1989) emphasized in their paper, the hierarchical relation(3.1.7) holds for clusters of different richness, and Q is almost same from galaxies to R $\geq$ 2

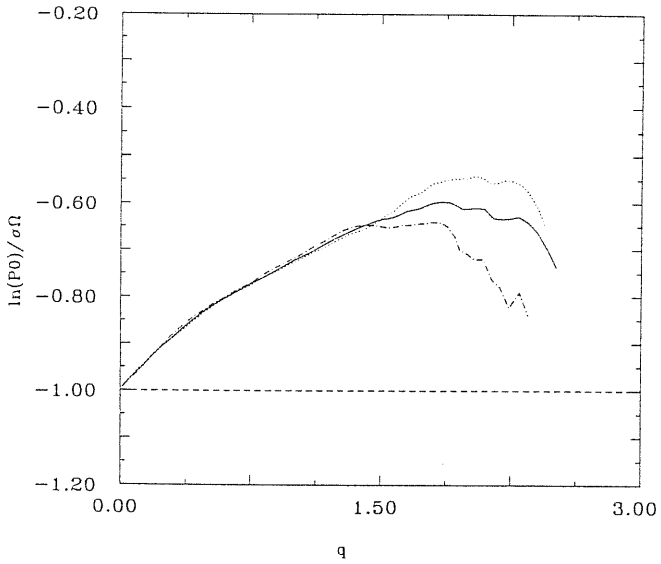

Fig. 8.2 — The $\Sigma \equiv \ln P_0/\sigma\Omega$ as a function of the scaling variable q. The solid line is for the DR61 sample, the dot-dashed line for DR61N and dotted line for DR61S.

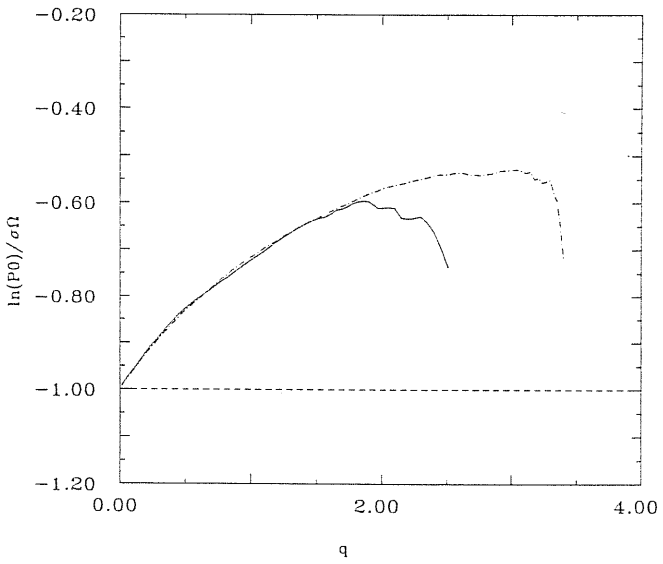

Fig. 8.3 — Same as Figure 8.2. The dot-dashed line is for the DR51 sample, and the solid line for DR61.

clusters. The work of Maurogordato and Lachieze-Rey (1987), which dealt with the void distribution in galaxies of different luminosities, also obtained a similar conclusion that the scaling relation of $\Sigma(q)$ is universal and independent of luminosity. To further examine this scaling property, we estimated the Σ for $R \geq 2$ clusters(DR62 sample), and results are presented in Figure 8.4 (dot-dashed line). We again find that two curves of $R \geq 2$ and of $R \geq 1$ are superposed with a great precision for $q < 1.5$ ($\Delta\Sigma < 0.02$). We have also noted that the mean surface density of $R \geq 1$ clusters is about 4 times higher than that of $R \geq$

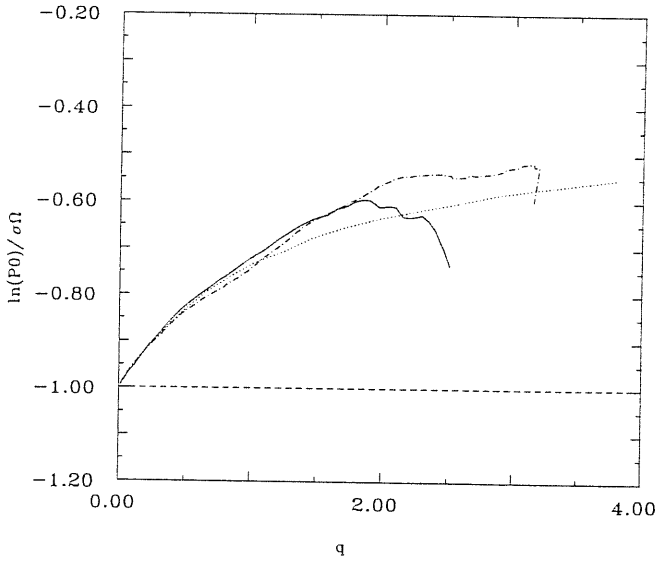

Fig.8.4 — Same as Figure 8.2. The dot-dashed line represents the DR62 sample, the solid line is for DR61 sample and the dotted line is for CfA galaxy catalogue (for comparison).

2, and q =1.5 corresponds to $\theta = 4.8°$ or r = 45 Mpch^{-1} for DR62 sample. This indicates that the scaling distribution of clusters is independent of their richness.

To compare with that of galaxies, we also estimate $\Sigma(q)$ for CfA survey by the same method for the self-consistency reason. From Figure 8.4, we see that the curves of galaxies and of clusters are also very similar.

8.3 Conclusions

In this chapter, we presented the determination of count probabilities $P_N(\theta)$ for the ACO catalogue. Examining the $\Sigma(q)$ of DR61N and DR61S, we found the errors in our measurement are very small for $q < 1.5$. By comparing $\Sigma(q)$ of DR61, DR51, and DR62 samples, we can conclude that cluster distribution is scaling invariant, and this scaling property is independent of their richness. From the further comparison with CfA sample, we tentatively conclude that the scaling relation keeps similar from galaxies to rich clusters of galaxies. This universal scaling would be important to understanding the formation of galaxies. The results obtained here have been confirmed by the recent analysis of Cappi *et al.* (1991) based on small 3-D samples.

‡The materials presented in this chapter are based on my paper: Jing, Y.P. 1990, *Astronomy and Astrophysics*, **233**, 309.

An outlook

In the future, many problems considered here will be further clarified with the advent of a new generation of observational catalogues. Several large deep machine-scanned surveys, such as the APM, COSMOS and POSS II surveys, will be completed in the next few years. Cluster catalogues are being constructed by applying objective finding algorithms to the deep digital sky surveys and to the ROSAT x-ray survey. There are large international efforts on completion of large redshift surveys both of galaxies and of rich clusters. Nearly all topics presented here are expected to be addressed much more accurately in the next decade.

With the increase of the computational capability, the model research is also prospective. Large N-body simulations with good resolutions are being run. Several hydrodynamical codes have been included in the pure gravitational N-body codes. Physical processes of the galaxy formation, such as the 'biasing mechanism', are expected to be better understood with such simulations. Comparisons between theories and observations will thus be made more properly. Our knowledge of the origin and evolution of the LSS will be greatly enhanced by the model studies.

In the thesis, because of the limited space, I have missed several important topics in the LSS studies. These are: $\Delta T/T$ of the cosmic background radiation, the flux dipoles and the peculiar motion of the Local Group, the large scale peculiar velocity fields, etc. These tests are believed the good probes to the primordial density power spectrum $[P(k)]$ and to the contents of the Universe$[\Omega]$. There has been recently noticeable progress on these observations.

Appendix

A. The moment method.

In this Appendix, we shall discuss the moment method used to calculate 3–point correlation function.

Let us then consider a fair sample made of $\mathcal{N}$ objects distributed in a given volume $\mathcal{V}$. Around each object we center spheres of radii r_k. Let δr_k be the thickness of the shell between the $(k-1)$-th and the k-th sphere and N_{jk} be the number of neighbours of the j-th object in the shell. We shall then take the average of N_{jk}, made over the $\mathcal{N}$ possible j's, $N_k =< N_{jk} >_j$.

Afterwards, we generate an artificial sample of $\bar{\mathcal{N}} >> \mathcal{N}$ objects, distributed in the same volume $\mathcal{V}$ with the same selection effects as the original sample.

Let then be $\bar{N}_k = (\mathcal{N}/\bar{\mathcal{N}}) < \bar{N}_{kj} >_j$. Here $\bar{N}_{jk}$ is the number of *random* neighbours of the j-th object in the shell k[let us draw the attention on the normalization factor $(\mathcal{N}/\bar{\mathcal{N}})$].

The 2–point function $\xi(r_k) = \xi_k$ can then be defined according to

$$N_k = \bar{N}_k(1 + K(\delta_k)\xi_k) \tag{A.1}$$

where $\delta_k = \delta r_k / r_k$.

Here, assuming

$$\xi(r) \;=\; (r_{cc}/r)^{\gamma}, \tag{A.2}$$

it is

$$K(\delta) \;=\; K_{\gamma,\delta} \;=\; \frac{3}{\gamma_3}\frac{(1-(1-\delta)^{\gamma_3})}{1-(1-\delta)^3} \tag{A.3}$$

where

$$\gamma_i = i - \gamma. \tag{A.4}$$

Among the central moments

$$S_k^{(m)} \;= < (N_{kj} - N_k)^m >_j \tag{A.5}$$

providing information on the $(m+1)$-point function, we shall consider, in particular,

$$S_k^{(2)} \;= < N_{kj}^2 >_j - N_k^2. \tag{A.6}$$

Let us then consider the joint expected numbers of objects in δV_1 and δV_2 at distances r_{01} and r_{02} from real objects

$$< \delta N_1 \delta N_2 >= \delta\bar{N}_1 \delta\bar{N}_2(1 + \xi_1 + \xi_2 + \xi_{12} + \zeta_{012}), \tag{A.7}$$

which depends on the connected 3-point function ζ. [In (A.7) and hereafter $\xi_i = \xi(r_{0i})$ while $\delta\bar{N}_1$ and $\delta\bar{N}_2$ are the (normalized) numbers of random objects in δV_1 and δV_2.]

As already outlined, we shall consider here two alternative expressions for ζ_{012} :

$$\zeta_{012} = Q(\xi_1\xi_2 + \xi_1\xi_{12} + \xi_2\xi_{12}) \ , \qquad (hm)$$

$$\zeta_{012} = \tilde{Q}(\xi_1\xi_2 + \xi_1\xi_{12} + \xi_2\xi_{12} + \xi_1\xi_2\xi_{12}) \ , \qquad (ks)$$

Here *hm* stands for *hierarchical model* and *ks* for *Kirkwood superposition*. The former expression does not actually follow from the requirement of hierarchical clustering (bottom–up scenarios), but is fully coherent with it. The latter expression, first introduced by Kirkwood in the study of gases, expresses a limiting case in the framework of *biased* theories of galaxy formation; it should then also be $\tilde{Q} = 1$. In what follows we shall use first *hm*, eventually correcting results with the extra terms arising from *ks*.

Let us then integrate (A.7) over $\mathbf{r_1}$ and $\mathbf{r_2}$ in the k-th shell. The result is to be corrected to subtract the effect of the *overlapped* physical objects. This leads to the relation

$$S_k^{(2)} - N_k = \bar{N}_k^2[J_{\gamma,\delta_k}\xi_k + ((Q-1)K_{\gamma,\delta_k}^2 + 2Q\tilde{K}_{\gamma,\delta_k})\xi_k^2] \qquad (A.8)$$

holding for *hm*. Here

$$J_{\gamma,\delta} = \frac{1}{8(1-\delta+\delta^2/3)^2}\frac{1}{\gamma_3\gamma_4}\times$$

$$\{\frac{2^{\gamma_6} - 2(2-\delta)^{\gamma_6} + [2(1-\delta)]^{\gamma_6}}{\delta^2\gamma_6} - \frac{8\delta^{\gamma_2}}{\gamma_2}(1-\delta+\delta^2\gamma_6) + 2(2-\delta)^{\gamma_4}\gamma_2\}. \qquad (A.9)$$

and

$$\tilde{K}(\gamma,\delta) = \frac{1}{\gamma_2\gamma_3}\frac{1}{2\left(1-\delta+\frac{\delta^2}{3}\right)^2}\times$$

$$\int_0^1 dx(1-x\delta)^{\gamma_1}\left[2^{\gamma_3}\frac{\left(1-\frac{x}{2}\delta\right)^{\gamma_3} - \left(1-\frac{x+1}{2}\delta\right)^{\gamma_3}}{\delta} - \frac{2^{\gamma_4}}{\gamma_4}\frac{\left(1-\frac{x}{2}\delta\right)^{\gamma_4} - (1-x+12\delta)^{\gamma_4}}{\delta} + \right.$$

$$\left. +2^{\gamma_3}\left(1-\frac{x+1}{2}\delta\right)^{\gamma_3} - \delta^{\gamma_2}\left((1-x)^{\gamma_3} + x^{\gamma_3}\right) + \delta^{\gamma_3}\left((1-x)^{\gamma_3} + \frac{x^{\gamma_4} - (1-x)^{\gamma_4}}{\gamma_4}\right)\right] \qquad (A.10)$$

Then, according to (A.6) and (A.8),

$$Q = \frac{1}{c_1(\delta,\gamma)}\left[\frac{S_k^{(2)} - N_k}{(N_k - \bar{N}_k)^2} - c_2(\delta,\gamma)\frac{\bar{N}_k}{N_k - \bar{N}_k} + 1\right] \qquad (A.11)$$

where

$$c_1(\delta,\gamma) = 1 + \frac{2\tilde{K}_{\gamma,\delta_k}}{K_{\gamma,\delta_k}^2}$$

$$c_2(\delta,\gamma) = \frac{J_{\gamma,\delta}}{K_{\gamma,\delta_k}} \qquad (A.12)$$

For *ks*, (A.11) ought to be modified into

$$\tilde{Q} = \frac{1}{c_1(\delta,\gamma) + c_3(\delta,\gamma)\frac{N_k - \bar{N}_k}{\bar{N}_k}}\left[\frac{S_k^{(2)} - N_k}{(N_k - \bar{N}_k)^2} - c_2(\delta,\gamma)\frac{\bar{N}_k}{N_k - \bar{N}_k} + 1\right] \qquad (A.13)$$

with

$$c_3(\delta,\gamma) = H_{\gamma,\delta}/K^3_{\gamma,\delta} \qquad (A.14)A$$

where

$$H\gamma,\delta \;=\; \frac{1}{V^2\xi^3}\int_{R-\delta R}^{R}\xi_1\xi_2\xi_{12}dV_1dV_2 =$$

$$= \frac{1}{\gamma_2}\frac{1}{2\delta^2\left(1-\delta+\frac{\delta^2}{3}\right)^2}\int_{1-\delta}^{1}dx_1x_1^{\gamma_1}\int_{1-\delta}^{1}dx_2x_2^{\gamma_1}\left[(x_1+x_2)^{\gamma_2}-|x_1-x_2|^{\gamma_2}\right]\ . \qquad (A.15)$$

(some above relations are taken from Pons et al. 1990).

The division of the distance axis r into intervals (*bins*) δr_k is to be performed in a suitable distance interval r_{min}, r_{max}. In the case of *pointlike* objects (galaxies, QSO's, etc.) we can take $r_{min} = 0$. This is not convenient for more complicated systems, with an intrinsical characteristic size l, as clusters of galaxies are. It is then wise taking r_{min} at least a few times greater than l. A reasonable choice for r_{max}, instead, is $\sim r_{cc}$. Above $\sim 2\,r_{cc}$ the very law (A.2) can no longer be granted that it holds. Therefore, in our case, we have taken $r_{min} = 7\ h^{-1}Mpc$ and $r_{max} = 26\ h^{-1}Mpc$.

A further point is the sharing of the interval $\Delta r = r_{max} - r_{min}$ into δr_k's. If no sharing is performed and $\delta r = \Delta r$, there is no direct possibility of checking the expressions hm and/or ks. If one shares Δr in a few δr_k, different (but non independent) estimates of Q ($\tilde{Q}$) follow from each bin. Their agreement is an indication of the validity of the expression used for the 3-point function.

Each bin collects the information concerning triplets set on the vertices of triangles with 2 sides having length between $r_k - \delta r_k$ and r_k and a third side between 0 and $2\,r_k$. For small δr_k, each bin tends to report information coming from nearly isosceles triangles, with two sides $\sim r_k$. It is clear that this selection leaves apart the contribution of a number of possible triplets, whose geometry does not fulfill the above requirements.

Any sharing is however to be carefully performed in order that at least a few triplets remain in each bin. Too small δ_k cause empty bins or bins where all objects have 0 or 1 partners. Negative Q estimates then appear. They bear no physical meaning being caused by the artificial suppression of existing triplets (2 partners for some object). In any case the minimal variation of Q arising formally adding an extra partner to each object in a shell is to be checked. Such variation

$$\Delta Q_k \;=\; [\mathcal{N}_k c_1(\delta,\gamma)(N_k - \bar{N}_k)^2]^{-1} \qquad (A.16)$$

($\mathcal{N}_k$: total number of objects in the k-th shell) can be large; ΔQ_k allows then to evaluate the convenience to use a given small δr_k. Furthermore, in possible averaging procedures, the estimate of Q coming from a given shell should be given a weight inversely proportional to the corresponding ΔQ_k.

References

Aaronson, M., Bothun, G., Mould, H., Huchra, J., Schommer, R., & Cornell, M. 1986, *ApJ*, **302**, 536

Abell, G.O. 1958, *ApJS*, **3** , 211

Abell, G.O., Corwin, H.G., & Olowin, R.P. 1989, *ApJS*, **70** , 1

Adler, R.J. 1980, *The Geometry of Random Fields*, Willy, New York.

Audouze, J., Pelletan, M.C., & Szalay, A.(eds) 1988, *Large Scale Structures in the Universe*, IAU Symp.**130**, Kluwer Academic Publishers

Bahcall, N.A. 1979, *ApJ* **232**, 689

Bahcall, N.A. 1988a, *An.Rev.Astr.Ap.*, **26** , 631

Bahcall, N.A. 1988b, in *IAU Symposium 130, Evolution of Large-Scale Structures in the Universe.* eds. J. Audouze, M.-C.Pelletan and A. Szalay (Kluwer Academic Publishers), p229

Bahcall, N.A., & Soneira, R.M. 1982, *ApJ* **262**, 419

Bahcall, N.A., & Soneira, R.M. 1983, *ApJ*, **270** , 20 (BS83)

Bahcall, N.A., & Soneira, R.M. 1984, *ApJ*, **277** , 27

Bahcall, N.A., Soneira, R.M., & Burgett, W. 1986, *ApJ*, **311**, 28

Bahcall, N.A., Henriksen, M.J., & Smith, T.Ed. 1989, *ApJ* **346**, L45

Bardeen, J.M., Bond, J.R., Kaiser, N., & Szalay, A.S. 1986, *ApJ*, **304** , 15.

Barrow, J.D., Bhavsar, S.P., & Sonoda, D.H. 1984, *MNRAS*, **210**, 19P.

Barrow, J.D., Bhavsar, S.P., & Sonoda, D.H. 1985, *MNRAS*, **216**, 17

Barrow, J.D., & Bhavsar, S.P. 1983, *MNRAS*, **205**, 61p.

Batuski, D.J. & Burns, J.O. 1985a, *AJ*, **90** , 1413

Batuski, D.J. & Burns, J.O. 1985b, *ApJ*, **299**, 5

Batuski, D.J., Melott, A.L., & Burns, J.O. 1987, *ApJ*, **322**,48

Batuski, D.J., Bahcall, N.A., Olowin, R.P, & Burns, J.O. 1989, *ApJ*, **341**, 599

Bean, A.J., Efstathiou, G., Ellis, R.S., Peterson, B.A., & Shanks, T. 1983, *MNRAS*, **205**, 605.

Bennet, D., & Bouchet, F. 1988, *Phys. Rev. Letters* **60**, 257

Bertschinger, E. W. 1985, *ApJS* **58**, 1

Bhavsar, S.P. 1978, *ApJ*, **222**, 412

Bhavsar, S.P. 1980, *ApJ*, **237**, 671

Bhavsar, S.P., & Ling, E.N. 1987, *ApJ*, **331**, L63

Binggeli, B. 1982, *A&A*, **107**, 338

Binggeli, B., Sandage, A., & Tammann, G.A. 1988, *An. Rev. Astr.Ap.*, **26**, 509

Binggeli, B., Tareghi, M., & Sandage, A. 1990, *A&A*, **228**, 42

Bond, J.R., Efstthiou, G., Lubin, P.M., & Meinhold, P.R. 1991, *Phys. Rev. Lett.*, **66**, 2179

Borgani, S. 1990, *MS thesis*, SISSA, Trieste.

Borgani, S., Jing, Y.P., & Plionis, M. 1991, (in preparation)

Börner,G., Mo,H.J. 1990, *A&A*, **227**, 324.

Börner,G., Mo,H.J., Zhou,Y.Y. 1989, *A&A*, **221**, 191.

Bothum, G.D., Beers, T.C., Mould, J.R., & Huchra, J.P. 1986, *ApJ*, **308**, 510

Bouchet, F. R., & Lachieze-Rey, M. 1986, *ApJ* **302**, L37

Brown, E.M. & Groth, E.J. 1989, *ApJ*, **338**, 605

Calzetti,D., Giavalisco,M., & Ruffini,R. 1988, *A&A* **198**, 1

Cappi, A., Maurogordato, S., & Lachiéze-Rey, M. 1991, *A&A*, **243**, 28

Carr, B. J., Bond, J. R., & Arnett, W. D. 1984, *ApJ* **277**, 445

Chincarini, G., Rood, H.J., & Thompson, L.A. 1981, *ApJ*, **249**, L47

Coles, P. 1988, *MNRAS*, **234**, 509

Coles, P. & Plionis, M. 1991, *MNRAS*, **250**, 75.

Collins, C.A., Heydon-Dumbleton N.H., & MacGillicray, H.T. 1989 *MNRAS*, **236**, 7p

Couchman, H.M.P., McGill, C., & Olowin, R.P. 1989, *MNRAS*, **239** , 513

da Costa, L.N., Pellegrini, P.S., Davis, M., Meiksin, A., Sargent, W.L.W., & Tonry, J.L. 1991 *ApJS*, **75**, 935

Davis, M., & Geller, M.J. 1976,*ApJ* **208**,13.

Davis,M., Geller,M.J., & Huchra,J., 1978,*ApJ* **221**,1.

Davis, M., & Peebles, P.J.E. 1983,*ApJ* **267**,465.

Davis, M., Efstathiou, G., Frenk, C. S., & White, S. D. M. 1985, *ApJ*, **292**, 371

Davis, M., Meiksin, A., Stauss, M.A., da Costa, L.N., & Yahil, A. 1988, *ApJ*, **333**,L9.

Dekel, A. 1988, in *IAU Symposium 130, Evolution of Large-Scale Structures in the Universe.* eds. J. Audouze, M.-C.Pelletan and A. Szalay (Kluwer Academic Publishers), p598

Dekel, A., & West, M.J. 1985, *ApJ*, **288**, 411

Dekel, A., & Silk, J. 1986, *ApJ*, **303**, 39

Dekel, A. & Rees, M.J. 1987, *Nature*, **326**, 455

Dekel, A., Blumenthal, G.R., Primack, J.P., & Olivier, S. 1989, *ApJ*, **338**, L5

de Lapparent, V., Geller, M. J., & Huchra, J. P. 1986, *ApJ*, **302**, L1 (LGH)

de Lapparent, V., Geller, M. J., & Huchra, J. P. 1988, *ApJ*, **332**, 44

Dressler, A., Fader, S.M., Burstein, D., Davies, R.L., Lynden-Bell, D., Terlevich, R.S. & Wegner, G. 1987, *ApJ*, **313**, L37

Eder, J.A., Schombert, J.M., Dekel, A., & Oemler, Jr.,A. 1989, *ApJ*, **340**, 29

Efstthiou, G. 1988, In *Large-Scale Motions in the Universe*, eds. V.C. Rubin and G.V. Coyne, Princeton Univ. Press, p299

Efstathiou, G., & Silk, J., 1983, *Fundamentals of Cosmic Physics*, **9**, 1.

Efstathiou, G., & Jedrzejewski, R.I., 1984, *Adv. Space Res.*, **3**, 379.

Efstathiou, G., Ellis, R.S., & Peterson, B.A. 1988, *MNRAS*, **232**, 431

Efstathiou, G., Kaiser, N., Saunders, W., Lawrence, A., Rowan-Robinson, Ellis, R.S., & Frenk, C.S. 1990 *MNRAS*, **247**, 10p

Einasto,J., Klypin,A., Saar,E. & Shandarin, S.F. 1984, *MNRAS*, **206**, 529

Einasto, J., Klypin, A., & Saar, E. 1986, *MNRAS* **219**,457.

Fall, S. M., & Tremain, S. 1977, *ApJ* **216**, 682

Frenk, C.S., White, S.D.M., Davis, M. & Efstathiou, G., 1988, *ApJ*, **327**, 507

Fry, J.N. 1984, *ApJ*, **277**, L5

Fry, J.N., & Melott, A.L. 1985, *ApJ*, **292**, 395

Fry, J.N., Giovanelli, R., Haynes, M.P., Melott, A.L., and Scherrer, R.J. 1989 *ApJ*, **340**, 11

Gao, Y., & Jing, Y.P. 1989, *MNRAS*, **236**, 559

Geller, M.J. & Huchra, J.P. 1983 *ApJS*, **52**, 61

Geller, M.J., & Huchra, J.P., 1988, In *Large-Scale Motions in the Universe*, eds. V.C. Rubin and G.V. Coyne, Princeton Univ. Press, p3

Giovanelli, R., Haynes, M.P., & Chincarini,G.L. 1986, *ApJ* **300**,77

Gott, J.R., Melott, A.L., & Dickinson, M. 1986 *ApJ*, **306**, 341

Gott, J.R., Miller, J., Thuan, T.X., Schneider, S.E., Weinberg, D.H., Gammie, C., Polk, K., Vogeley, M., Jeffrey, S., Bhavsar, S.P., Melott, A.L., Giovanelli, R., Haynes, M.P., Tully, R.B., & Hamilton, A.J.S. 1989 *ApJ*, **340**, 625

Gott, J.R., Gao, B., & Park, C. 1991, *Preprint*

Gregory, S.A., Thompson, L.A., & Tifft, W.G. 1981, *ApJ* **243**, 411

Groth,E.J., & Peebles,P.J.E. 1977,*ApJ* **217**, 385.

Hamilton, A.J.S., Gott, J.R., & Weinberg, D. 1986, *ApJ*, **309**, 1

Hauser, H.G., & Peebles, P.J.E. 1973, *ApJ*, **185** , 757

Haynes, M.P., & Giovanelli, R. 1986, *ApJ*, **306**, L55

Hoessel, J.G., Gunn, J.E., & Thuan, T.X. 1980, *ApJ*, **241**, 486

Hollósi, J., & Efstathiou, G. 1988,

Holtzman, J.A. 1989, *ApJS*, **71**, 1

Huchra, J.P., & Geller, M.J. 1982 *ApJ*, **257**, 423

Huchra, J., Davis, M., Latham, D. & Tonry, J. 1983 *ApJS*, **52**, 89

Huchra, J.P., Henry, J.P., Postman, M., & Geller, M.J. 1990a, *ApJ*, **365**, 66

Huchra, J.P., Geller, M.J., de Lapparent, V. & Corwin, H.G. 1990b, *ApJS*, **72**, 433

Ikeuchi, S. 1981, *Pub. Astr. Soc. Japan* **33**, 211

IRAS *Point Source Catalog*, Version 2, 1988. Joint *IRAS* Working Group, GPO, Washington, DC

Jesen, L.G., & Szalay, A.S.1986, *ApJ*, **305**, L5

Jing, Y.P. 1990a, *A&A* **233**, 7

Jing, Y.P. 1990b, *A&A* **233**, 309

Jing, Y.P. 1991, *MNRAS* **248**, 559

Jing, Y.P., & Zhang, J.L. 1987, *Astrophys. Spa. Sci.* **138**, 105

Jing, Y.P., & Zhang, J.L. 1988, *A&A*, **190**, L21

Jing, Y.P., & Zhang, J.L. 1989, *ApJ*, **342**, 639

Jing, Y.P., & Valdarnini, R. 1991a, *A&A*, (in press)

Jing, Y.P., & Valdarnini, R. 1991b, (in preparation)

Jing, Y.P., Mo, H.J., & Bórner, G. 1991a, *A&A*, (in press)

Jing, Y.P., Plionis, M., & Valdarnini, R. 1991b, *ApJ*, (submitted)

Jing, Y.P. *et al.* 1991c, (in preparation)

Joeveer, M., Einasto, J., & Tago, E. 1978, *MNRAS*, **185**, 357

Kaiser, N. 1986, *MNRAS*, **219**, 785

Kaiser, N. 1984, *ApJ*, **284**, L9.

Kashlinsky, A. 1987, *ApJ*, **317**, 19

Klypin, A.A., & Kopylov, A.I. 1983, *Soviet Astr. Letters*,**9**, 41

Kopylov, A.I., Kuznetsov, D. Yu., Fetisova, T.S., & Shvartsman, V.F. 1987, in *Proc. Semm. Large Scale Structure of the Universe, 1986*, P39. Stavropol, USSR Spec. Astrophys. Obs.

Kulsrud, R. M., & Cowley, S. C. 1989, *ApJ* **346** 546(KC)

Lahav,O., Rowan-Robinson,M., & Lynden-Bell,D. 1988, *MNRAS*, **234**,677 (LRL)

Lahav, O., Edge, A.C., Fabian, A.C., & Putney, A. 1989, *MNRAS*, **238**, 881

Lauberts, A. 1982, *The ESO-Uppsala Survey of the ESO(B) Atlas*, European Southern Observatory

Leir, A.A., & van den Bergh, S. 1977, *ApJS*, **34**, 381

Ling, E.N., Frenk, C.S., & Barrow, J.D. 1986 *MNRAS*, **223**, 21p

Lilje, P.B., & Efstathiou, G. 1988, *MNRAS*, **231**, 635

Lucey, J.R. 1983, *MNRAS*, **204**, 33

Lucey, J.R., & Carter, D. 1988, *MNRAS*, **235**, 1177

Maia, M.A.G., da Costa, L.N., & Latham, D.D. 1989 *ApJS*, **69**, 809

Maia, M.A.G., & da Costa, L.N. 1990, *ApJ*, **349**, 477

Maddox, S.J., Efstathiou, G., Sutherland, W.J., & Loveday, J. 1990a, *MNRAS*, **242**, 43p.

Maddox, S.J., Sutherland, W.J., Efstathiou, G., & Loveday, J. 1990b *MNRAS*, **243**, 692

Matarrese, S., Lucchin, F., & Bonometto, S.A. 1986, *ApJ*, ,

Matarrese, S., Lucchin, F., Messina, A., & Moscardini, L. 1991, *MNRAS*, (in press)

Mattig, W. 1958, *Astr. Nach.*, **284**, 109

Maurogordato, S., & Lachieze-Rey, M. 1987, *ApJ* **320**, 13

Melott, A.L. 1990, *Phys. Rep.*, **193**, 1

Melott, A.L., & Fry, J.N. 1986, *ApJ*, **305**, 1

Metcalfe, N., Fong, R., Shanks, T., & Kilkenny, D. 1989, *MNRAS*, **236**, 207

Mo, H.J., & Börner, G. 1990, *A&A*, **238**, 3

Mo, H.J., & Jing, Y.P. 1991, (in preparation)

Nilson,P., 1973, *Uppsala General Catalogue of Galaxies*, Uppsala.

Olivier, S., Blumenthal, G.R., Dekel, A., Primack, J.R., & Stanhill, D. 1990, *ApJ*, **356**, 1

Ostriker, J.P., & Cowie, L.L. 1981, *ApJ*, **243**, L127

Ostriker, J. P., Thompson, C., Witten, E. 1986, *Phys. Letters B* **180**, 231

Ostriker, J.P. 1988, in *IAU Symposium 130, Evolution of Large-Scale Structures in the Universe.* eds. J. Audouze, M.-C.Pelletan and A. Szalay (Kluwer Academic Publishers), p321

Otto, S., Politzer, H. D., Preskill, J., and Wise, M. B. 1986 *ApJ* **304**, 62

Parry, W.E. 1977, *Phys. Lett.* **60A**, 265

Peebles, P.J.E. 1975, *ApJ*, **196**, 647

Peebles, P.J.E. 1979, *AJ*, **84**, 730

Peebles, P.J.E. 1980, *The large-scale structure of the Universe*, Princeton Princeton University Press

Peebles, P.J.E. 1981, in *Annals New York Academy of Science*, P157

Peebles, P.J.E. 1982, *ApJ*, **263**, L1

Peebles, P.J.E., & Groth, E.J. 1975, *ApJ* **195**, 1

Pellegrini, P. S., Willmer, C.N.A., da Costa, N. & Santiago, B.X. 1990, *ApJ*, **350**, 95

Picard, A. 1991, *ApJ*, **368**, L7

Pietronero, L. 1987, *Physica*, **144A**, 257.

Politzer, D., & Wise, M.B. 1984, *ApJ*, **285** , L1

Pons, B., Iovino, M.J., Bonometto, S.A. 1991, *AJ*

Postman, M., Huchra, J.P., Geller, M.J., & Henry, J.P. 1985, *AJ*, **90** , 1400

Postman, M., Geller, M.J., & Huchra, J.P. 1986, *AJ*, **91** , 1267

Postman, M. Geller, M.J. & Huchra, J.P. 1988, *AJ*, **95**, 267

Postman, M., Spergel, D.N., Satin, B., & Juszkiewicz, R. 1989, *ApJ*, **346** , 588

Plionis, M. 1988, *MNRAS*, **234**, 401

Plionis, M., Barrow, J.D., & Frenk, C.S. 1991, *MNRAS*, **249**, 662

Plionis, M., & Borgani, S. 1991, *MNRAS*, **251**, 575.

Plionis, M., Valdarnini, R. & Jing, Y.P. 1991, *in preparation*

Ramella, M., Geller, M.J., & Huchra, J.P. 1989 *ApJ*, **344**, 57

Ramella, M., Geller, M.J., & Huchra, J.P. 1990 *ApJ*, **353**, 51

Readhead, A.C.S., Lawrence, C.R., Myers, S.T., Sargent, W.L.W., Hardeback, H.E., & Moffet, A.T. 1989, *ApJ*, **346**, 566

Salzer, J.J., Hanson, M.M., & Gavazzi, G. 1990, *353*, 39

Santiago, B.X., & da Costa, L.N. 1990, *ApJ*, **362**, 386

Saunders, W., Rowan-Robinson, M., Lawrence, A., Efstathiou, G., Kaiser, N., Ellis, R.S., & Frenk, C.S. 1990, *MNRAS*, **242**, 318

Schaeffer, R. 1984, *A & A*, **134**, L15

Schaeffer, R. 1987, *A & A* **180**, L5

Seldner, M., Siebers, B., Groth, E.J., & Peebles, P.J.E. 1977, *AJ*, **82**, 249

Shane, C.D. & Wirtanen, C.A. 1967, Pub. Lick. Obs., **22**, 1

Sharp, N. A. 1981, *MNRAS* **195**, 857

Sharp, N.A., Bonometto, S.A., & Lucchin, F. 1984, *A&A*, **130**, 79.

Shectman, S.A. 1985, *ApJS* **57**, 77

Seldner, M., & Peebles, P.J.E. 1977, *ApJ*, **215**, 703

Solton, A. 1988, *MNRAS* **231**, 309

Soneira, R.M., & Peebles, P.J.E. 1978 *AJ*, **83**, 845

Strauss, M. A., Davis, M., Yahil, A. and Huchra, J.P. 1990 *ApJ*, **361**, 49

Struble, M.F., & Rood, H.J. 1991a, *ApJS*, (submitted)

Struble, M.F., & Rood, H.J. 1991b, *ApJ*, **374**, 395

Sutherland, W. 1988, *MNRAS*, **234** , 159 (S88)

Sutherland, W., & Efstathiou, G. 1991, *MNRAS*, **248**, 159 (SE91)

Szalay, A.S., Hollósi, J., & Tóth, G. 1989, *ApJ*, **339**, L5

Szalay, A. S. 1988, *ApJ* **333**, 21

Thuan, T.X., & Seitzer, P.O. 1979, *ApJ*, **231**, 327

Thuan, T.X., Gott, J.R., & Schneider, S.E. 1987 *ApJ*, **315**, L93

Thuan, T.X., Alimi, J.M., Gott, J.R., & Schneider, S.E. 1991 *ApJ*, **370**, 25

Tóth, G., Hollósi, J., & Szalay, A.S. 1989, *ApJ*, **344**, 65

Tully, B. 1987, *Ap.J*, **323**, 1

Turok, N. 1985, *Phys. Rev. Letters* **55**, 1700

Turok, N., Brandenberger, R. H. 1986 *Phys. Rev.* **D33**, 2175

Valdarnini, R., & Borgani, S. 1991, *MNRAS*, (in press)

Weinberg, D.H. 1988, *PASP*, **100**, 1373

Weinberg, D. H., Ostriker, J. P., & Dekel, A. 1989, *ApJ* **336**, 9 (WOD)

Weinberg, D. H., Dekel, A., & Ostriker, J. P. 1990, in preparation

Weinberg, S. 1972, *Gravitation and Cosmology*, New York John Wiley

West, M.J., & Van den Bergh, S. 1991, *ApJ*, **373**, 1

White, S. D. M. 1979, *MNRAS* **186**, 145

White, S.D.M., Frenk, C.S., Davis, M., & Efstathiou, G. 1987, *ApJ*, **313** , 505

Whitmore, B., 1989, STScI preprint, **410**.

Xia, X.Y., Deng, Z.G., & Zhou, Y.Y. 1987 in *Observational Cosmology*, IAU Symp. **124**, eds. A. Hewitt, G. Burbidge, & L.Z. Fang, Reidel.

Zwicky, F., Herzog, E., Wild, P., Karpovicz, M., & Kowal, C. 1961-68 *Catalogue of Galaxies and Clusters of Galaxies, Vols 1-6*, California Institute of Technology, Pasadena